WASM: Minerals, Energy and Chemical Engineering

Fundamental Study of Gas Adsorption in Porous Materials using More Realistic Models

Xiu Liu

0000-0003-4592-7232

This thesis is presented for the Degree of
Doctor of Philosophy
of
Curtin University

May 2020

Declaration

To the best of my knowledge and belief this thesis contains no material previously published by any other person except where due acknowledgment has been made.

This thesis contains no material which has been accepted for the award of any other degree or diploma in any university.

Signature: …….

Date: 01/05/2020 …….

Abstract

Adsorption is used in extensive industrial applications such as gas separation and purification, pollution control and energy storage, etc. The theoretical fundamental understanding of various adsorption phenomena and the underlying mechanisms is vital for industrial design improvement and optimization. Numerous studies have been conducted with molecular simulation as the main tool in understanding various adsorption phenomena. However, the majority are based on the simplified models which are too ideal to be true in the practical applications. Therefore, the main objective of this project is using Monte Carlo simulation to investigate the mechanisms of gas adsorption in porous materials with more realistic models. And the thesis is composed by three main parts.

The first main part is about the bulk phase equilibria study conducted with the Bin-CMC scheme, as the correct description of the experimental phase behavior is the precondition for generating reliable results of adsorption systems. Good agreements were achieved between simulation results and experimental data for the two gases: Ar and Xe, which were chosen as the adsorbates for the adsorption studies included in the second part of the thesis.

The second part focuses on simple gas adsorption study with more realistic adsorbent models (wedge pore and deformable pore) with the combined utilization of GCMC and CMC methods. Compared to the commonly used ideal homogeneous slit pore, wedge pore is a more realistic adsorbent model by considering the continuous changing size along the axial direction. A systematic study was carried out for both open wedge and closed-end wedge, particularly attentions were paid to the step-wise hysteresis and existence of hysteresis in the closed-end wedge pore. Microscopic evidences were provided for the existence of hysteresis in closed-end wedge pore under the triple point of xenon which is due to the formation of an ordered domain and its evaporation. The adsorbed phase inside the closed-end wedge pore is denser than

the supercooled liquid, and yet is not as structured as the bulk solid. Another more realistic pore model is the deformable connected pore, which considers both the effects of connectivity and adsorption-induced deformation. Four deformation modes of argon in connected deformable pores were observed and the micro- narrow section plays a dominating role over the wide section. Moreover, hysteresis exists when the length ratio of the micro- narrow section exceeds half of the total pore length, indicating that adsorbent deformation could be another origin of hysteresis.

The third part is about the application of theoretical studies to a practical case, i.e. the adsorption removal of mercury with carbonaceous materials. A new Lennard-Jones (LJ) type state-dependent potential model for mercury was developed, which shows superior performances compared with previous LJ models. With the success of newly developed model, for the first time, mercury physisorption in AC was studied with MC simulation and simulation results agree qualitatively well with experimental measurement. The new mercury potential shows its applicability in the description of mercury-carbon interaction. The wetting temperature of mercury on graphite was found to be 1600 K, supporting the fact that mercury does not wet carbon under ambient conditions. Furthermore, it was illustrated that mercury can fill ultrafine graphitic slit pores, i.e. widths less than 0.7 nm, at ambient temperatures, because of the enhancement of the solid-fluid potential and the strong intermolecular interactions.

List of Publications

Journal papers

- **Liu, X.**, Fan C., Do D. D., Pareek V. and Yang P., A Temperature-dependent Potential Model for Mercury in the Description of Vapour-Liquid Equilibrium & Adsorption in Activated Carbon. *Chemical Engineering Science*, **2020**, 215, 115453.
- **Liu, X.**, Fan C., Do D. D. and Leong C. F., On the Hysteresis of Low Temperature Adsorption of Xenon in Graphitic Wedge Pore. *Chemical Engineering Journal* **2020**, 390, 124499.
- **Liu, X**., Fan C. and Do D. D., Microscopic Characterization of Xenon Adsorption in Wedge Pores, *Adsorption*, **2019**, 25, 1043-1055.

Conference abstracts

- **Liu, X**., Fan C., Do D. D., Low Temperature Adsorption of Simple Gas in Graphitic Wedge Pores with GCMC Simulations, PBAST-8, 03-06 Sep. 2018, Sapporo, Japan.
- Fan, C.; Do, D. D., **Liu, X.**, C. F. Leong, Effects of Graphene Size and Shape on Adsorption of Gases in Activated Carbon. Carbon 2018, 1-6 Jul, 2018, Madrid, Spain.
- Fan, C.; **Liu, X.**, Do, D. D.; Nicholson, Do., Simulation of Phase Diagram of Ethylene Adsorption on Graphite at Low Temperatures - The Importance of Energetic Corrugation and Anisotropy in Polarizability of Carbon Atom, PBAST8, 3-5 Sep, 2018, Sapporo, Japan
- Fan, C.; **Liu, X.**, R. Diao; Do, D. D.; Development of Temperature-Dependent Potential Model for Mercury with Bin-Monte Carlo Method. MM2017, 27-29 Sep,

2017, Margaret River, WA, Au.

- Fan, C.; **Liu, X.**, Do, D. D.; Adsorption Removal of Hg by Activated Carbon - A Monte Carlo Simulation Study. 2019 AUSTRALIA – CHINA Science, Technology, Commercialisation & Innovation Forum, 21-23 January, 2019, Chongqing, China.
- Fan, C.; **Liu, X.**, Do, D. D.; On the Hysteresis and Step-Wise Behaviour of Noble Gas Adsorption in Wedge Pores. 13th International conference on the Fundamentals of Adsorption, 26-31 May 2019, Cairns, Australia

Acknowledgements

My first acknowledgement goes to the Curtin International Postgraduate Research Scholarship (CIPRS) for the financial support during my PhD project.

I sincerely appreciate my principal supervisor Professor Vishnu Pareek for his continuous support and guidance throughout my PhD. My special and deepest appreciation goes to my supervisor Dr. Chunyan Fan for her magic of rebuilding my confidence in computer simulation and academic research. I would not have completed my PhD without the many discussions, hands-on guidance and training, enormous assistance and patience from her. Her warmth, optimism and thoughtfulness have given me huge power to overcome my hardest times. My deep gratitude goes to my co-supervisor Professor Duong D. Do from the University of Queensland for his enormous valuable guidance, suggestions and assistance. I am so lucky to have them as my supervisors. Great thanks to my thesis committee chairperson Professor Shaomin Liu for his assistance and advice.

Great thanks to the friendly staff and colleagues in the Discipline of Chemical Engineering and the Pawsey Supercomputing Centre for their help.

Thanks to all my friends in Australia and China, especially Wei and Mi for their care.

Finally, special thanks to my boyfriend Chaoran for his love, care and company for more than seven years. Deep gratefulness to my parents and younger brother for their love and encouragement. My father keeps struggling for two years until the completion of my PhD though suffering from serious disease, which is impossible without my mother's good care. My brother Ke, though very young, has given me enormous encouragement to overcome this difficulty. My grandma lives in my heart forever and I believe you have seen the journey of pursuing my PhD. Great help from aunt Xianying and cousin Dong are acknowledged. I wish the ones loving me and loved by me permanent happiness and health.

Table of Contents

List of Figures

List of Tables

Nomenclature

CMC	Canonical Monte Carlo
GCMC	Grand Canonical Monte Carlo
Bin-CMC	bin Canonical Monte Carlo
MD	Molecular Dynamics
MC	Monte Carlo
EOS	Equation of State
LJ	Lennard-Jones
fcc	Face Centred Cubic
FF	Fluid-Fluid
SF	Solid-Fluid
SS	Solid-Solid
LB	Lorentz–Berthelot
IUPAC	International Union of Pure and Applied Chemistry
vdW	van der Waals
VLE	Vapour-Liquid Equilibria
VSE	Vapour-Solid Equilibria

Chapter 1. Introduction

1.1 Background and Motives

The industrial importance of adsorption is self-evident in various fields and applications, such as gas purification and separation, pollution control, energy utilization and storage, catalyst supports, etc. [1]. Moreover, adsorption has become one of the standard methods for determining the pore size distribution and surface area of porous materials [2-5]. Therefore, it is essential to provide a theoretical fundamental understanding of various adsorption phenomena and the underlying mechanisms for the design and optimization of industrial adsorption process as well as the characterization of porous solids.

Looking back upon the classical adsorption theories, it is Langmuir, the earliest pioneer, who constructed a theoretical mathematical model at molecular level for adsorption on a homogeneous surface in 1918 [6]. Inspired by that, since then diverse models for more complicated adsorption systems have been put forward by other early pioneers such as Brunauer, Emmett and Teller [7]. The limitations of these classical models are obvious as they involved many idealized assumptions and extra fitting parameters and can be only applied in rather specific adsorption systems.

The swift development of computer science and technology have hastened the invention and improvement of many computational techniques achieving a better theoretical understanding of adsorption, such as the lattice gas theory, density functional theory and molecular simulation. Moreover, the availability of the High Performance Computing machines in the past two decades has made the theoretical calculations much more precise and reliable than ever before. In principle if the molecular interaction potentials of all the components in the adsorption system are clear, all the thermodynamic properties can be accurately obtained by computational

calculations. Another advantage of these abovementioned techniques is that it can deal with extreme conditions that beyond the experimental scope such as extreme high pressure and temperature, toxic, explosive, etc. Among these techniques, molecular simulation is the most popular, powerful and predominant tool in the theoretical study of adsorption behavior and mechanism. The two equivalent principal approaches of molecular simulations are Molecular Dynamics (MD) simulation and Monte Carlo (MC) simulation [8, 9]. MD simulation solves the motion equations of particles and calculates the related fluid properties as a time average, and it has the advantage of being able to trace the kinetic evolution of the system. However, its application has been limited due to the rather short time scale that can be handled with current computation power. On the other hand, MC simulation is more preferred for the study of equilibrium of the adsorption system due to its usage of importance sampling with respect to the Boltzmann weight of configurations to calculate thermodynamic properties as an ensemble average [9].

Two essential components included in any adsorption system are adsorbate (or gas/fluid) and adsorbent (or solid). One of the most vital parameters to ensure the reliability of the computation is the correct description of the interactions included in the adsorption system, which usually realized through the selection of the suitable potential models for both the adsorbate and adsorbent. The potential model of adsorbate can be evaluated by its description of bulk phase equilibria [10-12], and the good agreement with experimental data is a prerequisite to obtaining reliable adsorption results [13]. This evaluation process can also be used in the development of a new adsorbate model [14].

In practical application the majority of the adsorbents are highly porous, and very often then their structures are complicated. Carbonaceous materials are one of the mostly widely used adsorbents. Extensive theoretical studies have been conducted to build a firm foundation for adsorption mechanisms by using ideal simple uniform adsorbent

models like homogeneous graphitic slit pore to represent the pores presented in carbonaceous materials [15-21]. However, this pore model is too idealized considering the highly heterogeneous pore structures that observed experimentally [22, 23], including the characteristics of wedge shape, connectivity between pores, corrugation on pore walls, closed at one end and flexible pore walls, etc. Given these facts, it is essential to utilize more realistic adsorbent models in order to improve the understanding of the adsorption mechanisms in practical application. Meanwhile, from the fundamental perspective, many issues remain unresolved and need further investigation, such as one of the long-lasting controversial topics about whether hysteresis loop exists in closed-end pore, and the adsorption-induced solid deformation in more complicated pore structure, etc. These aspects were investigated in this thesis.

More specifically, there are three main objectives of this thesis. The first aim is to evaluate the potential models of adsorbate through comparing the simulated bulk phase behaviors against experimental data, with a special challenge in developing a new potential model for mercury. The second aim is to gain a theoretical fundamental understanding of adsorption in porous materials with more realistic pore models including the wedge pore model and connected deformable pore model, with particular emphases on the hysteresis and the microscopic mechanisms. And the third aim is to test the mercury potential model developed at earlier stage in adsorption systems and evaluate its performance by comparing with the experimental measurements, which will act as a stepstone for future studies in improving the technology of adsorptive removal of mercury.

1.2 Literature Review

1.2.1 Potential Models of Adsorbate

Among the many types of potential models available in the literature, Lennard-Jones (*LJ*) potential and exp-6 potential are the two commonly used types in MC simulations. Compared to the two-parameter *LJ* potential, exp-6 potential and other ones like Mie

potential have an extra parameter which carries more ambiguous meaning though they show advantage under some conditions like very high pressures [24, 25]. The *LJ* potential has gained greater popularity because of its simplicity and higher computational efficiency [11]. Moreover, the *LJ* potential is favored in adsorption systems due to its compatibility with the well-known Steele 10-4-3 equation, Bojan-Steele equation and other equations for the calculation of adsorbate-adsorbent interactions [26-28]. Even with this very simple and convenient form of the *LJ* potential which is a function of only two effective parameters: collision diameter σ_{ff} and reduced well depth ε_{ff}, we might feel dazzled by choosing a proper one from the many different sets of parameters for a specific adsorbate or fluid.

Almost all molecular potentials (*LJ* potential included without exception) are of an empirical nature with effective parameters obtained from the fitting of particular experimental data or appropriate macroscopic properties [11], such as spectroscopic data, second virial coefficient, liquid radial density distribution, gas viscosity data, and vapor–liquid equilibria (*VLE*), etc. Generally, the effective parameters obtained from the fitting of second virial coefficient perform better than those obtained from gas viscosity data [29]. However, properties like density and pressure are more of interest in adsorption system. Therefore, phase equilibria data could act as a suitable criterion in choosing the potential modes. Do and co-workers put forward that in adsorption systems where equilibrium is established between the dense adsorbed phase and the gaseous phase, the molecular parameters which are able to describe the *VLE* are the most suitable for the study of adsorption [29]. Out of similar considerations, many research groups have been continually devoted to developing potential models which are able to reproduce the phase coexistence properties to near-experimental accuracy [30]. One of the most successful series is the Transferable Potentials for Phase Equilibria (TraPPE) model, especially for more complex adsorbates other than noble gas family [31-34].

Noble gas family, as the simplest non-polar single-site adsorbates having spherical geometry, are the most widely used LJ fluids in providing fundamental insights into adsorption phenomena [12]. For example, Ar is one of the standard adsorbates used for the characterization of porous carbonaceous materials and it can probe much smaller pore entrances than N_2 (e.g. the lower detection limits in cases of Ar and N_2 at 77 K are ~4 and ~5 nm, respectively) [35, 36]. Xe is drawing increased attention these years as it has much stronger intermolecular interaction, strength of which is almost double that of Ar [37-39]. The potential models of Ar and Xe adopted in this thesis are summarized in Chapter 2.

Apart from these noble gas adsorbates, a special attention was turned to mercury, which is the only metal presents in liquid state at ambient conditions and has a high volatility. It is akin to noble gas to some extent due to its inertness. A survey of the literature shows that the conventional 12-6 Lennard-Jones potentials fail to describe the behaviours of bulk mercury over a wide range of temperature [40, 41]. It has been experimentally reported that mercury can form clusters, and the cluster size decreases with temperature [42] and the transition from metal to non-metal (*M-NM*) occurs at a density close to 9 g/cm^3 [43] when the cluster comprises of 100 atoms [42]. In the *M-NM* transition region, the number of atoms in the cluster decreases to 30 and the interatomic interaction is transformed from metallic bonding to covalent bonding [44]. Furthermore, as the temperature approaches the critical temperature, the electrical conductivity decreases and the metallic character disappears [45] for a cluster size of 21 atoms, below which the van der Waals (*vdW*) interaction is dominant [44]. It clearly shows the complex behaviour of mercury in the transition from metallic to covalent and then to *vdW* force with a decrease in the cluster size, and this is corroborated in the experimental work of Inui and co-workers that mercury near the bulk critical point exhibits insulating properties and behaves like a *vdW* fluid [46]. This suggests that mercury can be modelled as an *LJ* fluid, at least for temperatures close to the critical point. For temperatures well below the critical point, the complex

behaviour of mercury, as mentioned above, renders the *LJ*-equation not suitable to correctly describe the vapour-liquid equilibrium.

Beside the various 12-6 *LJ* potential equations that have been proposed in the literature, there are attempts to develop equations with quantum mechanical calculations to investigate the energy curves for the ground and excited states of mercury dimer [42, 47-49]. The ab initio pairwise interaction potential energy is modelled with different functional forms, for example *LJ*, Morse [41, 42] and exponential [48]. Despite of their firm theoretical basis, these equations fail to describe the vapour-liquid equilibrium, which has been attributed to the multi-body interactions [50]. As documented in the literature, multibody effects could result from the formation of clusters [51], relativistic contraction effect (or spin-orbit) [52] and polarization [40], etc. However, even when these are accounted for [45], these sophisticated potentials are unable to describe the experimental data accurately, e.g. the dissociation energy and equilibrium interatomic separation could not be reproduced [42, 47, 53]. For the practical purpose of accurately describing the data, the sophistication can be traded off with simpler approaches, for example Bomont and Bretonnet (*BB*) [50] and Raabe and Sadus (*RS*) [54] proposed empirical equations for the intermolecular interaction with temperature-dependent parameters to implicitly account for the multibody effects with some improvement over the classical 12-6 Lennard-Jones equation. Recently, the same method applied in RS model was applied by Tang et al. in proposing a force-field fitting model to consider the temperature effects [55]. The details of the *BB* and *RS* models are summarized in Chapter 3.

1.2.2 Simulation of Bulk Phase Equilibria for Model Evaluation

The careful choice of the potential model is critically essential, otherwise it is likely to result in the failure of the subsequent adsorption simulation because of its inability in correctly describing the bulk phase equilibria, especially the vapor pressure [56]. MC simulation has been widely applied in studying the bulk phase equilibria for the

purpose of model evaluation and development [11, 12, 14, 31-33, 57, 58]. However, phase equilibria issue is quite difficult to be addressed with conventional MC method due to the gradient of density at the interface between the two coexisting phases. Gibbs ensemble MC method was first proposed by Panagiotopoulos in 1987 to address this problem through the molecule swap between two distinct phase boxes [59, 60]. Since then, this technique has been successfully applied to the model evaluation of various adsorbates in the state of pure component or mixtures with moderately complex intermolecular potentials [61-63] but fails for more complex intermolecular interactions, especially for systems involving solid or highly structured phases due to inadequate sampling of the relevant phase regions [30, 64]. Subsequent techniques have been engaged in improving the sampling efficiency and calculation accuracy, for example, Gibbs-Duhem integration method and Grand canonical histogram-reweighting Monte Carlo method [65, 66].

In 2012, Fan et al. developed a new Bin-CMC method by introducing a concept of multi-bins to address the non-uniformity of the system [67]. It features high sampling efficiency especially for the rarefied region which makes it very promising in handling not only the vapour-liquid equilibria but also the vapour-solid equilibria [68]. Bin-CMC has succeeded in describing the density profiles across the interface between the rarefied and dense phases. Another advantage of this technique is that it can yield many thermodynamic properties (e.g. surface tension) which cannot be acquired from the interface-absent Gibbs ensemble MC method [69].

1.2.3 Adsorption in Non-uniform Pores

Various adsorption phenomena in porous materials and the underlying mechanisms keep fascinating the researchers from both fields of science and engineering. Hysteresis is one of the many characters by understanding which could help with the characterization of the porous structures, and its occurrence is affected by many parameters, temperature, pore size and pore structure, etc. The fact that hysteresis

occurs extensively in porous materials has been reported and interpreted by hundreds and thousands of experimental and theoretical studies [70-74]. Conventional consensus is that hysteresis only exists in mesopores at low enough temperatures (below the critical hysteresis temperature) due to capillary condensation [75-77]. However, recent research has proved that hysteresis can also exist in micropores and even on homogeneous surface due to the different origin like ordering transition of adsorbate [78-80], though hysteresis in these cases is commonly regarded to be absent as the mechanism is molecular filling or molecular layering.

With the aid of synthesis of new materials (especially ordered mesoporous materials) [81, 82], high resolution measurement apparatus and the increasing power of computer simulation, the new version of IUPAC classification of hysteresis [83] has been proposed in 2015 (Figure 1.1a). However, the original de Boer classification in 1972 (Figure 1.1b) [84] is still applicable nowadays as it covers certain hysteresis type, like the very unique Type C, which is still not very clearly classified in the new IUPAC classification. These two classifications have only two in common: Type A = Type H1 and Type E = Type H2(a).

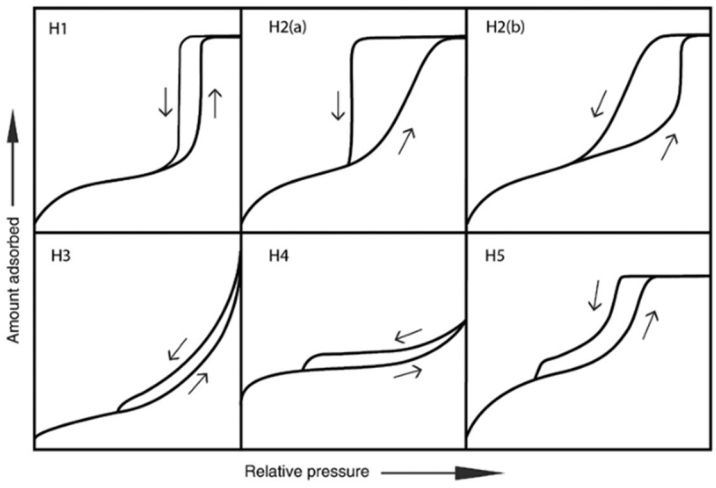

(a)

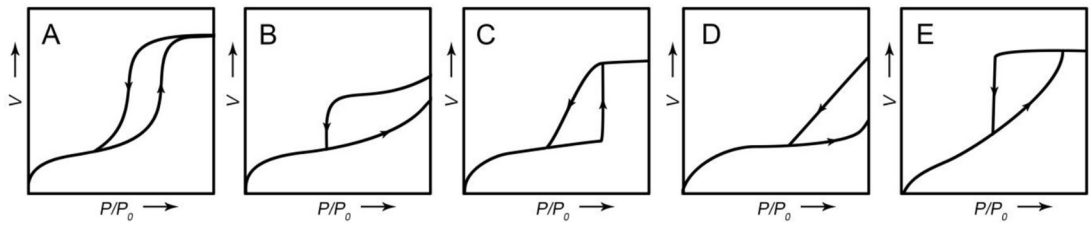

(b)

Figure 1.1 (a) New version of IUPAC classification of hysteresis in 2015; (b) de Boer's original classification of hysteresis in 1972.

Molecular simulation, combined with the usage of various pore models to represent the carbonaceous materials, has become a powerful tool in producing the experimentally observed hysteresis and studying the underlying mechanism. Extensive theoretical studies assume activated carbons as a composite of unconnected slits of different sizes and use the simplest ideal uniform graphitic slit pore model to generate a kernel of local isotherms, and this kernel is used to generate a theoretical isotherm which is then matched against the experimental isotherm to derive the pore size distribution [85-89]. However, the uniform slit pore model frequently underestimates the pore size in determining of mesopore size distribution [90]. Furthermore, this uniform slit pore model is mainly capable in interpreting Type H1 (or Type A) hysteresis, due to adsorption metastability (resulting in delayed condensation) [91, 92]. In fact, the real structure of porous solids is complicated by (1) different shapes of pores; (2) connections between pores, which may vary in size, shape and location; (3) a distribution in the size of the pores [93]; (4) surface energetical heterogeneity and geometrical corrugation [94, 95] and pores with closed end [96]. Very recently, a series of amorphous carbon models have been developed by a group in Curtin University [97], which are more realistic solid models. However, these types of complex solid models will not assist in understanding the mechanism fundamentally and is very expensive for computation purpose. Therefore, it is essential to apply certain models that are simple enough for conducting calculation efficiently meanwhile bringing some of the above-mentioned parameters into consideration to facilitate the fundamental

study.

It is generally clear from many *SEM* studies of activated carbon that it is composed of crystallites, which are randomly stacked against each other and the extent of packing depends on the precursor as well as the conditions of treatment of carbonization and gasification [98]. The interstices between these crystallites form pores, and they are described better with a non-uniform wedge pore model having continuous changing pore size along the axial direction, rather than a uniform slit model. Theoretical research as early as 1960's more focused on the kinetics of capillary condensation and evaporation in wedge pores [99, 100]. Many subsequent studies have utilized the wedge pore model to study the wetting/filling transition [101-104]. However, not much attention has been paid to the adsorption-desorption hysteresis in wedge pore. Nickmand et al. observed that hysteresis in the single wedge pore having two open ends resembles the de Boer Type C, and it is significantly affected by pore angle and pore length, which differs so much from that in uniform pores [105]. de Boer originally associated Type C loop with cavities that could be emptied through windows that with a wide range of openings, so that each cavity would be emptied when its window became sub critical; the implicit assumption being that each window has a direct pathway to the external adsorptive phase [106]. Recently, Zeng et al. proposed that the Derjaguin-Broekhoff-de Boer (DBdB) equation can describe the desorption process from a filled wedge pore [107, 108], and wedge pore model is an alternative to the uniform slit pore model for the characterization of activated carbon [90]. They observed a very interesting step-wise behavior because of the alternation of commensurate and incommensurate packing of molecules along the axial direction. However, this step-wise behavior has not been interpreted well, at least from the microscopic perspective.

The existence of hysteresis in the isotherm for gas adsorption in closed-end pores (with only one end connected to the gas surroundings, and closed at the other end) has been

a controversial topic for many decades. Cohan in 1938 [109] argued that the hysteresis is absent in a closed end cylindrical pore because the interface separating the adsorbed phase and the gas phase is invariant for either increasing or decreasing the pressure. Embedded in this argument are the assumptions that the thermodynamic properties (surface tension and liquid molar volume) of the adsorbate are the same as those of the bulk liquid (i.e. they are not modified by the external adsorbent field). While this theory is plausible for temperatures above the triple point temperature, T_{Tr}, for which the adsorbate is disordered and liquid-like, it is debatable for temperatures below T_{Tr} because the theory does not account for the detailed structure of the adsorbate and the manner in which the adsorbate evolves when the pressure is either increased or decreased. Contrary to the classical view of reversible isotherms in closed-end cylindrical pores, hysteresis has been reported in many experimental and molecular simulation studies of closed-end pores [110-118]. Arguments to support the presence of hysteresis include wide pore size, pore deformation [119], irregularities on an atomic scale or surface heterogeneities of the pore structure [110], or the formation of a cohesive thin film at the pore mouth [111]. Recently, Zeng et al. [120] reported possible sources of hysteresis in closed-end pores: (1) different interface curvatures during adsorption and desorption in weakly adsorbing pores; (2) low temperatures facilitating the adsorbate become solid-like; and (3) restructuring of the condensed phase where adsorbate changes from a liquid-like state to a solid-like state. The common denominator is that the adsorbate does not have the same structure as the bulk liquid and the structure along the adsorption path is different from that along the desorption path for temperatures below the bulk triple point temperature.

Type H2 hysteresis is generally considered to be given by solids having interconnected pore network where larger cavities are laterally surrounded by small necks connected to the bulk gas [83]. It is typically found for interconnected pores that the existence and number of hysteresis loops depend on the sizes of both narrow and wide parts, highlighting the importance of the interconnectivity [23]. The origin of the hysteresis

can be explained by the pore-blocking and/or cavitation mechanism for the desorption process, which is sensitive to the relative size between cavity and neck, temperature and adsorbate species and properties [121-123]. Pore blocking mechanism applies where menisci at the neck mouth recede into the interior of the pore until the cavity is gradually evaporated; cavitation mechanism is applicable when the neck is so small that the condensed fluid inside the cavity is stretched to its limit of mechanical stability at which point the cavity evaporates while the neck remains (partially) filled. In the absence of pore blocking effect, interconnectivity does not affect the desorption pressure [124]. Recently, a more sophisticated mechanism has been proposed concerning both the condensation and evaporation processes [125].

1.2.4 Adsorption-Induced Deformation in Nano-Pores

Adsorption-induced deformation is the phenomenon that the solid undergoes a dimensional change due to the force on its surface exerted by gas during adsorption. Extensive experimental observations have recorded many deformation behaviors: monotonic contraction or expansion, initial contraction followed by expansion, keeping commensurate, even the alternation between expansion and contraction, hysteresis, etc. [126-138]. The first theory for adsorption-induced deformation is the Bangham's law proposed in 1930s' that the expansion is proportional to the deceasing of the solid surface free energy [132, 139]. However, it always predicts expansion at non-zero loading, thus is not applicable to the contraction occurred in micropores [140] which was later explained by Flood et al. as due to the liquid bridging between opposite pore walls [141, 142].

Solvation pressure, the pressure difference inside and outside the pore, is one of the crucial measures of deformation. Ravikovitch and Neimark associated the deformation extent in micropores with solvation pressure [143]. Do et al. demonstrated that solvation pressure is directly related to the deformation which is a complex function of temperature, pore width, pressure, adsorbate species, etc. [144, 145]. Diao et al.

explained the correlation between the adsorbate packing effect and the solvation pressure from the microscopic analysis of the spatial distribution of solvation pressure, revealing that the adsorbed particles closed to the pore walls have a tendency to push the walls apart, while the particles in the interior have a tendency to pull the walls together [146].

1.3 Thesis Objectives

The aim of this thesis is to improve the understanding of mechanism of gas adsorption in porous carbonaceous materials using more realistic models. To achieve this aim, a systematic and comprehensive study by Monte Carlo simulation was conducted; the specific objectives of this thesis include:

1. To investigate the phase equilibria behavior of adsorbates including Ar and Xe to evaluate the potential model used in the thesis.
2. To apply a non-uniform open wedge pore model to investigation of the hysteresis at the molecular level; to prove the existence of hysteresis in closed end wedge pore model with canonical and grand canonical ensembles.
3. To construct and apply a connected deformable pore model to provide insight into the deformation behaviours and mechanisms at the molecular level.
4. To use phase equilibria as a criterion to develop a new potential model for mercury which is compatible with the commonly used potential model of carbonaceous material for MC simulation.
5. To further confirm the validity of the new mercury potential in the description of mercury -carbon interaction to practically study the purification of mercury with activated carbon.

1.4 Thesis Development

Following the brief introduction presented in Chapter 1, Chapter 2 elaborates the

relevant concepts and details of the Monte Carlo simulation applied in this study, including the different Monte Carlo ensembles, the potential models, the equations for calculating the thermodynamic properties and different pore models.

Chapter 3 presents the phase equilibria study of Ar and Xe carried out with Bin-CMC scheme, and this model evaluation process was then applied to the development of a new mercury potential model.

Chapter 4 illustrates the adsorption behaviors of Xe in both open wedge and closed end wedge pores, microscopic characterization were analyzed with particular attention were paid to the packing of Xe inside the pore and the effects of closed end on the existence of hysteresis.

In Chapter 5, Ar adsorption in a connected deformable pore model composed by a micro- section and meso- section is implemented to reveal the respective role of different part in the adsorbate-induced deformation behaviour and their interaction.

In Chapter 6 the study on the adsorption of mercury in carbonaceous materials was attempted with the newly developed potential model of mercury, which is closely related to the practical application of adsorptive removing mercury with activated carbon, and qualitatively good agreement with experiment was reached.

The conclusions of this thesis and the recommendations for future work are summarized in the final Chapter 7.

Chapter 2. Monte Carlo Simulation and Theories

2.1 Introduction

Named after the gambling hot spot in Monaco [147], Monte Carlo (MC) simulation [148], or probability simulation, is a very powerful mathematical and statistical tool to study the equilibrium of an adsorption system if one has correctly described the system in the computer [29]. MC simulation calculates thermodynamic properties by utilizing randomly generated numbers and importance sampling with respect to the Boltzmann weight of configurations, details of which can refer to Frenkel and Smit [8]. Provided that the microscopic reversibility is maintained during the simulation course, equilibrium will be achieved by generating a sequence of configurations on the Markov chain [149]. This Metropolis algorithm is practically applied in various ensembles and schemes, and here we just briefly present the ones adopted in this thesis.

2.2 Monte Carlo Simulation Methods

2.2.1 Canonical Monte Carlo (CMC/NVT)

The canonical ensemble is describing an isolated system with fixed number of molecules (*N*), temperature (*T*) and volume (*V*). There is only one type of movement: displacement of a molecule. The free energy of the system is minimized by displacing a randomly selected molecule to a new position. The probability of accepting the displacement of the molecule is given by:

$$P_{disp}^{acc} = \min\left(1, \exp\left\{-\beta\left(U'-U\right)\right\}\right) \tag{2.1}$$

where $\beta=1/k_BT$ is the reciprocal temperature, and k_B = 1.38066×10^{-23} *J*/*K* is Boltzmann's constant. U and U' are the system energies before and after the displacement. If the displacement of the molecule is accepted, the Markov chain is

updated with the new configuration, otherwise the old configuration is recounted. Simultaneous rotation of the molecule should be performed with the displacement if for multi-site rigid molecule [150].

2.2.2 Grand Canonical Monte Carlo (GCMC)

GCMC was first put forward by Norman and Filinov [151], which is the most extensively adopted MC ensemble in the study of adsorption. Volume (V), temperature (T) and chemical potential (μ) or pressure (P), are kept constant in the system. Fluctuation in the number of adsorbate molecules (N) is allowed due to its connection to the infinite bulk gas reservoir with the same temperature and chemical potential, mimicking the same conditions commonly applied in real experiment.

In addition to the displacement of a molecule, there are another two types of moves: insertion and deletion of a molecule. For the insertion, a molecule is inserted into a randomly selected position in the simulation box, with a simultaneous random rotation if the molecule is multi-site. The probability of accepting the insertion of the molecule is given by:

$$P_{inse}^{acc} = \min\left(1, \frac{V}{\Lambda^3 (N+1)} \exp\left\{\beta\left(\mu - U' + U\right)\right\}\right) \tag{2.2}$$

where U and U' are the system energies before and after the insertion, and Λ is the thermal de Broglie wavelength.

For the deletion, a randomly selected molecule is removed from the N molecules and the probability of accepting the deletion is given by:

$$P_{dele}^{acc} = \min\left(1, \frac{\Lambda^3 N}{V} \exp\left\{-\beta\left(\mu + U' - U\right)\right\}\right) \tag{2.3}$$

where U and U' are the system energies before and after the deletion.

Similarly, if the insertion/deletion is accepted, the Markov chain is updated with the new configuration; otherwise the old configuration is recounted. Equal probability for the insertion and deletion in *GCMC* is set to ensure the microscopic reversibility.

2.2.3 Bin-Canonical Monte Carlo (Bin-CMC)

Bin-CMC scheme was first proposed by Fan et al. [67]. It considered the system non-uniformity and introduced a concept of bins (each bin contains patches of similar interaction energies) to the conventional *CMC*, making use of the grand canonical characteristics within a canonical ensemble. The main feature of *Bin-CMC* scheme is that the maximum displacement length is large in the rarefied region but is small in the dense region, which has improved the sampling efficiency of both regions, especially of the rarefied region.

Same as in conventional *CMC*, temperature (T), total number of molecules (N) and total volume of system (V) are fixed in *Bin-CMC*. However, the fluctuation of molecule number in any given bin is accompanied by change of molecule number in other bins in order to ensure N constant. Each bin can be viewed as a pseudo grand canonical ensemble having constant volume (V_C), temperature (T) and chemical potential (μ). The sequence of the trail moves is: transferring of a molecule from one bin C to another bin D followed by displacement of molecules within the two bins; reverse transferring of a molecule from bin D to bin C followed by displacement of molecules within the two bins. The reverse transferring is to satisfy the microscopic reversibility.

Specifically, transferring a molecule from bin C to bin D includes two steps which are equivalent to the grand ensemble process: first deleting a randomly selected molecule from the bin C to the surroundings at fixed chemical potential, then inserting a molecule from the surroundings to a randomly selected position in bin D. The acceptance probability is given by:

$$P_{tran}^{acc} = \min\left(1, \frac{N_C / V_C}{(N_D + 1) / V_D} \exp\left\{-\beta\left[U(N_D + 1) - U(N_D)\right] - \left[U(N_C) - U(N_C - 1)\right]\right\}\right) \tag{2.4}$$

where the energy change $\left[U(N_D + 1) - U(N_D)\right]$ and $\left[U(N_C) - U(N_C - 1)\right]$ are for the insertion and deletion steps, respectively.

2.2.4 Two Volume-Canonical Ensemble (2V-NVT)

The *2V-NVT* scheme was first introduced by Nguyen et al. [152], based on the gauge cell method developed by Neimark et al. [153, 154]. It is a meso-canonical two-box system: the adsorption system and the bulk gas reservoir. In addition to the displacement moves of randomly selected molecules in the two boxes, molecule exchange between the two boxes is involved as well. The probabilities of accepting these moves can refer to the other methods introduced above. The main advantage of this method is that the full phase diagram of a confined fluid is constructed in the form of a van der Waals (*vdW*) loop, including unstable, metastable and stable states.

2.3 Thermodynamic Property Calculations

2.3.1 Potential Energy

Fluid-Fluid Potential

The Lennard-Jones (*LJ*) model is the most popular potential model to calculate the interaction between two dispersive sites, due to its relative simplicity and the readily available molecular parameters for a wide range of fluids. Moreover, *LJ* model is consistent with the well-known solid-fluid potential equations, such as the Bojan-Steele and Steele equations [26, 28]. The *LJ* 12-6 potential equation for calculating the interaction energy between two single-site molecules is presented as follows:

$$u_{ff}(r) = 4\varepsilon_{ff}\left[\left(\frac{\sigma_{ff}}{r}\right)^{12} - \left(\frac{\sigma_{ff}}{r}\right)^{6}\right] \tag{2.5}$$

where r is the separation distance between two molecules, ε_{ff} is the well-depth of interaction energy and σ_{ff} is the collision diameter when ε_{ff} = 0.

For a molecule having many dispersive sites and fixed partial charges, the interaction energy between two molecules i and j is given by the sum of the Coulomb and the *LJ* 12-6 interactions:

$$u_{ij} = \sum_{a=1}^{A}\sum_{b=1}^{B}\frac{q_i^a q_j^b}{4\pi\varepsilon_0 r_{ij}^{ab}} + \sum_{c=1}^{C}\sum_{d=1}^{D}4\varepsilon_{ij}^{cd}\left[\left(\frac{\sigma_{ij}^{cd}}{r_{ij}^{cd}}\right)^{12} - \left(\frac{\sigma_{ij}^{cd}}{r_{ij}^{cd}}\right)^{6}\right] \tag{2.6}$$

where A and B are the numbers of partial charges on the molecules i and j, C and D are the numbers of *LJ* sites on the molecules i and j, ε_0 is the vacuum permittivity, r_{ij}^{ab} is the separation distance between charge a on molecule i and charge b on molecule j having charges q_i^a and q_j^b, r_{ij}^{cd} is the separation distance between the *LJ* site c on molecule i and the *LJ* site d on molecule j, ε_{ij}^{cd} and σ_{ij}^{cd} are the combined *LJ* well-depth and collision diameter for the two *LJ* sites, which are calculated by the Lorentz-Berthelot (*LB*) combining rules [155]:

$$\varepsilon_{ij}^{cd} = \sqrt{\varepsilon_i^c \varepsilon_j^d} \qquad \sigma_{ij}^{cd} = \left(\sigma_i^c + \sigma_j^d\right)/2 \tag{2.7}$$

In this thesis, Ar and Xe are modelled as single dispersive site molecules with the corresponding molecular parameters listed in Table 2.1.

Table 2.1 LJ molecular parameters of the adsorbates used in this thesis.

Adsorbate	σ_{ff} **(nm)**	ε_{ff}/k_B **(K)**	**Source**
Ar	0.3405	119.8	Michels and Wijker [156]
Xe	0.4047	231	Reid et al. [157]

Solid-Fluid Potential

Two approaches are mainly used to model the graphitized surface of carbonaceous solids. One is the structured graphene layer composed of discrete carbon atoms, which are periodically arranged in hexagonal units with a carbon-carbon bond length of 0.142 nm, and usually the carbon surface consists of three graphene layers with a spacing of 0.3354 nm between two layers [158]. The other is the unstructured solid model composed of structureless graphene layers having constant density of carbon atoms. It has been demonstrated that the two models generate identical simulation results [159] at high enough temperature so that the barrier between the hexagonal sites is lower than $k_B T$. In order to save computation costs, the unstructured model was adopted in this thesis, which can be classified into two types, the infinite and semi-finite surface.

Infinite unstructured model

The solid-fluid (*SF*) interaction energy between a molecule *i* and a homogeneous infinite flat solid surface is given by the Steele 10-4-3 potential model [28, 160]:

$$u_{i,s} = 2\pi\rho_s\varepsilon_{sf}\sigma_{sf}^2\left\{\frac{2}{5}\left(\frac{\sigma_{sf}}{z_i}\right)^{10} - \left(\frac{\sigma_{sf}}{z_i}\right)^4 - \frac{\sigma_{sf}^4}{3\Delta\left(0.61\Delta + z_i\right)^3}\right\} \tag{2.8}$$

where ρ_s is the surface carbon atom density of a graphene layer (38.2 nm^{-2}), z_i is the

shortest distance between the molecule and the surface, and Δ is the spacing between two adjacent graphene layers (0.3354 nm). The *SF* molecular parameters, the cross collision diameter σ_{sf} and well-depth ε_{sf}, are also calculated from the *LB* combining rule with the molecular parameters for a carbon atom in a graphene layer σ_{ss} = 0.34 nm and ε_{ss}/k_B = 28 K.

Semi-finite unstructured model

We use Bojan-Steele potential model to calculate the interaction energy between a molecule and a homogenous surface having infinite *x*-dimension and finite *y*-dimension [26, 38, 161, 162]:

$$u_{f,s} = 2\pi\rho_s\varepsilon_{sf}\sigma_{sf}^2\left\{\left[u_{rep}\left(z,y^+\right)-u_{rep}\left(z,y^-\right)\right]-\left[u_{att}\left(z,y^+\right)-u_{att}\left(z,y^-\right)\right]\right\} \tag{2.9}$$

where ρ_s is the surface carbon atom density, *z* is the shortest distance between the homogenous surface and the molecule, σ_{sf} and ε_{sf} are the *SF* molecular parameters. The variables y^+ and y^- are the *y*-coordinates of the right- and left-hand edge of the homogenous surface relative to the position of the molecule:

$$y^+ = \frac{W}{2} - y \qquad\qquad y^- = -\frac{W}{2} - y \tag{2.10}$$

Figure 2.1 presents the configuration of the homogenous surface at the centre of which is the origin of the *y*-coordinate. The repulsive and attractive functions on the *RHS* of eq. (2.9) are given by:

$$u_{rep}\left(z,y\right) = \frac{y}{\sqrt{y^2+z^2}}\left[\begin{array}{l}\frac{1}{5}\frac{\sigma_{sf}^{10}}{z^{10}}+\frac{1}{10}\frac{\sigma_{sf}^{10}}{z^8\left(y^2+z^2\right)}+\frac{3}{40}\frac{\sigma_{sf}^{10}}{z^6\left(y^2+z^2\right)^2}+ \\ \frac{1}{16}\frac{\sigma_{sf}^{10}}{z^4\left(y^2+z^2\right)^3}+\frac{7}{128}\frac{\sigma_{sf}^{10}}{z^2\left(y^2+z^2\right)^4}\end{array}\right] \tag{2.11}$$

$$u_{att}(z,y)=\frac{y}{\sqrt{y^2+z^2}}\left[\frac{1}{2}\frac{\sigma_{sf}^4}{z^4}+\frac{1}{4}\frac{\sigma_{sf}^4}{z^2\left(y^2+z^2\right)}\right] \tag{2.12}$$

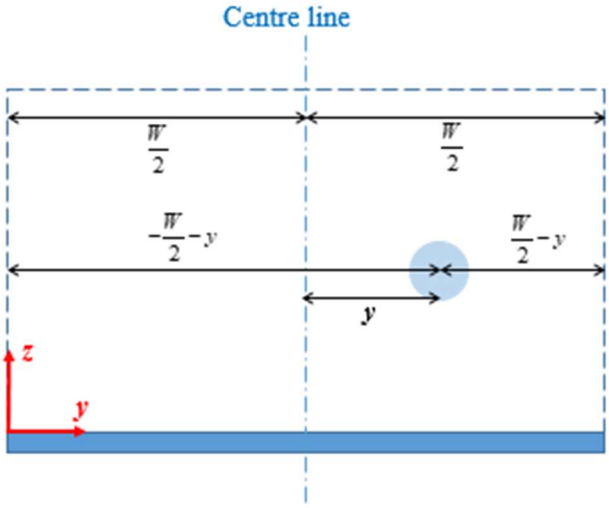

Figure 2.1 Schematic plot of the finite homogenous surface having finite *y*-dimension and infinite *x*-dimension (perpendicular to the page).

The potential equation (2.9) applies for any molecule around the surface. However, eqs. (2.11) and (2.12) become undefined when the molecule is located exactly at the same level as the surface (i.e. $z = 0$). In this case, a Taylor series expansion of these two equations is taken to find their limit when z approaches zero:

$$\lim_{z\to 0} u_{rep}=\frac{y}{\sqrt{y^2}}\left[\frac{1}{5}\left(\frac{\sigma_{sf}}{z}\right)^{10}-\frac{63}{1280}\left(\frac{\sigma_{sf}}{y}\right)^{10}+O\left(z^2\right)\right] \tag{2.13}$$

$$\lim_{z\to 0} u_{att}=\frac{y}{\sqrt{y^2}}\left[\frac{1}{2}\left(\frac{\sigma_{sf}}{z}\right)^{4}-\frac{3}{16}\left(\frac{\sigma_{sf}}{y}\right)^{4}+O\left(z^2\right)\right] \tag{2.14}$$

Substituting eqs. (2.13) and (2.14) into eq. (2.9), the final solution for *SF* potential at $z = 0$ is obtained as:

$$u_{f,s}=\psi 2\pi\rho_s\varepsilon_{sf}\sigma_{sf}^2\left\{\frac{63}{1280}\left[\left(\frac{\sigma_{sf}}{y^-}\right)^{10}-\left(\frac{\sigma_{sf}}{y^+}\right)^{10}\right]-\frac{3}{16}\left[\left(\frac{\sigma_{sf}}{y^-}\right)^{4}-\left(\frac{\sigma_{sf}}{y^+}\right)^{4}\right]\right\} \tag{2.15}$$

where $\psi = 1$ for positive y^+ and y^-, and $\psi = -1$ for negative y^+ and y^-. There is

no singularity in the *SF* potential energy, as one would physically expect it. In the region of small *z*, the *SF* potential energy is calculated from a Taylor series expansion of Bojan-Steele equation (eq. 2.9) as:

$$\frac{u_{f,s}}{\psi 2\pi\rho_s\varepsilon_{sf}\sigma_{sf}^2}=\left\{\frac{63}{1280}\left[\left(\frac{\sigma_{sf}}{y^-}\right)^{10}-\left(\frac{\sigma_{sf}}{y^+}\right)^{10}\right]-\frac{3}{16}\left[\left(\frac{\sigma_{sf}}{y^-}\right)^{4}-\left(\frac{\sigma_{sf}}{y^+}\right)^{4}\right]\right\}$$
$$-\left(\frac{z}{\sigma_{sf}}\right)^2\left\{\frac{231}{1024}\left[\left(\frac{\sigma_{sf}}{y^-}\right)^{12}-\left(\frac{\sigma_{sf}}{y^+}\right)^{12}\right]-\frac{5}{16}\left[\left(\frac{\sigma_{sf}}{y^-}\right)^{6}-\left(\frac{\sigma_{sf}}{y^+}\right)^{6}\right]\right\}$$
$$+\left(\frac{z}{\sigma_{sf}}\right)^4\left\{\frac{1287}{2048}\left[\left(\frac{\sigma_{sf}}{y^-}\right)^{14}-\left(\frac{\sigma_{sf}}{y^+}\right)^{14}\right]-\frac{105}{256}\left[\left(\frac{\sigma_{sf}}{y^-}\right)^{8}-\left(\frac{\sigma_{sf}}{y^+}\right)^{8}\right]\right\}$$
$$-\left(\frac{z}{\sigma_{sf}}\right)^6\left\{\frac{45045}{32768}\left[\left(\frac{\sigma_{sf}}{y^-}\right)^{16}-\left(\frac{\sigma_{sf}}{y^+}\right)^{16}\right]-\frac{63}{128}\left[\left(\frac{\sigma_{sf}}{y^-}\right)^{10}-\left(\frac{\sigma_{sf}}{y^+}\right)^{10}\right]\right\}$$
$$+\left(\frac{z}{\sigma_{sf}}\right)^8\left\{\frac{85085}{32768}\left[\left(\frac{\sigma_{sf}}{y^-}\right)^{18}-\left(\frac{\sigma_{sf}}{y^+}\right)^{18}\right]-\frac{1155}{2048}\left[\left(\frac{\sigma_{sf}}{y^-}\right)^{12}-\left(\frac{\sigma_{sf}}{y^+}\right)^{12}\right]\right\}$$
$$+O\left(\frac{z}{\sigma_{sf}}\right)^{10} \tag{2.16}$$

where $\psi=1$ for positive y^+ and y^-, and $\psi=-1$ for negative y^+ and y^-.

Solid-Solid Potential

Apart from fluid-fluid potential and solid-fluid potential, solid-solid potential is also supposed to be added to the total potential energy when studying adsorption-induced solid deformation. For pores having finite *y*-dimension and infinite *x*-dimension, its solid layers are described by the Bojan-Steele potential, schematic of any two layers is shown in Figure 2.2. The interaction between any two solid layers is obtained by summing up the interactions of all the carbon atoms within one solid layer with the other. The interaction between a carbon atom and a solid layer is calculated with the Bojan-Steele equation, only replacing the molecular parameters with σ_{ss} and ε_{ss}. The interaction of all the carbon atoms in the red differential strip of the upper layer

with the other layer is:

$$du_{ss} = 2\pi\rho_s\varepsilon_{ss}\sigma_{ss}^2\left\{\left[u_{rep}\left(z,y^+\right)-u_{rep}\left(z,y^-\right)\right]-\left[u_{att}\left(z,y^+\right)-u_{att}\left(z,y^-\right)\right]\right\}\times L_x\rho_s dy \tag{2.17}$$

where z is the separation distance between the two layers and L_x is the x-dimension of the solid layers. The final solution of the solid-solid interaction energy is obtained by integrating eq. (2.17):

$$u_{ss} = 2\pi\rho_s\varepsilon_{ss}\sigma_{ss}^2\int_a^b\left\{\left[u_{rep}\left(z,y^+\right)-u_{rep}\left(z,y^-\right)\right]-\left[u_{att}\left(z,y^+\right)-u_{att}\left(z,y^-\right)\right]\right\}\times L_x\rho_s dy \tag{2.18}$$

where a and b are the lower and higher boundaries of the upper layer in the y-direction. The integrals for the repulsive and attractive functions are:

$$\begin{aligned}
&\int_a^b u_{rep}\left(z,y^{\pm}\right)dy = \\
&\left\{-\frac{1}{5}\frac{\sigma_{ss}^{10}}{z^{10}}\sqrt{\left(\pm\frac{W}{2}-b\right)^2+z^2}+\frac{1}{10}\frac{\sigma_{ss}^{10}}{z^8}\frac{1}{\sqrt{\left(\pm\frac{W}{2}-b\right)^2+z^2}}+\frac{1}{40}\frac{\sigma_{ss}^{10}}{z^6}\frac{1}{\left(\left(\pm\frac{W}{2}-b\right)^2+z^2\right)^{3/2}}\right.\\
&\left.+\frac{1}{80}\frac{\sigma_{ss}^{10}}{z^4}\frac{1}{\left(\left(\pm\frac{W}{2}-b\right)^2+z^2\right)^{5/2}}+\frac{1}{128}\frac{\sigma_{ss}^{10}}{z^2}\frac{1}{\left(\left(\pm\frac{W}{2}-b\right)^2+z^2\right)^{7/2}}\right\}\\
&-\left\{-\frac{1}{5}\frac{\sigma_{ss}^{10}}{z^{10}}\sqrt{\left(\pm\frac{W}{2}-a\right)^2+z^2}+\frac{1}{10}\frac{\sigma_{ss}^{10}}{z^8}\frac{1}{\sqrt{\left(\pm\frac{W}{2}-a\right)^2+z^2}}+\frac{1}{40}\frac{\sigma_{ss}^{10}}{z^6}\frac{1}{\left(\left(\pm\frac{W}{2}-a\right)^2+z^2\right)^{3/2}}\right.\\
&\left.+\frac{1}{80}\frac{\sigma_{ss}^{10}}{z^4}\frac{1}{\left(\left(\pm\frac{W}{2}-a\right)^2+z^2\right)^{5/2}}+\frac{1}{128}\frac{\sigma_{ss}^{10}}{z^2}\frac{1}{\left(\left(\pm\frac{W}{2}-a\right)^2+z^2\right)^{7/2}}\right\}
\end{aligned} \tag{2.19}$$

$$\int_a^b u_{att}\left(z, y^{\pm}\right) dy = \left\{ -\frac{1}{2}\frac{\sigma_{ss}^4}{z^4}\sqrt{\left(\pm\frac{W}{2}-b\right)^2+z^2} + \frac{1}{4}\frac{\sigma_{ss}^4}{z^2}\frac{1}{\sqrt{\left(\pm\frac{W}{2}-b\right)^2+z^2}} \right\}$$
$$-\left\{ -\frac{1}{2}\frac{\sigma_{ss}^4}{z^4}\sqrt{\left(\pm\frac{W}{2}-a\right)^2+z^2} + \frac{1}{4}\frac{\sigma_{ss}^4}{z^2}\frac{1}{\sqrt{\left(\pm\frac{W}{2}-a\right)^2+z^2}} \right\} \tag{2.20}$$

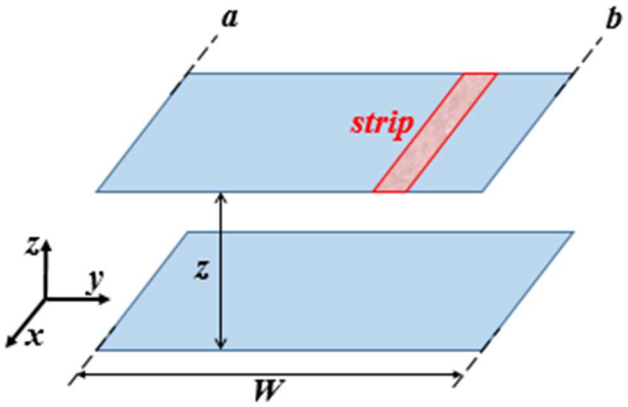

Figure 2.2 Schematic plot of two solid layers described by the Bojan-Steele potential.

2.3.2 Chemical Potential

The chemical potential is contributed by both the ideal gas part and excess part:

$$\mu = \mu_{id} + \mu_{ex} = -k_B T \ln\left(\frac{V/\Lambda^d}{N}\right) + \left(\frac{\partial U}{\partial N}\right)_{T,V} \tag{2.21}$$

where U is the potential energy, N is the number of molecules, V and d are the volume and dimensionality of the system, respectively. The ideal gas part is calculated quite straightforward. The excess part is defined as the partial derivative of U to N.

The Widom molecule insertion method [163] which is based on the statistical

mechanics is a simple and elegant method to measure μ_{ex} by utilizing a perturbation in the number of molecules in the *NVT* system. First, a test molecule is inserted to a randomly selected position at frequent intervals during the simulation course, then the energy between this test molecule and all the molecules in the system is calculated for N_{test} molecules and the ensemble average is obtained as follows:

$$\left\langle \exp\left(-\frac{U_{test}}{k_B T}\right)\right\rangle = \frac{1}{N_{cycle} N_{test}} \sum_{n=1}^{N_{cycle}} \sum_{j=1}^{N_{test}} \exp\left(-\frac{U_{test}}{k_B T}\right) \tag{2.22}$$

where N_{cycle} is the number of cycles for doing the insertion of N_{test} molecules. Then μ_{ex} is calculated by:

$$\mu_{ex} = -k_B T \ln\left\langle \exp\left(-\frac{U_{test}}{k_B T}\right)\right\rangle \tag{2.23}$$

The Widom molecule insertion method is very powerful for calculating the chemical potential of simple molecules and not too dense systems. However, it becomes unreliable for complex molecules and dense systems due to the frequently overlap of the test molecules by the real molecules in the system.

This thesis adopts another method through the equation of state (*EOS*) to calculate the chemical potential in the *GCMC* simulations. The Johnson et al.'s *EOS* is generally applicable for simple *LJ* fluids except under extreme conditions [164].

2.3.3 Pressure

The pressure in the *NVT* simulation is calculated through the virial route [150]:

$$p_G = \rho_G k_B T - \frac{1}{3V_G}\left\langle \sum_{i\in V_G}^{N_G-1} \sum_{\substack{j\in V_G \\ j=i+1}}^{N_G} \omega_{ij} \right\rangle - \frac{1}{6V_G}\left\langle \sum_{i\in V_G}^{N_G} \sum_{j\notin V_G} \omega_{ij} \right\rangle \tag{2.24}$$

where ω_{ij} is the intermolecular pair virial function:

$$\omega_{ij} = \sum_{a=1}^{A}\sum_{b=1}^{B} \frac{\vec{r_{ij}} \cdot \overrightarrow{r_{ij}^{ab}}}{r_{ij}^{ab}} \frac{\partial u_{ij}^{ab}}{\partial r_{ij}^{ab}} \tag{2.25}$$

The second term on the *RHS* of eq. (2.24) is the sum of interactions between N_G molecules in the V_G region while the third term is sum of the interactions between each of the N_G molecules with all the molecules in the surrounding regions.

2.3.4 Enthalpy of Phase Change

The molar enthalpy difference between the two coexisting phases is given by:

$$\Delta h = h_G - h_L = \left(u_G + pv_G\right) - \left(u_L + pv_L\right) = \left(u_G - u_L\right) + p\left(\frac{1}{\rho_G} - \frac{1}{\rho_L}\right) \tag{2.26}$$

where the molar energies of the gas phase and liquid phase are calculated from the sum of the pair interaction energies in a way analogous to eq. (2.24); i.e.

$$U_G = \sum_{i\in V_G}^{N_G-1}\sum_{\substack{j\in V_G \\ j>i}}^{N_G} u_{ij} + \frac{1}{2}\sum_{i\in V_G}^{N_G}\sum_{j\notin V_G} u_{ij} \tag{2.27}$$

$$U_L = \sum_{i\in V_L}^{N_L-1}\sum_{\substack{j\in V_L \\ j>i}}^{N_L} u_{ij} + \frac{1}{2}\sum_{i\in V_L}^{N_L}\sum_{j\notin V_L} u_{ij} \tag{2.28}$$

and $u_G = U_G / N_G$, and $u_L = U_L / N_L$.

2.3.5 Surface Tension

Surface tension is calculated by the Kirkwood and Buff equation [165]:

$$\gamma = \frac{1}{2S}\left\langle \sum_{i=1}^{N-1}\sum_{j>i}^{N} \frac{r_{ij}^2 - 3y_{ij}^2}{2r_{ij}^2} \sum_{a=1}^{A}\sum_{b=1}^{B} \frac{\vec{r_{ij}} \cdot \overrightarrow{r_{ij}^{ab}}}{r_{ij}^{ab}} \frac{\partial u_{ij}^{ab}}{\partial r_{ij}^{ab}} \right\rangle \tag{2.29}$$

where *S* is the interfacial area.

2.3.6 Surface Excess Density

Surface excess density of adsorption is defined as the excess above a reference amount:

$$\Gamma = \frac{\langle N \rangle - V_{acc}\rho_G}{A} \tag{2.30}$$

where A is the surface area of the solid, <*N*> is the ensemble average of the number of molecules, V_{acc} is the accessible volume, and ρ_G is the bulk gas phase density.

The accessible volume V_{acc} is defined as the volume accessible to the mass centre of a molecule at zero loading, as proposed by Do et al. [166, 167],. The calculating process for V_{acc} is as follows: the mass centre of a molecule is inserted to a randomly selected position in the simulation box and a multi-site molecule is given *M* different orientations. If all these *M* orientations have positive values of potential energies, this insertion is viewed as a failure; otherwise, it is a success. Repeat this process and $V_{acc} = fV_{box}$, where f is the fraction of successful insertions and V_{box} is the volume of the simulation box.

2.3.7 Pore Density

The absolute pore density of adsorption with respect to the accessible volume is calculated by:

$$\rho = \frac{\langle N \rangle}{V_{acc}} \tag{2.31}$$

where <*N*> is the ensemble average of the number of molecules within the pore. There are other kinds of volumes to evaluate the pore density, however eq. (2.31) is usually regard as the proper way in describing how dense the adsorbed phase in the pore is.

2.3.8 Isosteric Heat

The isosteric heat is defined as the infinitesimal change of the enthalpy of adsorbate to the infinitesimal change of the excess adsorbed amount. A number of thermodynamic partial derivatives can be calculated by using the fluctuation of thermodynamic properties. The detailed derivation process of the thermodynamic partial derivatives can refer to many books about statistical mechanics [9]. We can obtain the isosteric heat by applying the thermodynamic fluctuations in *GCMC* simulation:

$$q_{st} = k_B T - \frac{f(U,N)}{f(N,N) - \overline{N_G}} \tag{2.32}$$

where $\overline{N_G}$ is the number of molecules of an ideal gas occupying the space of adsorption. With the assumptions of ideal gas and the molar volume of the adsorbed phase being smaller than that of the gas phase, most adsorption work has neglected the second term $\overline{N_G}$ in the denominator, then eq. (2.32) is commonly presented as:

$$q_{st} = k_B T - \frac{f(U,N)}{f(N,N)} \tag{2.33}$$

where U is the configuration energy of the whole system, and N is the number of molecules. The function f is defined as $f(C, D) = \langle C, D \rangle - \langle C \rangle \langle D \rangle$. However, as the adsorptive density may be significant compared to the adsorbed density, the assumptions mentioned above are only applicable for subcritical fluids and will become invalid for subcritical conditions near critical point or supercritical fluids. Do et al. proposed a more general and rigorous equation for isosteric heat [168].

The differential heat of adsorption in a canonical ensemble is defined as the energy change of the adsorbed phase per unit change in the excess number, as presented below:

$$q_{diff} = k_B T - \frac{\partial\{\langle U\rangle - \langle U_G\rangle\}}{\partial\{N - N_G\}} \tag{2.34}$$

where U is the energy of the system, U_G is the energy of the bulk gas phase calculated as $\langle U_G\rangle = \frac{V}{V_M}\langle U_M\rangle$, with U_M and V_M being the energy and volume of a region representing the bulk gas phase, respectively, N_G is the hypothetical number of molecules that occupy the accessible volume at the same density as the bulk gas.

2.3.9 Solvation Pressure

The solvation pressure exerted by the adsorbate on the solid surface is:

$$P_{solv} = \frac{1}{A}\left\langle -\sum_{i=1}^{N}\frac{\partial u_i}{\partial z}\right\rangle \tag{2.35}$$

where A is the total surface area of the solid exposed to the adsorbate, u_i is the *SF* interaction energy of molecule *i* with the solid and *z* is the shortest distance between the molecule and the solid surface.

2.3.10 Bulk Modulus

The bulk modulus is defined as the inverse of the slope of plot of the percentage change of pore width versus solvation pressure:

$$M_b = \frac{\Delta P_{solv}}{\Delta(\Delta H / H)} \tag{2.36}$$

where ΔH and H are the absolute change of pore width and the initial pore width, respectively.

2.3.11 Cohan-Kelvin Equation

The Cohan-Kelvin equation describes the relationship between the condensation pressure and the radius of curvature of the cylindrical interface separating the adsorbed film and the gas phase in the core of a cylinder [109]:

$$RT \ln \frac{p_A}{P_0} = -\frac{\gamma V_m}{r_A} \tag{2.37}$$

where r_A is the radius of the curvature just before the condensation pressure p_A, γ and V_m are the surface tension and the molecular volume of the adsorbate (which is assumed bulk liquid-like), and P_0 is the saturation vapour pressure, R and T are the gas constant and temperature.

Kelvin equation is a more general version of the Cohan-Kelvin equation, it also reveals the above relationship, more details can be found in [90, 169].

2.4 Microscopic Analysis

2.4.1 Local Density Distribution

The local density at the distance z from the solid surface is calculated as:

$$\rho(z) = \frac{\langle \Delta N(z) \rangle}{L_x L_y \Delta z} \tag{2.38}$$

where $\Delta N(z)$ is the number of molecules whose mass centres are positioned in the segment bounded by z and $z + \Delta z$, L_x and L_y are the x- and y- dimensions of the solid surface, respectively.

2.4.2 Local Solvation Pressure Distribution

The local solvation pressure in the y-direction is defined as the sum of the forces per unit area exerted on the solid by molecules in the segment bounded by y and $y + \Delta y$:

$$P_{solv}(y) = \frac{1}{A_{\Delta y}} \left\langle - \sum_{i \in (y, y+\Delta y)} \frac{\partial u_i}{\partial d} \right\rangle \tag{2.39}$$

where $A_{\Delta y}$ is the area of the segment on the surface bounded by y and $y + \Delta y$, d and u_i are the shortest distance and *SF* interaction energy between the molecule i and the solid.

2.4.3 Local Molecular Potential Energy Distribution

The local molecular potential energy in the y direction is defined as:

$$E_{molecular}(y) = \left\langle \frac{\sum_{i \in (y, y+\Delta y)} u_i}{\Delta N(y)} \right\rangle \tag{2.40}$$

2.4.4 2D Density Profiles

The 2D local density is calculated by dividing the simulation box into two-dimensional bins along the y- and z-directions:

$$\rho(z, y) = \frac{\langle \Delta N(z, y) \rangle}{L_x \Delta z \Delta y} \tag{2.41}$$

where $\Delta N\,(z, y)$ is the number of molecules in the bin bounded by $[z, z + \Delta z]$ and $[\, y, y + \Delta y]$. The bin thickness $\Delta z = \Delta y = 0.1\,\sigma_{ff}$. The smoothed density of a given bin is calculated by averaging the densities for its surrounding bins (including the given bin) within a radius of $1.5\,\sigma_{ff}$.

2.5 Setup of Simulation Systems

2.5.1 Coexistence Phase Equilibria System

In a rectangular simulation box as shown in Figure 2.3, the dense phase is placed in

the middle and two bulk gaseous phases are connected at the two ends, forming two interfaces. Periodic boundary conditions are applied in all directions. For the initial configuration at temperatures above triple point, molecules within the dense phase are arranged on lattice sites with a grid size so that the density is equivalent to that of liquid density. For temperatures below triple point, the initial configuration is a solid slab. To calculate the thermal properties of vapour and dense phases, three regions usually with a length of $4\sigma_{ff}$ at the two ends and in the middle are chosen to represent the two bulk gas phases and the bulk liquid (solid) phase, respectively.

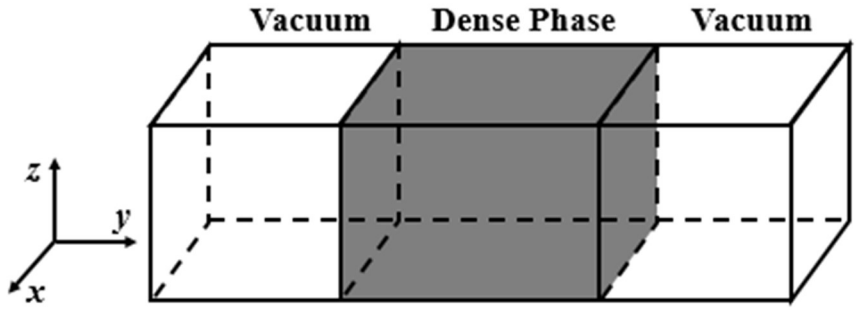

Figure 2.3 The schematic diagram of the initial configuration with a dense phase region in the middle of the simulation box and two vacuum regions on each side.

2.5.2 Adsorption Systems

Slit Pore

Finite slit pore is composed of two parallel graphite walls with each wall consisting of three graphene layers of Bojan-Steele surfaces, with a constant surface density of 38.2 nm^{-2} and a spacing $\Delta = 0.3354$ nm, which is standard setting of graphite walls applied hereafter in this thesis. Its schematic is shown in Figure 2.4. Periodic boundary condition is only applied in the *x*-direction, the two open ends are connected to bulk gas reservoirs so that a mechanical equilibrium can be maintained between the pore and the surroundings through the interaction of molecules inside the pore with the bulk phase. The pore width *H* refers to the distance between the plane passing though the centres of carbon atoms in the innermost layer of one wall and the corresponding plane

of the opposite wall.

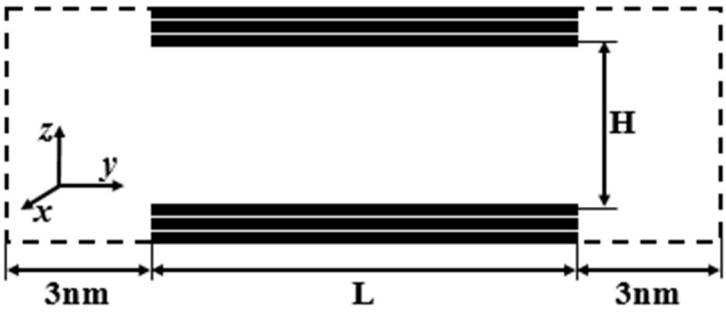

Figure 2.4 The schematic diagram of the finite slit pore model.

Wedge Pore

Figure 2.5a depicts an open wedge pore and its structural parameters: pore sizes at small end (*SH*) and big end (*BH*), axial pore length (*L*) and half wedge angle (α). The dashed lines represent the boundaries of the simulation box in the *y*- and *z*- directions. The gas surrounding at any open end has a length of 3 nm along the *y*- axis, and the dimension in the *z*-direction is decided by the width at the big end. The pore length along the axial direction (the *y*-direction) is finite with the two ends of the pore connected to the surroundings, the dimension in the *x*-direction is assumed to be infinite and only this direction is modelled with the periodic boundary condition.

Figure 2.5b depicts a closed-end wedge pore. Its only difference from the open wedge pore in setting is that one end is closed and at its apex, the spacing between the closest layers of the two pore walls is 0.3354 nm (=Δ). The pore size at the open end is denoted as *H*.

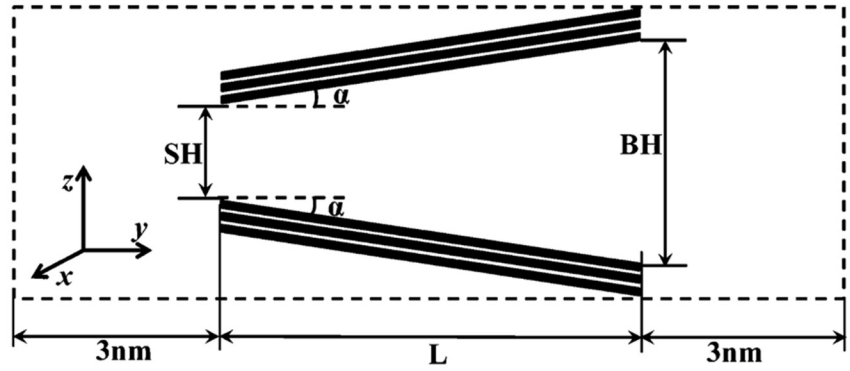

(a)

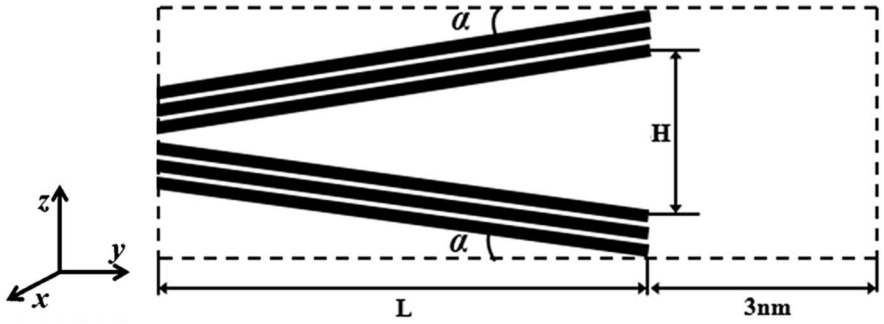

(b)

Figure 2.5 The schematic diagram of two types of wedge pores whose walls are formed by layers of constant solid density and constant spacing between layers: (a) open wedge pore (b) closed wedge pore.

Connected Deformable Pore

Figure. 2.6 depicts a connected deformable slit pore and its structural parameters: narrow part size (H_N), wide part size (H_W), total pore length (L) and length of the narrow part (L_N). The pore length in the y-direction is finite and fixed (L = 20 nm) and the two ends of the pore are connected to the gas surroundings, the x-dimension is assumed to be infinite and the periodic boundary condition is applied in the x-direction to simulate its infinite extent. The walls of the wide pore section have the standard setting. Extra graphene layers are placed on top of the innermost wall of the wide pore to form the narrow part. The two outermost graphene layers are fixed while the others are moveable as whole along the z- direction. The gas surroundings at the two ends are 3nm long along the y-axis, and the z-dimension is determined by the pore

width of the wide part.

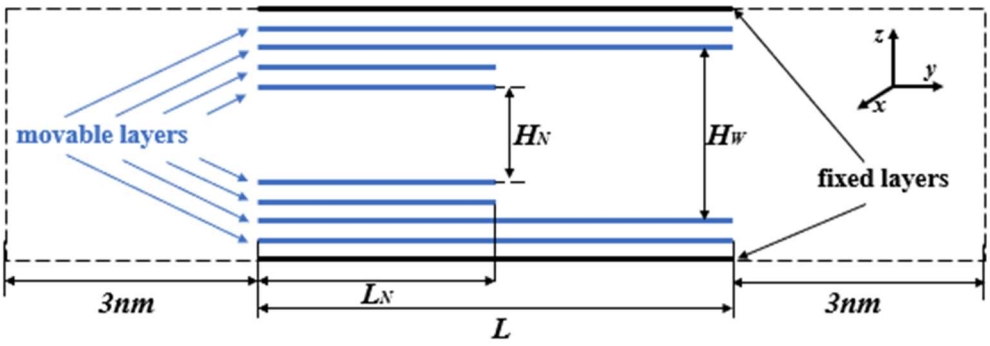

Figure 2.6 The schematic diagram of a connected deformable pore model.

Chapter 3. Vapor-Liquid/Solid Equilibria of Ar, Xe and Hg

3.1 Introduction

The effects of confinement and additional interaction [170] exerted on the fluids by the presented solids on the fluids' behaviors and properties comparing to the corresponding bulk phase has been well recognized. Before investigating the adsorption system, it is essential to select a proper potential model of adsorbate that are interested in. And as proposed by Do et al. that the appropriate potential models should be able to well describe the vapor-liquid equilibria (*VLE*) [29].

In this chapter, Bin-CMC scheme is adopted and the potentials of Ar and Xe used in the subsequent adsorption fundamental study are evaluated by its capability of describing the bulk phase behaviors, including not only vapor-liquid equilibria (*VLE*) but also vapor-solid equilibria (*VSE*). Other thermodynamic properties, such as surface tension, are also calculated. Extensive comparisons between simulation results and experimental data are carried out.

This model evaluation process is then applied in the development of a new potential model for mercury as till now there is no satisfactory potential available and this has hindered the related research. Specifically, we modelled the multi-body effect (as mentioned in Section 1.2.1) by allowing the molecular parameters of mercury to vary with temperature so that the *VLE* and other thermodynamic properties, including the critical point, can be correctly described.

3.2 Simulation Details

Bin-CMC Simulation

For the *VSE* simulations for Ar and Xe at various temperatures under their respective

triple points, the system is initialized by placing a solid slab of 7 × 12 × 7 unit cells (N = 2352) in the middle of an elongated simulation box with two vacuum spaces on both sides of the slab (see Figure 2.3). The dimensions of the box are 11.2σ×(19.2σ+20 nm)×11.2σ with the y-dimensions of the solid slab and each vacuum space being 19.2σ and 10 nm, respectively. The molecules within the solid slab are arranged in the *fcc* structure. The simulation box is divided into 28 bins for the purpose of determining the density distribution, and the bin size is smaller in the interfacial and condensed phase regions and larger in the gas phase region. We used 8×10^5 cycles, with 1000 displacement moves in each cycle, in both the equilibration and sampling stages to ensure the accuracy of output data. During the equilibration of a simulation, the dimensions in the x- and z-directions of the simulation box are allowed to vary in order to facilitate the formation of the condensed phase, and this is done with equal probability at the end of every 1000 cycles. A change in the box length in either the x-direction or the z-direction is carried out with a change in the y-direction to keep the total volume constant, and the maximum change is 1% of the collision diameter. For temperatures above their respective triple points, the same simulation procedure described above is carried out to determine the *VLE* with the only difference that the solid slab is replaced with a lattice having an initial density equal to the bulk liquid density at the boiling point.

The *VLE* study of mercury is carried out at temperatures ranging from the triple point (234K) to the critical point (1751K). The dimensions of the simulation box are 2.4×26.8 ×2.4 nm^3, and the initial density of the lattice is the liquid density at the boiling point (6.82×10^4 mol/m^3). At this density, the simulation box contains 1728 mercury atoms. For temperatures near the critical point, the larger box length in the y-direction is used because of the broader interfacial region between the liquid and vapour phases; the number of mercury atoms is increased to 4096 to minimize the finite size effects. The simulation box is divided into 30 bins in the y-direction. During the simulation, at least 700,000 cycles are used in both the equilibration and sampling

stages.

The Calculation of Solid Phase Density

Solid phase density below the triple point is calculated using the following method:

Figure 3.1 show the local density distribution along *y*-direction for argon at 50K obtained from the Bin-CMC, as indicated in the graphs the region between the two blue dashed lines are selected to represent the solid phase, covering four peaks between two minima, to make sure it covers integer numbers of unit cells.

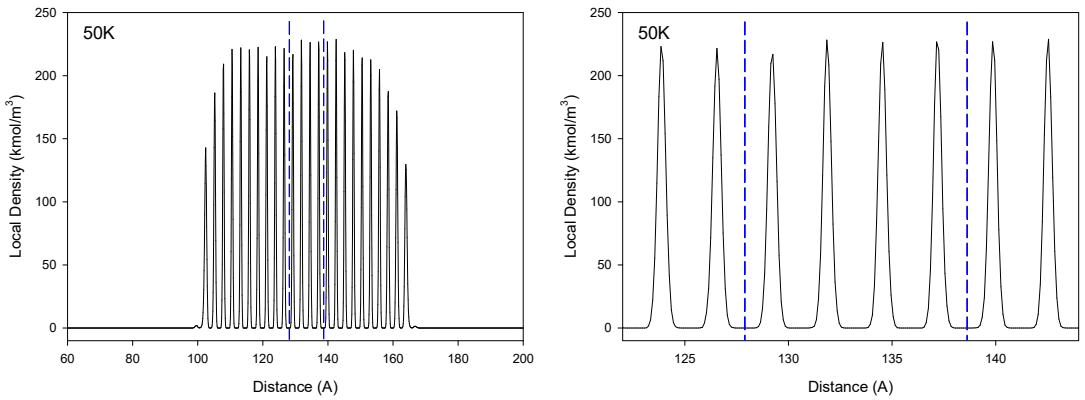

Figure 3.1 The density profile of Ar *VSE* at 50 K, the two dashed lines represents the boundaries of the portion selected for the calculation of solid phase density.

3.3 Results and Discussions

3.3.1 VSE/VLE of Ar

Figure 3.2 demonstrates the comparison between the simulated *VSE/VLE* results (red circle) and experimental data (cross symbol) for Ar from below the triple point (83.8 K in experiment) up to near critical point (150.7 K in experiment). From the vapour-liquid/solid coexistence curve which is temperature versus the coexistence density in linear scale (Figure 3.2a) and in log scale (Figure 3.2b), we can see that the simulated densities of all the three phases (gas, liquid and solid) agree excellently with the experimental data over the whole temperature range. Furthermore, the phase change from solid to liquid at the triple point is accurately captured from the discontinuity in

the branch of the dense phase density. This discontinuity is also captured for the enthalpy of phase change at the triple point that the sublimation heat for gas-solid transition is larger than the evaporation heat for gas-liquid transition (Figure 3.2e). The linear and log scale plots of saturation vapour pressure versus temperature in Figure 3.2c and d demonstrate quite good agreement between simulated results and the experimental data, especially excellent description of the sublimation pressure at temperatures under the triple point, while only presenting small deviations when temperature is approaching the critical point. The plot of surface tension versus temperature (Figure 3.2f) shows the same trend with the simulation over-estimate the experimental values slightly, which could contribute to the finite size effects [171]. Overall, the agreement between simulation results and experimental data is satisfying.

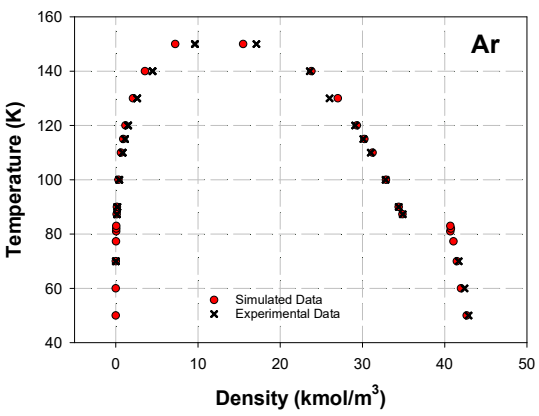

(a)

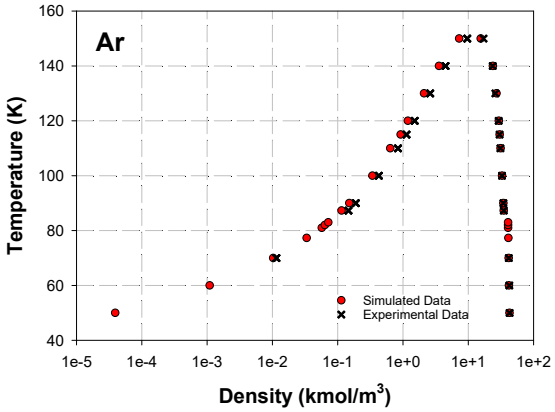

(b)

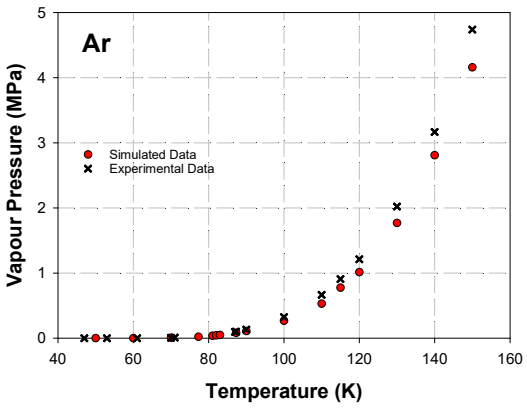

(c)

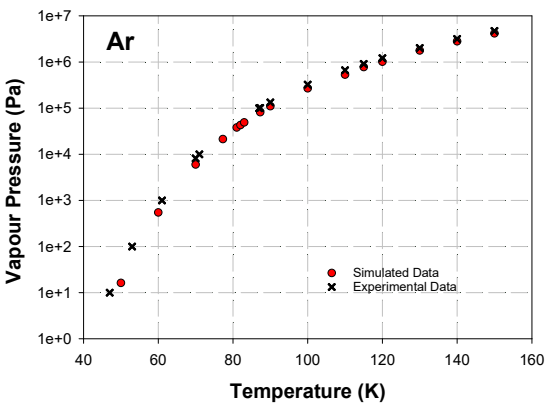

(d)

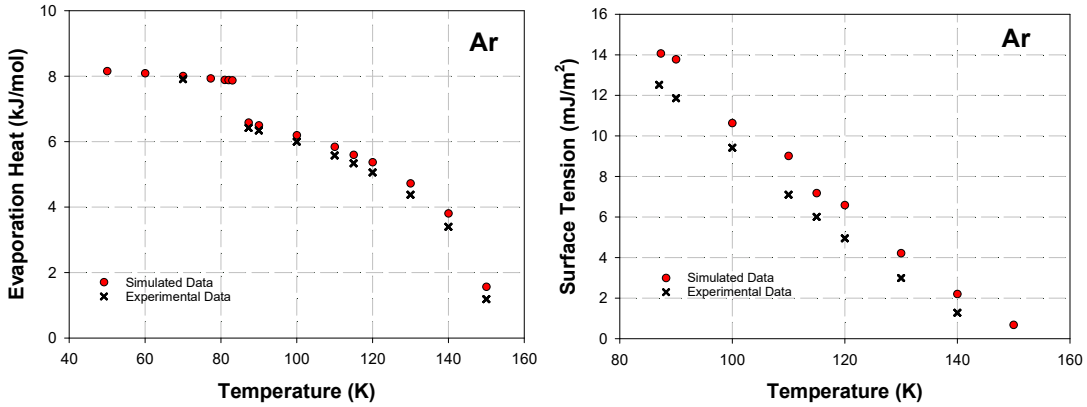

(e) (f)

Figure 3.2 Liquid (solid)-vapour coexistence curves of Ar in (a) linear scale and (b) semi-log scale. Other thermodynamic properties of Ar versus temperature: (c) vapour pressure in linear scale and (d) semi-log scale, (e) evaporation heat and (f) surface tension. The experimental data above triple point in these figures are taken from the database of NIST Chemistry WebBook [172]; The experimental data of vapour pressure under triple point in (c) and (d) are taken from [173]; The experimental data of solid phase density and sublimation heat under triple point in (a), (b) and (e) are taken from [174]. Statistical uncertainties are smaller than the size of the symbols used in the above figures.

3.3.2 VSE/VLE of Xe

The comparison between the simulated *VSE/VLE* results (red circle) and experimental data (cross symbol) for Xe from below the triple point (161.4 K in experiment) up to near critical point (289.7 K in experiment) is shown in Figure 3.3. Generally, we can see that good agreement has been reached between simulation results and experimental data as for all the properties been considered. Similar to Ar, a discontinuity at the triple point is also observed in both the dense phase density profiles and the enthalpy of phase change.

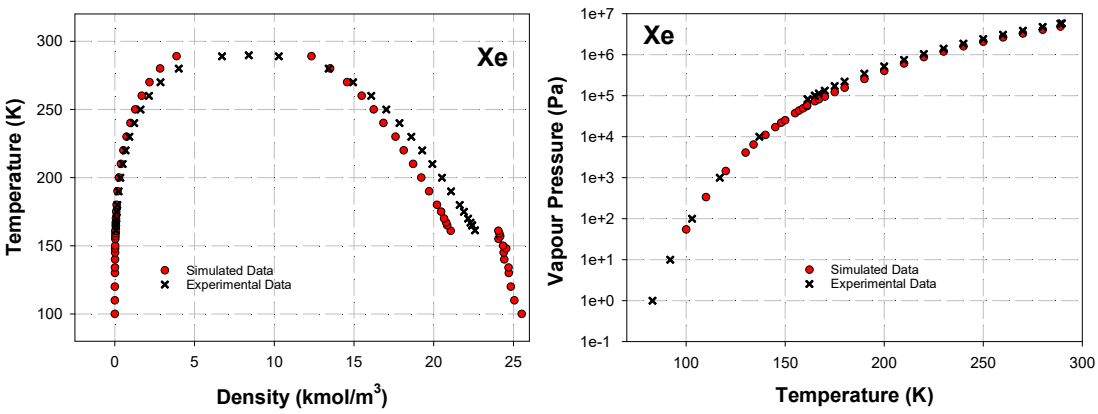

(a) (b)

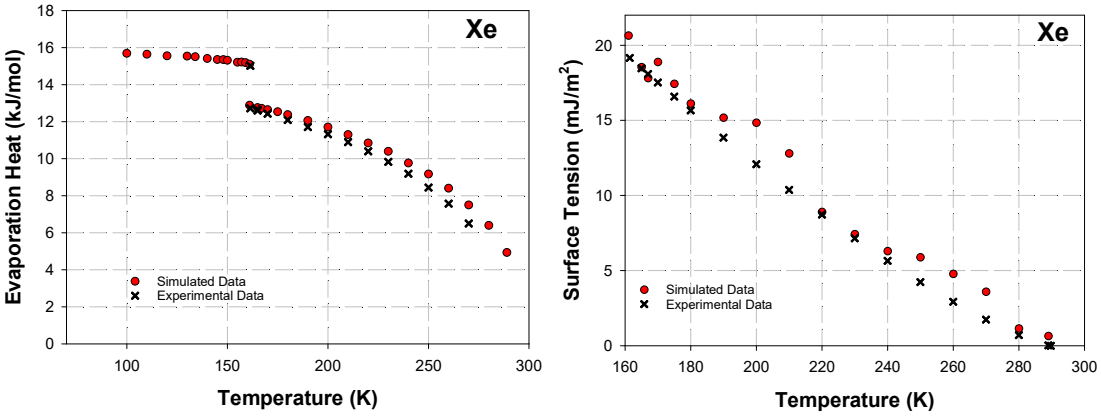

(c) (d)

Figure 3.3 (a) Liquid (solid)-vapour coexistence curves of Xe, (b) vapour pressure in semi-log scale, (c) evaporation heat and (d) surface tension. The experimental data above triple point in these figures are taken from the database of NIST Chemistry WebBook [172]; The experimental data of vapour pressure under triple point in (b) are taken from [173]; the experimental data of solid phase density under triple point in (a) are taken from [174]; the experimental data of sublimation heat under triple point in (c) are taken from [175]. Statistical uncertainties are smaller than the size of the symbols used in the above figures.

3.3.3 New Potential Model of Mercury

Unlike Ar, Xe and other LJ fluids, mercury has multi-body effect in nature as has been reviewed in Section 1.2.1. Therefore, the conventional form of *LJ* potential is suitable for *LJ* fluids, however, is not suitable for mercury. Although the existing conventional *LJ* potentials proposed for mercury are not good, they still can give information about the general scope of the molecular parameters. Some other potentials have made improvement by introducing the temperature factor to consider the multi-body effect; however, the forms of these potentials are not compatible in *MC* simulation. This section will be focused on the development process of a new potential for mercury which is based on the conventional form of *LJ* potential but has temperature-dependent molecular parameters. The above model evaluation process for Ar and Xe by studying the phase equilibria is applied in the development of the new mercury potential.

3.3.3.1 Existing Intermolecular Potential Models

Two conventional 12-6 *LJ* potentials

Mercury is modelled as a 1-centre *LJ* site, two sets of molecular parameters, collision diameter σ_{ff} and the reduced well depth ε_{ff}/k_B: 0.314 nm, 525.15 K (*Model A*) [50] and 0.261 nm, 1336.64 K (*Model B*) [54] were used as the initial guesses for the development of the new model.

Bomont-Bretonnet (*BB*) potential

Bomont and Bretonnet [54, 176, 177] suggested the following functional equations:

$$\varphi_{ff}(r) = A_0 \exp(-\alpha r) - A_1 \exp\left[-\beta\left(r - R_0\right)^2\right] \tag{3.1}$$

$$A_1(T) = \sum a_i T^i \tag{3.2}$$

Here only the parameter for the attractive term varies with temperature.

Raabe-Sadus (*RS*) potential

The equations of *RS* potential model are:

$$\varphi_{ff}(r) = \lambda_E \sum_{j=3}^{9} a_{2j} \left(\lambda_r r\right)^{-2j} - 45.77254 r^{-4.26957} \exp(-0.67264 r) + \frac{C_9}{r^9} \tag{3.3}$$

$$C_9 = -16020.46 - 2823.42\left(\frac{kT}{\varepsilon}\right) \tag{3.4}$$

The parameters in eqs. (3.3) and (3.4) can be found in [50]. Like the *BB* model, the temperature dependence of the potential equation is accounted for in the attractive term.

3.3.3.2 Comparison of Existing Potential Models

The *VLE* coexistence curves of mercury obtained with the four potential models described in Section 3.3.3.1 are shown in Figures 3.4a and b in linear and semi-log

scales to highlight the liquid and gas regions, respectively. Our simulation results with these potential models using the Bin-MC scheme agree well with those reported in the literature using different simulation methods, the Gibbs ensemble [50] and the expanded Wang-Landau scheme [178].

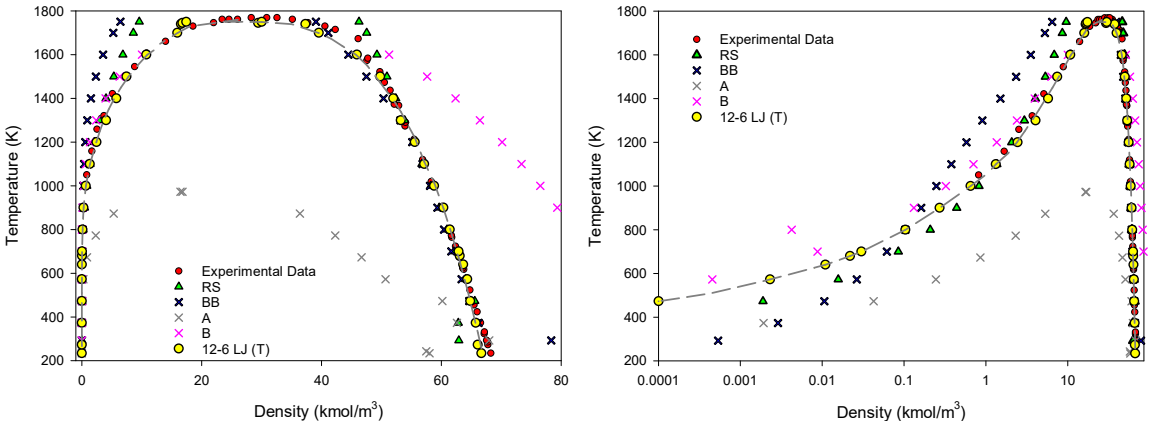

Figure 3.4 Liquid -vapour coexistence curves of mercury with various models in (a) linear scale and (b) semi-log scale. The experimental data are taken from [179]. Statistical uncertainties are smaller than the size of the symbols. The dashed line is the fitting curve for Model 12-6 LJ (T), with its estimated critical temperature of 1745 K.

The following points are derived from the simulations:

1. The conventional 12-6 *LJ* models are inadequate in describing the experimental data. Model A over-predicts the vapour phase density while under-estimates the dense phase density, and it gives a critical temperature of 1000 K, well below the experimental data. Opposite trend was observed for Model B.

2. The *BB* and *RS* models perform generally better than the 12-6 *LJ* models because of the allowance for the temperature dependence of the attractive term. The *RS* model describes better the gas phase while the *BB* model does it better for the dense phase. Both models, however, over-predict the critical temperature.

3. The deviation between the simulation results with the *RS* model and the experimental data increases with temperature. This is likely due to the linear dependence of the parameter C_9 on temperature [40, 52].

Other thermodynamic properties are presented in Figures 3.5a-d. For clarity, the results of the two 12-6 LJ models are not included because of their very poor description. Overall, the *RS* model describes reasonably the experimental data, but deviation is observed for temperatures greater than 1200 K. Since it is superior to the other models, it was taken as the reference for comparison with the new model developed in this work.

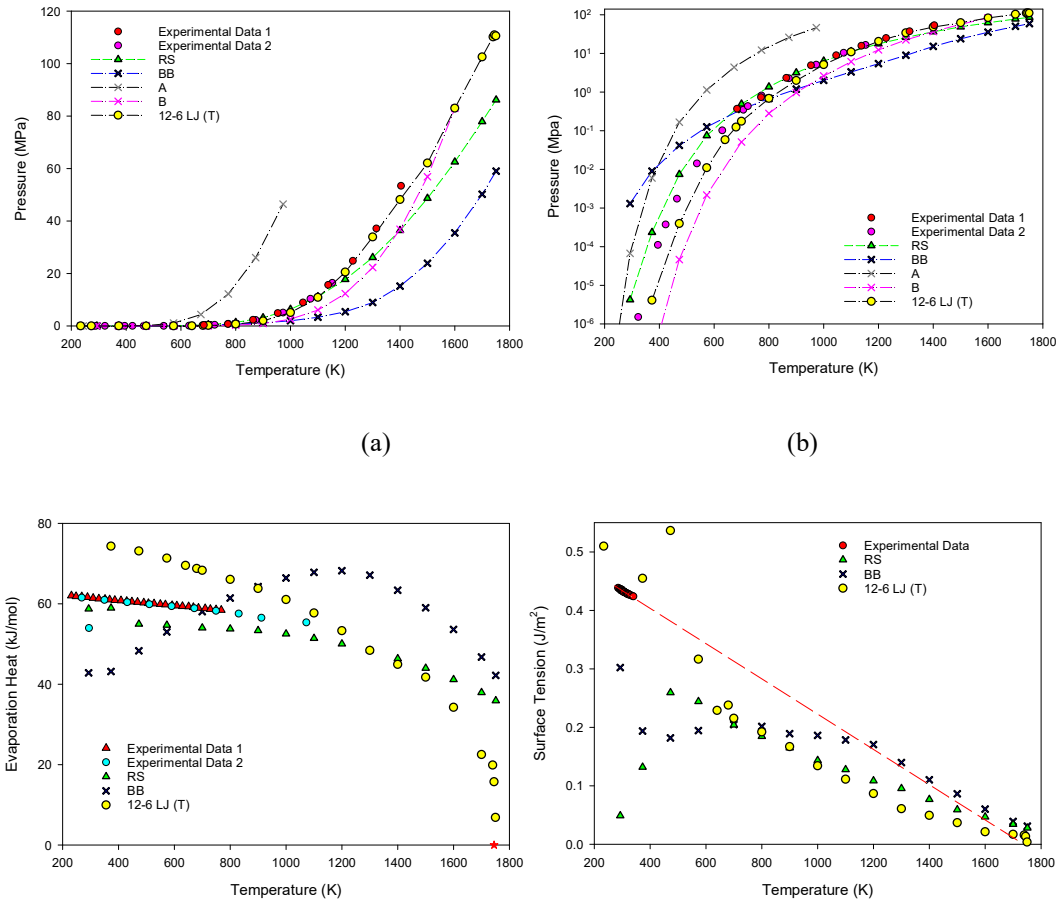

Figure 3.5 Thermodynamic properties of mercury versus temperature with various potential models, (a) vapour pressure in linear scale and (b) semi-log scale, (c) evaporation heat and (d) surface tension. The experimental data in (a) and (b) are taken from [180, 181]; the two sets of experimental data in (c) are taken from [50]; the experimental surface tensions in (d) are from [182]. Statistical uncertainties are

smaller than the size of each individual symbol used in the above figures. The estimated critical temperature 1745 K for Model 12-6 LJ (T) is shown with the red star symbol in (c).

3.3.3.3 The New Temperature-dependent LJ Model

As mentioned in [56], a high liquid density implies that the collision diameter is too small while a small saturation vapour pressure implies a large well depth of the intermolecular interaction energy. Based on the thermodynamic properties described by Models A and B in Figures 3.4 and 3.5, the collision diameter and the well depth of interaction energy should fall between those models. The *LJ* parameters are determined through trial and error methods of adjusting these two parameters for each temperature by matching the simulation results against the *VLE* experimental data. The search for the optimum parameters is aided with the corresponding parameters of the two conventional *LJ* models A and B. The matching was carried out for twenty temperatures spanning from the triple point temperature of 234 K and the critical point temperature of 1751 K.

With the new temperature-dependent LJ model given below,

$$u_{ff}(r,T) = 4\varepsilon_{ff}(T)\left[\left(\frac{\sigma_{ff}(T)}{r}\right)^{12} - \left(\frac{\sigma_{ff}(T)}{r}\right)^{6}\right] \tag{3.6a}$$

we derived the following temperature dependence of the molecular parameters:

$$\sigma_{ff}(T) = AT^2 + BT + C \;; \qquad \varepsilon_{ff}(T)/k_B = DT^E + F \tag{3.6b}$$

where the values of A-F are -4.415×10^{-9} nm/K^2, -1.086×10^{-5} nm/K, 0.2952 nm, 5.393×10^{-14} K$^{-3.811}$, 4.811 and 1176 K, respectively. The plots of $\sigma_{ff}(T)$, $\varepsilon_{ff}(T)$ and $\sigma^6\varepsilon$ versus temperature are shown in Figures 3.6a-b, and their values are listed in Table A1 of Appendix A. The collision diameter decreases by 8% and the well-depth of the interaction energy increases by 10% over the temperature range in the sub-

critical region. The product of $\sigma^6\varepsilon$ decreases with temperature, suggesting that the attraction becomes weaker with temperature, in agreement with the fact that mercury cluster size decreases with temperature as mentioned in Section 1.2.1.

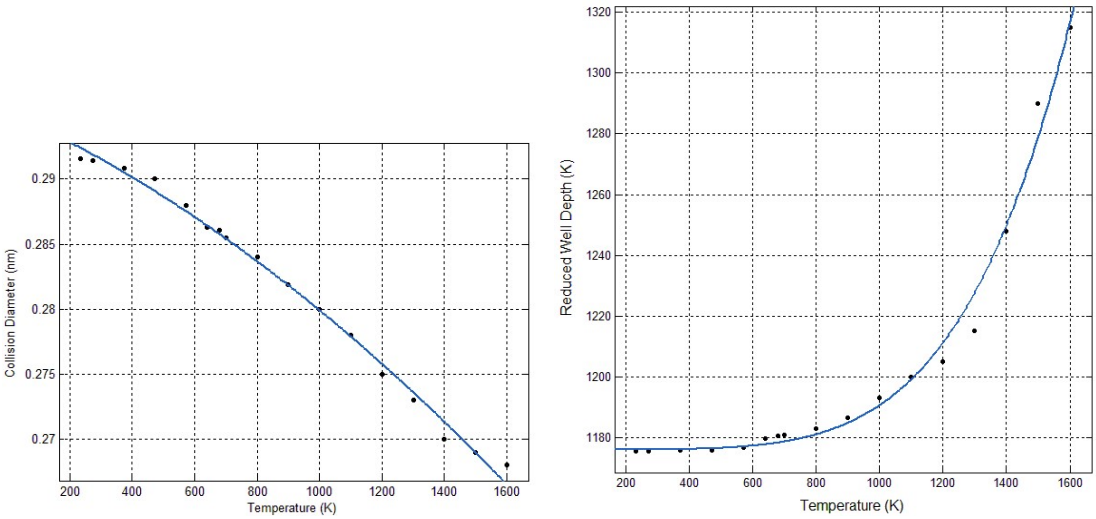

(a) (b)

Figure 3.6 (a) Collision diameter, and (b) reduced well depth as a function of temperature for the new 12-6 LJ (T) model of mercury.

3.3.3.4 Critical Properties Predicted with the New 12-6 LJ (T) Model

We adopted the method suggested in [183] to obtain the critical properties, ρ_C, T_C and P_C. The fitting equations are shown in eqs. (3.7) and (3.8). The superscript * denotes dimensionless unit.

$$\rho_{\pm}^{*} = \rho_C^{*} + C_2|t| \pm \frac{1}{2}\left(B_0|t|^{\beta} + B_1|t|^{\beta+1/2}\right) \tag{3.7}$$

where $t = 1 - T/T_C$ and $\beta = 0.325$

$$\ln P_V^{*} = A - \frac{B}{T^{*}} \tag{3.8}$$

The terms C_2, B_0, B_1, A and B are 0.0495, 0.8296, 5.1494×10^{-5}, 2.422 and 5.867, respectively. The critical properties derived from our model are: T_C=1745 K, ρ_C

=2.98×10^4 mol/m^3, and P_C =1.28×10^8 Pa, comparing well with 1750 K, 2.89×10^4 mol/m^3 and 1.72×10^8 Pa of the experimental data, respectively.

3.3.3.5 Performance of the New 12-6 LJ (T) Model

The thermodynamics properties obtained with this new 12-6 *LJ* (T) potential are shown in Figures 3.4 and 3.5. A number of points are drawn:

1) The new model generally describes better the liquid-vapour coexistence curve (Figure 3.4), and it gives the saturation vapour pressure better than the *RS* model.
2) Although there are some deviations in the heat of evaporation, the new model performs far better than the other models.
3) The surface tension is not well described by any model, but the new model gives the best description overall. It must be borne in mind that the description of the surface tension depends on the choice the system size, the cut-off radius and the use of the long range correction [184].

Apart from the above thermodynamics properties, the potential profiles of the new 12-6 *LJ* (T) model were compared with other models as presented in Appendix B. For a given temperature the profile of the new model falls between those of the two conventional 12-6 *LJ* models. The same trend is observed when the potential curves of *RS* model are compared with those of the new model.

3.4 Conclusions

In this chapter, through the *VSE* and *VLE* studies with Bin-CMC scheme over a wide range of temperature, we have found that the selected potential models of Ar and Xe can predict their corresponding bulk phase behaviours (gas, liquid and solid phases) and agree well with the experimental data of other thermodynamic properties (saturation vapor pressure, enthalpy of phase change and surface tension). Triple point

can also be captured by simulation indicated as the discontinuity in dense phase density and enthalpy of phase change, and matches well with the experimental value. Therefore, we are confident that these two potential models of Ar and Xe are appropriate and ready for the subsequent adsorption studies as both *VSE* and *VLE* can be well described.

We developed a practical potential model for mercury by allowing for the temperature dependence of the molecular parameters, to describe the thermodynamic properties of the vapour-liquid equilibrium. While the intermolecular energy of mercury is long-ranged, the engineering model proposed in this paper incorporates it into the dispersion parameters, in the same way as the common practice in simulation that the three-body interactions are embedded in the lumped parameters of the pairwise interaction. Although the model is empirical at best, we capture the description of the vapour-liquid equilibrium with this engineering potential model, and argue that its correct description is a prerequisite for the description of the non-uniform distribution of molecules in an adsorption system. In our model the collision diameter (σ) decreases while the well-depth of the energy interaction (ε) increases with temperature, with their product $\sigma^6\varepsilon$ decreasing, indicating that the intermolecular attraction decreases as the temperature increases. The critical temperature estimated with this new potential model is 1745 K, which is in excellent agreement with the experimental data. The same is also true for the critical density and the critical vapour pressure.

Chapter 4. Adsorption in Wedge Pores

4.1 Introduction

The wedge pore model, among other non-uniform pore models, has been studied with *GCMC* simulation [169], and it was suggested as a suitable model for the characterization of carbonaceous materials [79, 90, 105, 185, 186]. The two parameters of a wedge, the angle and the axial length, have significant effects on the shape of the hysteresis and the structure of the adsorbate [105, 169, 187]. When the wedge angle is sufficiently small, the simulated isotherm can exhibit a stepwise behaviour in the desorption boundary of the hysteresis loop, for example argon adsorption at 77 K in a graphitic wedge [90]. This was explained as the result of the alternate commensurate and incommensurate packings along the axial direction of the wedge [188]. The first objective of this chapter is to investigate systematically the mechanisms of the step-wise behaviour for a wider range of temperature to determine the bifurcation temperature above which the domain of commensurate packing disappears. Here we chose xenon as a model adsorbate because of its stronger intermolecular energy, twice as strong as argon [37], so that the packing could be facilitated and studied on the step-wise behaviour. Moreover, the operating temperature range (including the boiling point) of xenon is higher than that for commonly used argon and nitrogen, making it a potential adsorbate for use in all commercial pore size analysers, nowadays equipped with cryostat, and the potential use of isotherms at more than one temperature to derive better pore size distribution.

One of the most controversial issues in adsorption study is whether hysteresis exists in closed-end pores, however, past research has focused mainly on closed-end pores of either slit or cylindrical shape and little attention has been paid to closed-end wedge pores [188], despite of the fact that the pore size in practical solids is not uniform along the axial direction of the pore [98]. The wedge model, despite of its simplicity, captures this non-uniformity, this approach is regarded as the paradigm shift in the modelling

of adsorption with the implication of better characterization of porous carbonaceous solids. It is the second aim of this chapter to address the possible presence of hysteresis in the isotherm for gas adsorption in wedge pores and to derive the microscopic reason behind hysteresis.

4.2 Simulation Details

GCMC Simulation

For an open wedge system, we used 3×10^5 cycles in both the equilibration and sampling stages, and in each cycle there are 1000 trial moves of displacement, insertion and deletion, chosen with equal probability, giving a total of 3 billion configurations. This was found to be more than adequate to achieve equilibrium. For a closed wedge system, we used at least 1×10^6 cycles in both the equilibration and sampling stages.

In the equilibration stage, the maximum displacement length is initially set as half of the largest dimension of the box and adjusted at the end of each cycle to give an acceptance ratio of 20% [189], and it is kept constant in the sampling stage. The length of the simulation box in the *x*-direction is 10 times the collision diameter of xenon. The gas surrounding at the ends of the pore has a length of 3 nm along the *y*-axis, and the dimension in the *z*- direction is the same as the pore width of the large end. The cut-off radius for the energy calculation is 5 times the collision diameter of xenon.

2V-NVT Simulation

To carry out simulations with the canonical ensemble, we used the *2V-NVT* scheme for which there are two boxes: the adsorption system and the gas reservoir. The dimensions of the former are the same as that used in the *GCMC* simulations. For the gas reservoir box, one of its linear dimensions (*z*-) is 1×10^4 nm, which is large enough to ensure that there are enough number of molecules for reliable determination of density and pressure, and the other two dimensions (*x*- and *y*-) are the same as those of the adsorption box. In addition to the trial of displacement of molecule in both boxes,

exchange of molecule between the two boxes is another trial move. The ratio of the probabilities for the displacement and exchange trial moves is 2:1.

4.3 Results and Discussions

4.3.1 Xenon Adsorption in Open Wedge at 134K

The adsorption-desorption isotherm in the reference open wedge pore (SH = 3.15 nm, L = 16.2 nm and α = 3.5°) at 134K, well below the triple point is presented in Figure 4.1. It exhibits Type *C* hysteresis (de Boer classification) with a remarkable feature of multiple steps along the desorption boundary of the hysteresis loop. Four distinct steps are observed, instead of the usual one step as described by Type *C*.

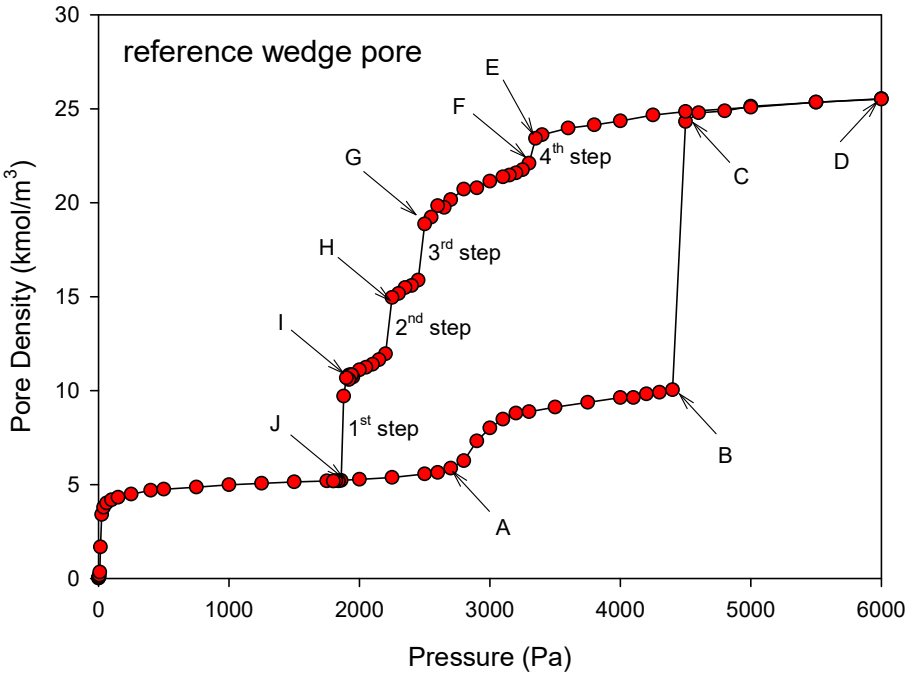

Figure 4.1 Isotherm of xenon adsorption at 134 K in the reference open wedge pore (SH = 3.15 nm, L = 16.2 nm and α = 3.5°). The sublimation pressure is 10.8 kPa.

To shed light into the underlying mechanisms of adsorption and the multiple steps along the desorption boundary, we showed in Figure 4.2 the snapshots for various points marked in Figure 4.1.

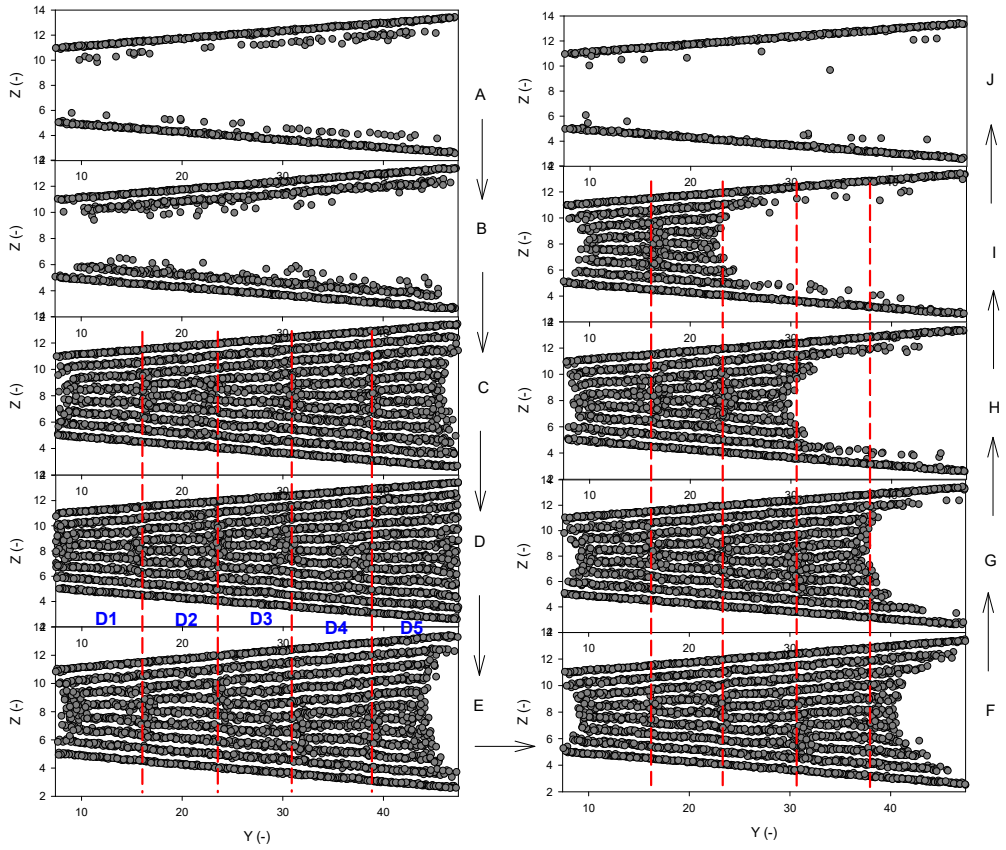

Figure 4.2 Snapshots of xenon adsorption at 134 K in the reference pore. The points A to J are marked in Figure 4.1.

Adsorption branch

At Point *A* along the adsorption path, molecules build up on the pore walls by a molecular layering mechanism, and this proceeds until Point B, at which the adsorbed films on the opposite walls at the small end of the pore are close enough to induce the filling at Point *C*, and the filling extends all the way to the pore mouth of the large end. At this point the interface separating the adsorbed phase and the gas phase is concave, with its radius of curvature satisfying the Kelvin equation at $P_B = P_C$. Had the wedge been much longer, the condensation does not extend right to the pore mouth, but rather the interface stops at the distance along the axial direction such that its radius of curvature is governed by the Kelvin equation [90, 169].

Further increase in pressure from Point *C* results in molecules building up at the pore mouth with a decrease in the curvature of the interface, and this proceeds until the

saturation vapour pressure has been reached.

During the course of filling from Point *B* to *C*, we observe a clear formation of domains (labelled as *D1* to *D5* in Figure 4.2), each of which has a constant number of molecular layers, commensurately packed across the pore, and the number of layer is incremented by one across any two adjacent domains. This is a feature of bifurcation with one layer bifurcated into two [188].

Desorption branch

As the pressure is decreased from the completely filled pore (Point *D*) to Point *E*, the interfaces from both ends of the pore recede into the interior, with greater extent at the large end. This continues until the domain *D5* near the large end is evaporated at Point *F*, resulting the first step (4^{th} step marked in Figure 4.1) along the desorption boundary of the hysteresis loop. A further reduction in the pressure from Point *F* to *G*, we see the gradual removal of molecules in the junction between the domains *D4* and *D5*. The sequence of the sharp evaporation of the domain and the gradual evaporation of the junction are repeated for the remaining domains, resulting in the multiple steps along the desorption boundary of the hysteresis, with the exception of the last domains *D1* and *D2*, which are evaporated simultaneously because of the recession of the interface at the small end.

To understand better the effects of the interactions between molecules and the pore walls on the domains and junctions, we plotted in Figure 4.3 the distribution of the solvation pressure along the axial direction of the pore, and identified a number of distinct features:

a) The solvation pressure oscillates with a damped amplitude because of the increasing pore width along the axial direction of the wedge. This is consistent with the variation of the solvation pressure in uniform sized slits of different width [190].

b) The solvation pressures at the junctions are positive because molecules are under expansion to attempt adding one additional molecular layer to form the next domain. The solvation pressure in most part of any domain is negative, indicating the highly structure of the adsorbate that has the tendency to pull the walls to the adsorbate to maximize the solid-fluid interactions [146].

c) In each domain, there exists two locations where the solvation pressure is zero because of the positive solvation pressure in the junction and the negative solvation pressure in the most part of the domain.

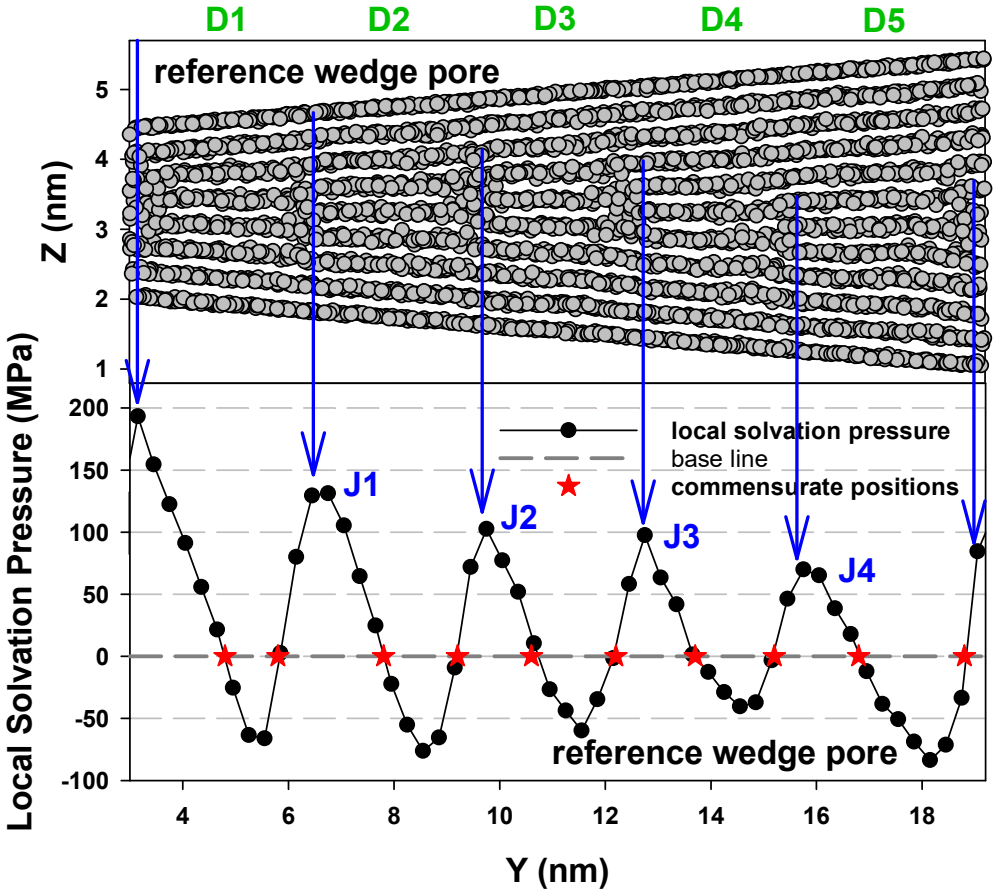

Figure 4.3 The distribution of the solvation pressure at 134 K along the reference pore at the saturation pressure. The five domains are labelled as *D1* to *D5*, and the four junctions are labelled as *J1* to *J4*.

Figure 4.3 also shows that the length of the domain is constant (3.2 nm), which is expected because of the linear increase in the pore width along the axial direction, and this length is required to add one additional layer as we move from one domain to the next. This is a function of the wedge angle, and the domain length is greater for smaller

wedge angles. It is also a function of temperature as when the temperature is increased the domain length remains the same until a bifurcation temperature is reached, beyond which there is no clear formation of domains and junction because of the thermal fluctuations. For temperatures greater than the bifurcation temperature, the isotherm is reversible.

For comparison between the behaviour of the solvation pressure in a wedge and that in a slit, we showed in Appendix D the solvation pressure for slits whose widths are the same size as the sizes at the junction and the domain. We chose the pore size of 3.57 nm at the junction *J1*, and the pore size of 3.69 nm in the domain *D2* (corresponding to the 3rd red star from the left in Figure 4.3). As expected, the 3.57 nm slit pore shows disordered configuration, typical for incommensurate packing, while the 3.69 nm slit pore yields distinct molecular layers as evidenced in the distinct peaks in the local density distribution across the pore (Figure D1d).

4.3.2 Effects of Temperature

Figure 4.4 shows the isotherms for temperatures in the range between 134 K (below the triple point T_{tri}) to 200 K (above T_{tri}), and Figure 4.5 shows the corresponding snapshots at the saturation vapour pressure to study the effects of temperature. A number of features can be derived:

a) Type *C* (de Boer classification) hysteresis is observed for all temperatures, and the hysteresis loop shifts to a higher relative pressure and shrinks in size as the temperature is increased.
b) The number of steps in the desorption boundary of the hysteresis remains unchanged until the triple point (161 K) is reached. At 165 K, the last three steps vanish, as seen in the disordered structure of the last three domains. This result suggests that the bifurcation temperature of the last three domains is between 161 K and 165 K.

c) The size of the domain is independent of temperature for temperatures less than the bifurcation temperature, and it is a function of the wedge angle only.

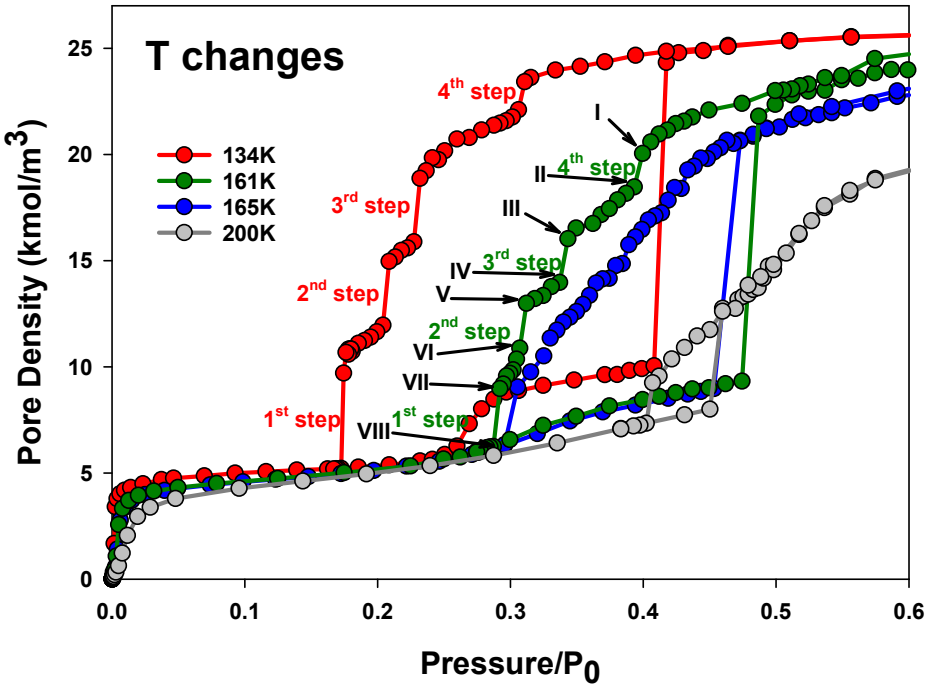

Figure 4.4 Plots of isotherms of xenon adsorption in terms of the reduced pressure for the reference pore at various temperatures. The saturation vapour pressure (P_0) at different temperatures used are determined by the Antoine equation [191], and the values are tabulated in Appendix C.

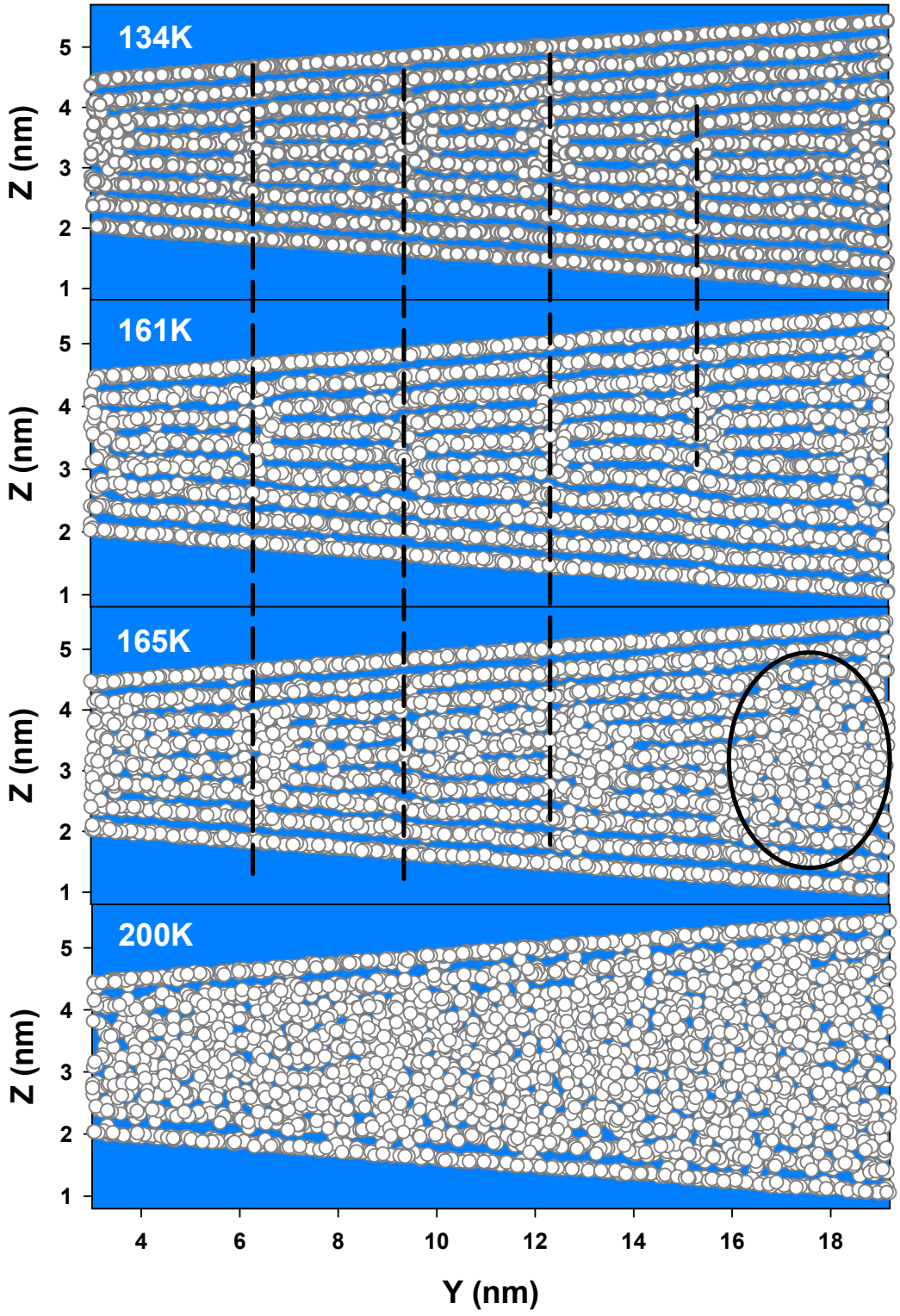

Figure 4.5 Snapshots of molecules in the reference pore at the saturation vapour pressures for various temperatures.

Although the number of steps along the desorption boundary of the hysteresis loop at the triple point (161 K) is the same as at 134 K, there is a subtle different in the mechanisms of the evaporation. Figure 4.6 shows that the 4th step in the desorption boundary is due to the evaporation of the domains *D4* and *D5* for 161 K and 134 K, respectively. This is because of the greater thermal motion of molecules at higher temperature, which results in the gradual evaporation of the domain *D5*. This has an effect on the evaporation of the subsequent domains, for example the last step is associated with the evaporation of the domain *D1* for 161 K, while it is associated with the domains *D1* and *D2* for 134 K, which is due to the greater cohesiveness of the domains *D1* and *D2*, as seen in Figure 4.7.

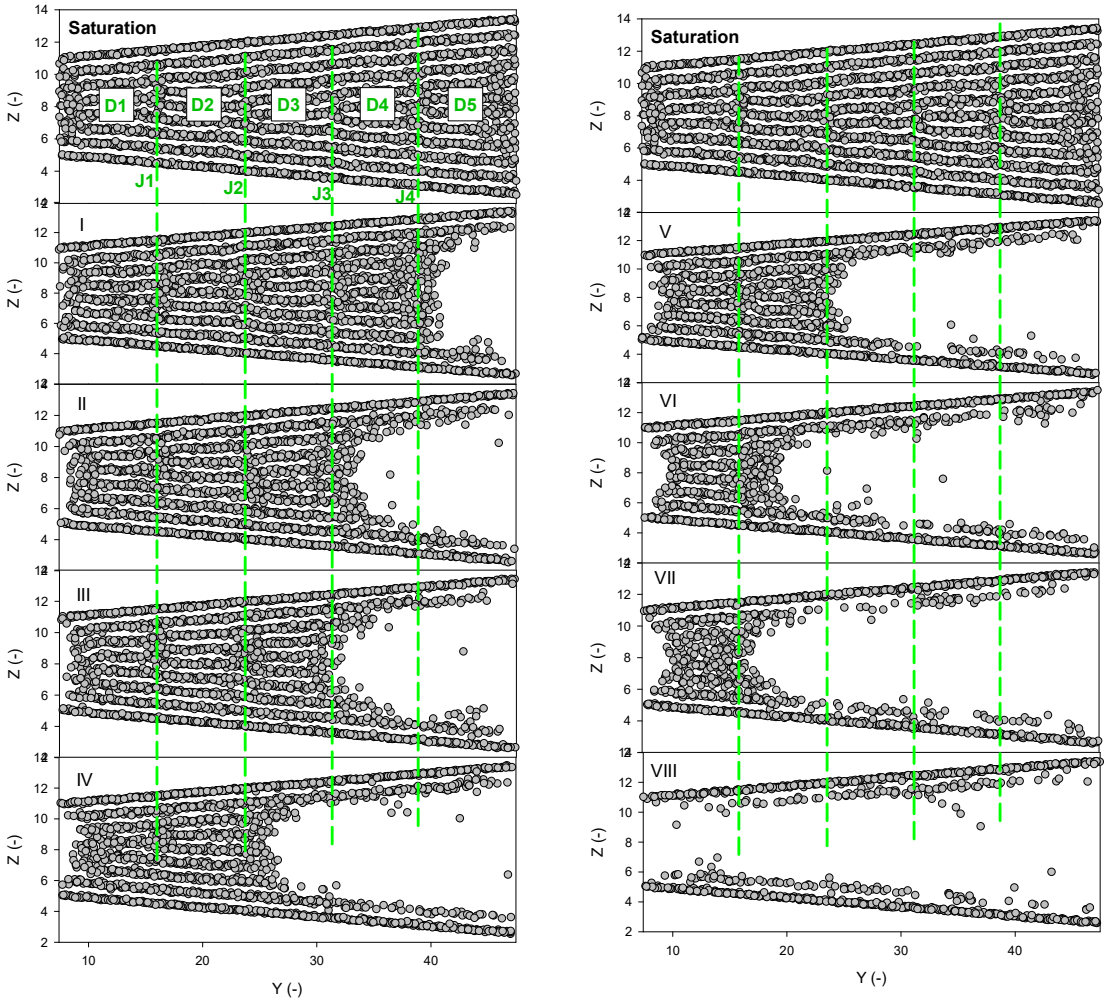

Figure 4.6 Snapshots of xenon adsorption at 161 K in the reference pore for the points I to VIII as labelled in Figure 4.4.

Figures 4.7a and b show the distributions of the solvation pressure and the average molecular potential energy along the axial direction of the reference wedge at various temperatures. The amplitude of the oscillations of the local solvation pressure decreases with temperature, indicating the greater cohesiveness of the domains at low temperatures. The same conclusion could also be made for the average molecular potential energy, which follows the inverse oscillatory pattern as of the solvation pressure, i.e. the molecules at the junctions has higher potential energies. The amplitude of the potential energy is smaller with temperature.

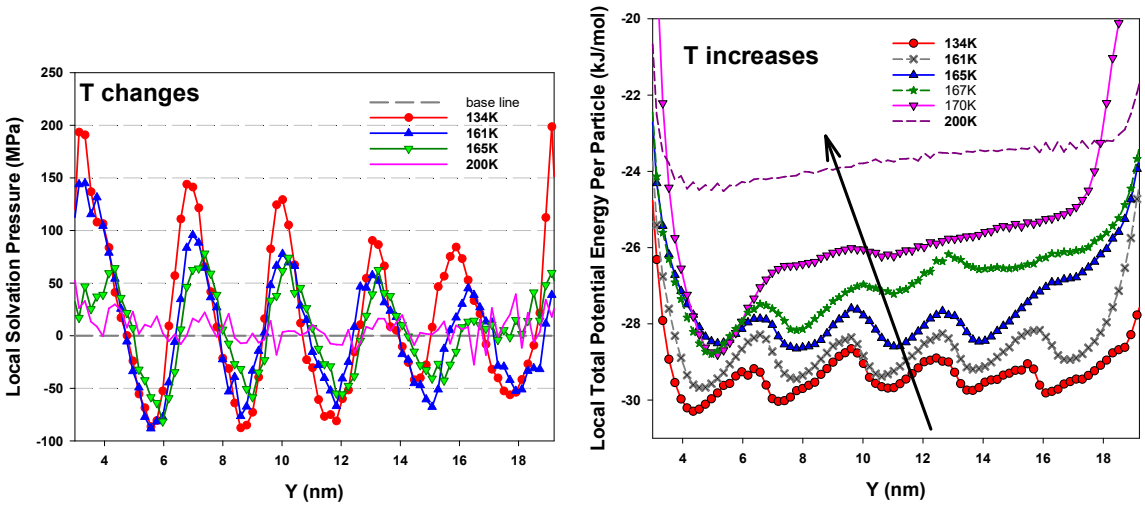

(a) (b)

Figure 4.7 (a) Local solvation pressure distribution and (b) local molecular potential energy distribution for various temperatures at the saturation vapour pressures at 134 K in the reference pore.

The step-wise behaviour for xenon is more pronounced than for argon, and this is attributed to its stronger intermolecular interactions (detailed comparison between xenon and argon adsorption is shown in Figure E in Appendix E).

4.3.3 Effects of Pore Length

As shown in Section 4.3.1, the positions of the junctions *J3* and *J4* at 134 K for the reference pore are 9.8 nm and 13 nm, respectively, from the small end. The length of this reference pore is 16.2 nm. Figure 4.8a shows the isotherms at the same temperature for the reference wedge and the wedges having shorter lengths of 9.8 nm and 13 nm,

keeping other parameters the same. The condensation pressures remain unchanged as it is governed by the adsorbate at the small end, while the evaporation pressures for various steps shift to lower pressures for shorter wedges, which is due to the enhanced solid-fluid interactions at the large end because of smaller width of *BH*. As expected, the number of steps is smaller for shorter wedges, and this is seen in the snapshots at the saturation vapour pressure in Figure 4.8b.

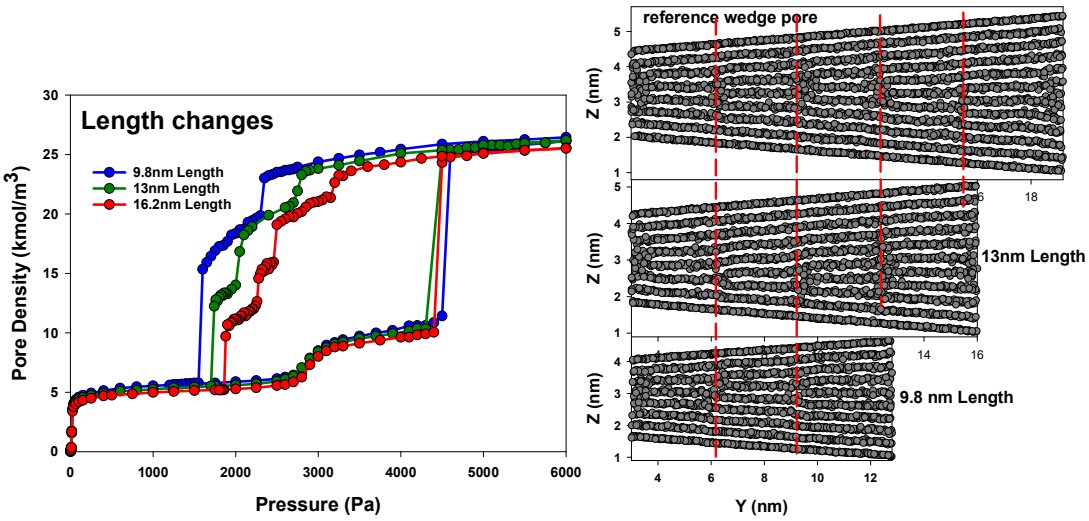

(a) (b)

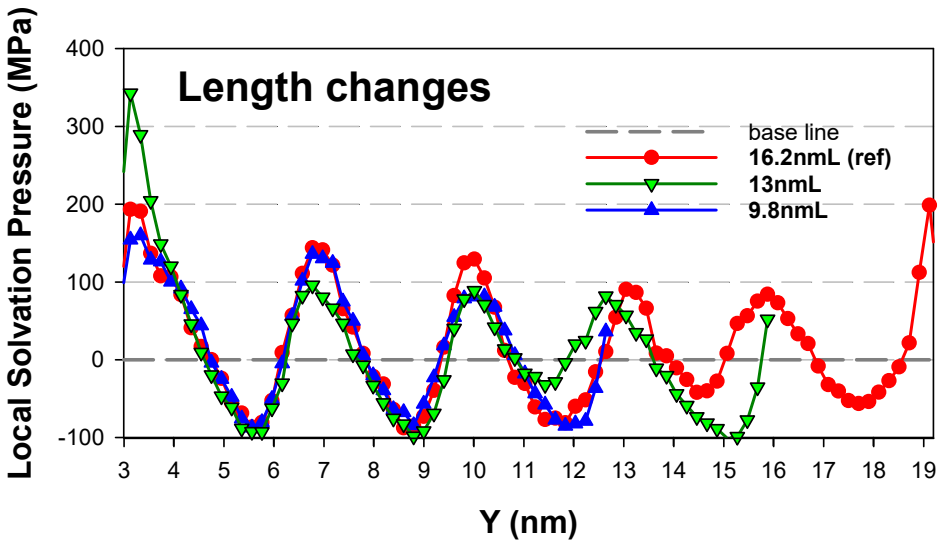

(c)

Figure 4.8 (a) Isotherms, (b) snapshots and (c) local solvation pressure distribution at the saturation vapour pressures at 134 K in wedge pores of length 9.8 nm, 13 nm and 16.2 nm.

From the snapshots and the local solvation pressure distribution in Figure 4.8b and c, the pore length has no effects on the positions of the junctions, as physically expected because the length of a domain is governed only by the wedge angle that we have discussed earlier. It is worthwhile to note that the two domains near the small end evaporate simultaneously for wedges of different lengths.

4.3.4 Effects of Angle

The effects of varying the wedge angle on the stepwise behaviour of the desorption boundary of the hysteresis loop are studied for the following two cases:

Case I: The wedge angles are 2.8°, 3.5° and 4.2°, keeping the axial length and the width of the small end constant (16.2 nm and 3.15 nm, respectively). The widths at the large end for these angles are 4.73 nm, 5.13 nm and 5.53 nm, respectively.

Case II: We keep the widths of the small end and the large end constant at 3.15 nm and 4.73 nm, and study the wedge angles are 2.8° and 3.5°, for which the axial lengths are 16.2 nm and 13 nm, respectively.

The geometrical parameters of these wedge pores are summarized in Table 4.1.

Table 4.1 The geometrical parameters of the wedge pores.

Pore	Length (nm)	SH (nm)	Angle (°)	BH (nm)	No. steps	J1 (nm)	J2 (nm)	J3 (nm)	J4 (nm)	J5 (nm)
Ref	16.2	3.15	3.5	5.13	4	3.57	3.96	4.35	4.74	
Case I	16.2	3.15	4.2	5.53	5	3.57	3.96	4.33	4.75	5.15
	16.2	3.15	2.8	4.73	3	3.55	3.95	4.32		
Case II	13	3.15	3.5	4.73	3	3.57	3.96	4.35		

Figure 4.9 shows the isotherms for Case I, the adsorption and desorption branches shift to lower pressures, which is due to the enhancement in the solid-fluid interactions in the wedge with smaller angle. The number of steps for a given axial length increases with the wedge angle because of the shorter length of the domain, i.e. it takes shorter length in a given domain to bifurcate into the next domain (Figure 4.9b). As a consequence, it is not surprising that the pore widths where the junctions are formed

are independent of the wedge angle, which are summarized in Table 4.1. This is also supported by the local solvation pressure distribution versus the wall-wall separation in Figure 4.9c.

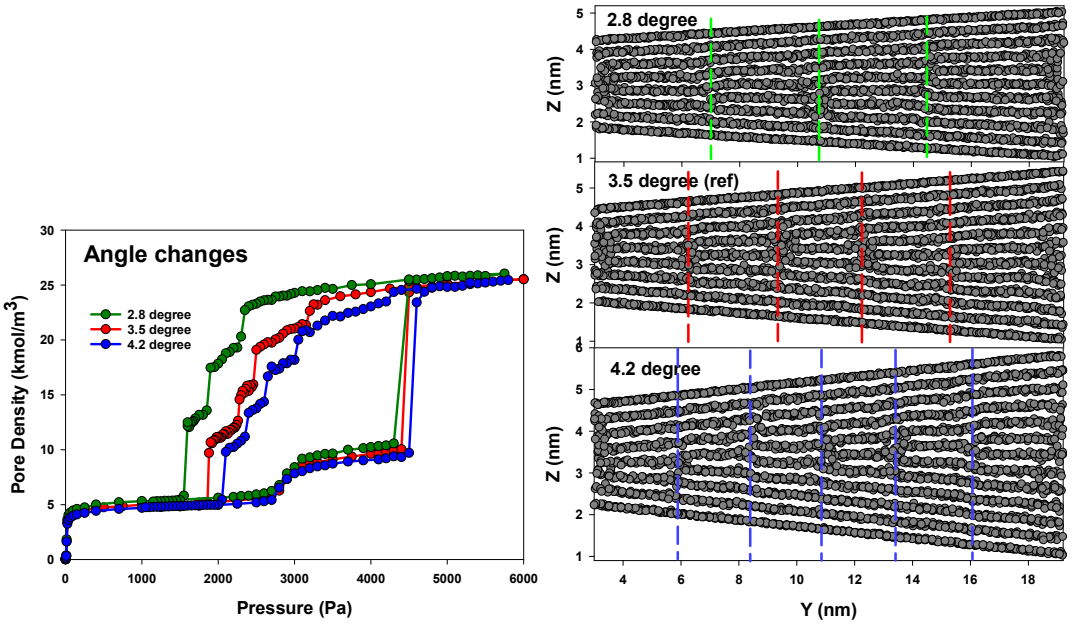

(a) (b)

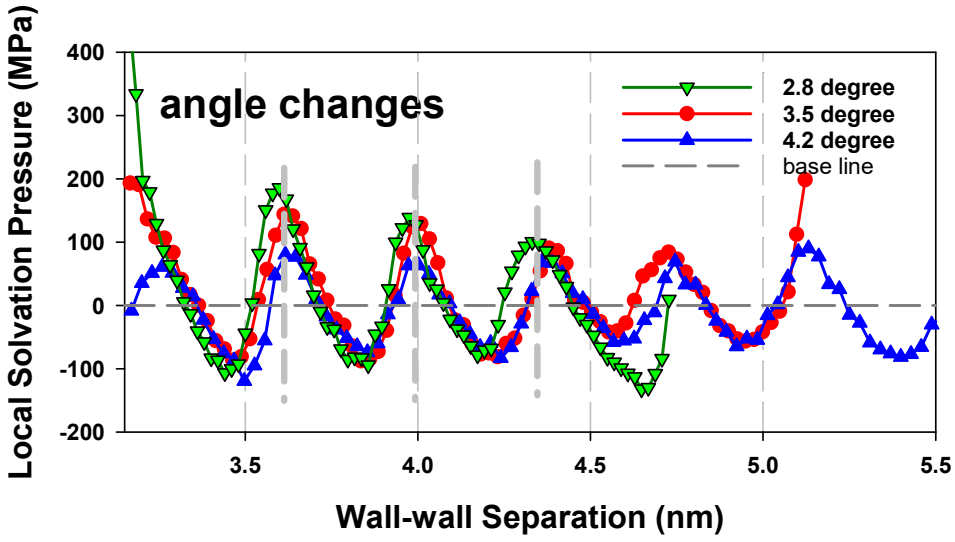

(c)

Figure 4.9 (a) Isotherms, (b) snapshots and (c) local solvation pressure distribution at the saturation vapour pressures at 134 K for wedge pores of different angle α = 4.2°, 3.5° and 2.8°.

For a smaller angle of 2.1° the evaporation mechanism of the last step along the

desorption boundary switches from the simultaneous evaporation of the two domains at the small end to sequential evaporation, due to the enhanced *SF* potential at the small end (Figure F1 in Appendix F).

Figure 4.10a shows the isotherms for Case II, and they exhibit almost the same behaviour for the different sets of angle and pore length, with the exception that the desorption branch shifts to lower pressure for the wedge with smaller angle, which is, once again, due to the enhanced *SF* interactions.

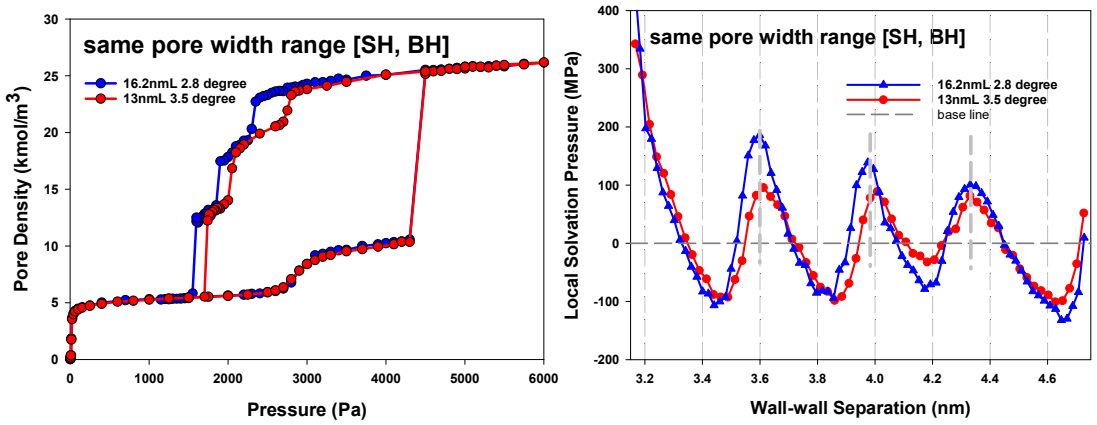

(a) (b)

Figure 4.10 (a) Isotherms and (b) local solvation pressure distribution at saturation pressures at 134 K in two wedge pores of different wedge angle and pore length, while keeping the widths at the small and large ends constant.

4.3.5 The Cohan Equation

The Cohan equation (eq. 2.37) is detailly presented in Section 2.3.11. Although this equation was derived for a cylinder, we shall assume that its functional form is valid for wedges, where the adsorbate is formed on the pore walls as two adsorbed films and the hemi-cylindrical interface is at the location where the two films meet. This approach was used by Barrer et al. [192] in their theoretical study of condensation and filling in single pores of different shape.

If the adsorbate in a wedge is assumed to have the same properties of the supercool liquid, i.e. its properties, saturation vapour pressure, surface tension and liquid molar

volume, are extrapolated from those corresponding properties in the vapour-liquid equilibrium (*VLE*) region, we used the Cohan equation in eq. (2.37) to calculate the radius of curvature of the interface for a given pressure. This is then compared with the simulated radius of curvature determined from Monte Carlo simulations (Section 4.3.5.2), to justify the assumption of supercooled liquid of the adsorbate.

4.3.5.1. Supercool liquid of bulk phase

We first determined the simulated bulk coexistence pressure, which is the equilibrium pressure between the condensed phase and the gas phase, the liquid molar volume and the surface tension for xenon in the temperature range between the bulk triple point and critical point temperatures (vapour-liquid equilibrium region), and they are tabulated in Appendix G. They are then used in the extrapolation to determine the properties for the supercooled liquid xenon at 134 K as 16 kPa (compared to the simulated sublimation pressure of 6.7 kPa), 4.4×10^{-5} m^3/mol and 24 mJ/m^2, respectively. Having these values, we used the Cohan equation (eq. 2.37) to estimate the radii of curvature of a cylindrical interface at various values of pressures less than the saturation vapour pressure for the supercool adsorbate at 134 K, and they are tabulated in Table 4.2.

Table 4.2 The radii of curvature of the interface separating the adsorbed phase and the gas phase for various values of pressure less than the saturation vapour pressure of 16 kPa for supercooled xenon, assuming that the interface is cylindrical and the adsorbate is liquid-like for xenon at 134 K.

P (kPa)	*r (nm)*
2.75	0.692
2.80	0.702
2.90	0.720
5.00	1.230
16.0	∞

4.3.5.2. Simulation results of adsorbate

Figure 4.11 presents the grand canonical isotherm for xenon adsorption at 134 K in a closed-end graphitic wedge pore with L=32.8 nm and α= 3.5 degrees. The snapshot of

a molecular configuration at the bulk sublimation pressure of 6.7 kPa (Point E) is shown in Figure 4.12 to show how the adsorbate is structured from the apex.

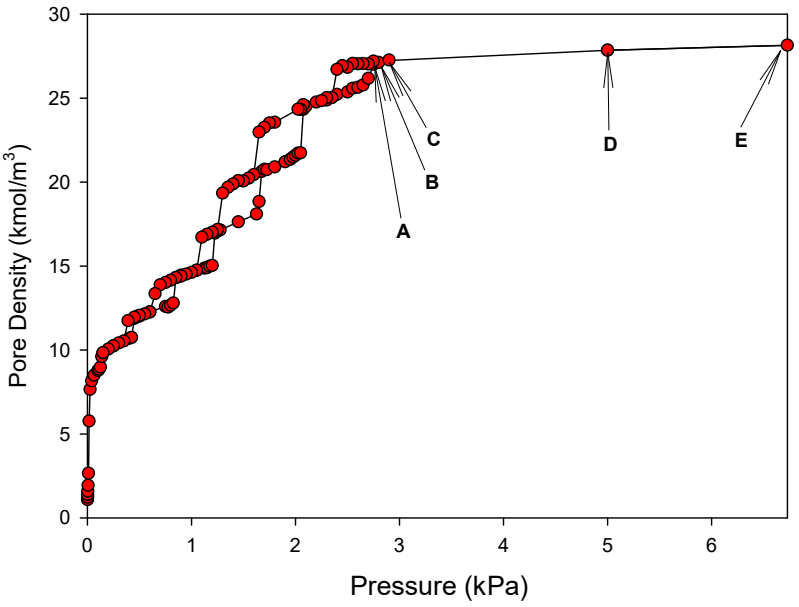

Figure 4.11 The grand canonical isotherm for xenon adsorption at 134 K in a closed-end graphitic wedge pore with L=32.8 nm and α= 3.5°.

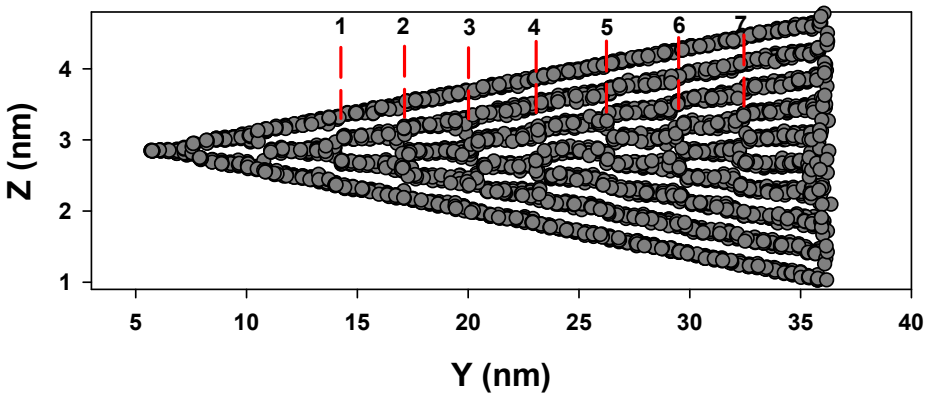

Figure 4.12 Snapshot of the molecular configuration at the bulk sublimation pressure for xenon adsorption at 134 K in a closed-end graphitic wedge with L=32.8 nm and α= 3.5°.

Beyond the seven hysteresis loops observed in the isotherm, the adsorbate has an interface separating it from the bulk gas phase (Points A to E in Figure 4.11). A snapshot in Figure 4.12 is one of the possible configurations for the adsorbate, and the better representation is the 2D-smoothed density distribution as shown in Figure 4.13,

where we see a clear interface with a disordered region of the condensed phase near the interface. The pressures and the radii of curvature are determined and subsequently used in the functional form of the Cohan equation to derive the properties of the adsorbate. The interface is determined from the 2D-smoothed density distribution and its radius is estimated by matching a circle of radius *r* against the curvature of the interface, and Figure 4.13 shows a typical distribution for *Point* D (as marked in Figure 4.11). We tabulated in Table 4.3 the radii of curvature and the pressures for Points A to D, and they are consistently greater than the values obtained by assuming the adsorbate as supercool-liquid-like (Table 4.2).

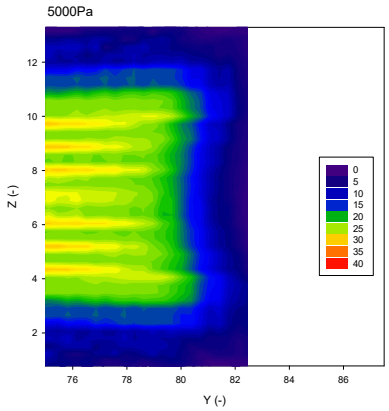

Figure 4.13 The 2D local density distribution and the contour of constant density for xenon adsorption at 5 kPa (*Point* D in Figure 4.11) at 134K in a closed-end graphitic wedge with L=32.8 nm and α= 3.5 degrees.

Table 4.3 The radii of curvature derived from the simulation for Points A, B, C and D in Figure 4.11.

P_A (kPa)	r_A *(nm)* (MC)
2.75 (A)	0.696
2.80 (B)	0.709
2.90 (C)	0.750
5.00 (D)	1.307

Given the radii of curvature for various pressures as derived from the simulation (Table 4.3), we used the form of the Cohan equation (eq. 2.37) to determine the

thermodynamic properties of the adsorbate. We rearrange this equation in a linear form,

$$lnP_A = lnP_0^* - (\gamma V_m/RT)\frac{1}{r_A} \tag{4.1}$$

so that we can derive the coexistence pressure between the adsorbate and the gas, P_0^*, and the energy parameter $\gamma V_M/RT$ from the linear plot of the logarithm of the pressure versus the inverse of the radius of curvature. They are listed in Table 4.4. It is seen that the derived coexistence pressure between the adsorbate and the bulk gas, which is the equilibrium pressure at which the adsorbate and the gas phase coexist, P_0^* =10 kPa, is less than the supercool liquid vapour pressure of 16 kPa and is greater than the bulk sublimation pressure of 6.7 kPa. This suggests that the adsorbate at 134 K is denser than the supercool liquid and not as structured as the bulk solid because the geometrical constraint of the wedge prevents the adsorbate to form a *fcc* structure of the bulk solid, which is also proved by the comparison of their radial density distributions at 134 K in Figure 4.14. It is substantiated with the smaller energy parameter, $\gamma V_M/RT$. This observation is true for other temperatures less than the bulk triple point temperature.

Table 4.4 The comparison of P_0 and $\gamma V_M/RT$ of the Cohan equation (eq. 2.37), obtained from two different approaches: (1) assuming the adsorbate as supercool liquid, and (2) direct simulation of the adsorbate as a function of pressure.

	Supercool Liquid data	MC simulation
P_0 (kPa)	16.0	10.0
γV_m/RT (nm)	0.96	0.9

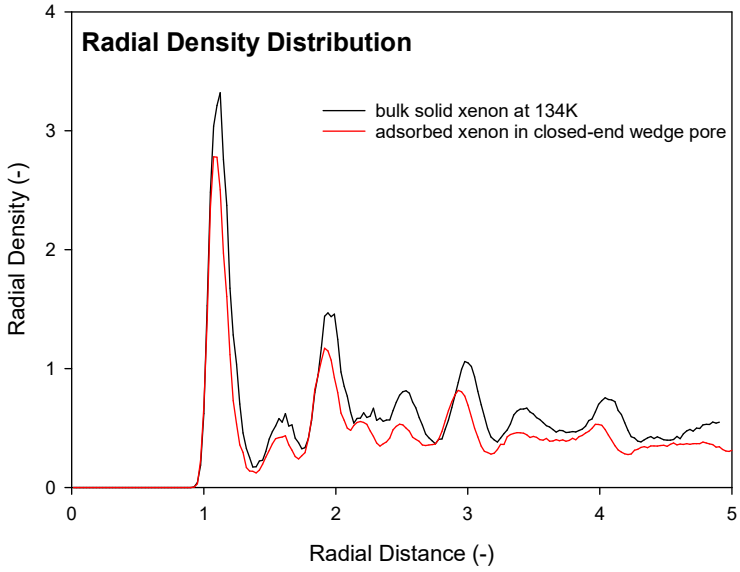

Figure 4.14 The radial density distributions of the bulk solid xenon and the adsorbed xenon in a closed-end graphitic wedge with L= 32.8 nm and α= 3.5 degrees, both at 134 K.

4.3.6 The Effects of the Closed End

The adsorption behaviour in open wedge pore has been previously studied [90, 188, 193], and subject to the pore dimensions hysteresis might occur, even for temperatures greater than the triple point because adsorption and desorption follow different paths. To show the effect of the closed end on the hysteresis, we plotted in Figure 4.15a the grand canonical isotherm for the open end graphitic wedge [193], with its small open end truncated at Point 5 marked in Figure 4.12 for the closed end wedge pore. The snapshot of the molecular configuration of this open wedge at the sublimation pressure is shown in Figure 4.15b, and for comparison we also show the snapshot for the corresponding closed end wedge. We observed the positions of alternate domains and junctions remain the same no matter whether the smaller end is closed or not. However, the isotherms for these pores are distinctly different: single hysteresis loop is observed for the open wedge compared to seven hysteresis loops for the closed-end wedge before the interface is developed, with the evaporation for the last two hysteresis loops occurring at the same pressures as those for the open wedge because these evaporations occur in the region that two wedge pores overlap geometrically. This indicates that the evaporation mechanisms are the same for both closed-end and

open wedges. Further supporting evidence of snapshot is shown in Appendix H.

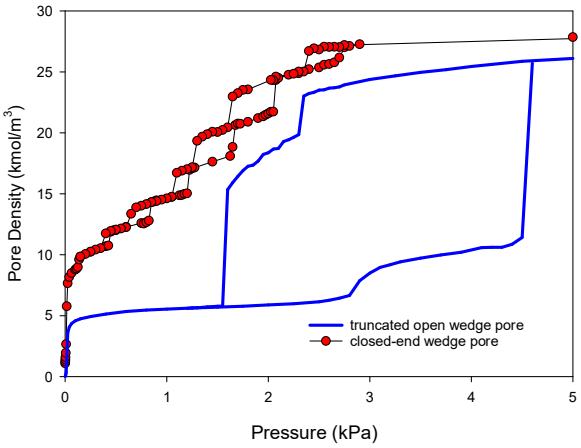

(a)

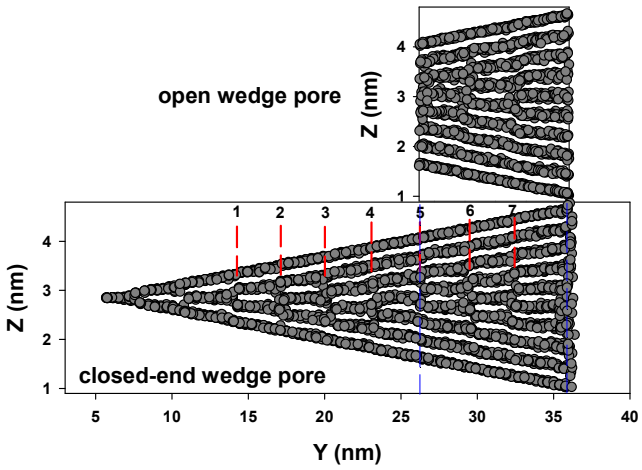

(b)

Figure 4.15 (a) The grand canonical isotherm (shown as blue solid line) for xenon adsorption at 134 K in an open graphitic wedge pore with its small end truncated at the position 5 of the closed end wedge whose L=32.8 nm and α= 3.5° (see Figure 4.12 for the truncation), and the grand canonical isotherm of this closed end wedge is also presented for comparison. (b) Snapshot of the molecular configuration at the bulk sublimation pressure for the open graphitic wedge (top panel), and the corresponding snapshot for the closed end graphitic wedge (bottom panel).

4.3.7 Hysteresis in Closed-end Wedge Pore and the Bifurcation Temperature

To determine the microscopic origin of the hysteresis in closed-end wedge pores, we studied the canonical and grand canonical isotherms for xenon adsorption at 134 K in a shorter closed-end graphitic wedge with L=20.6 nm and half angle of 3.5 degrees

(Figure 4.16).

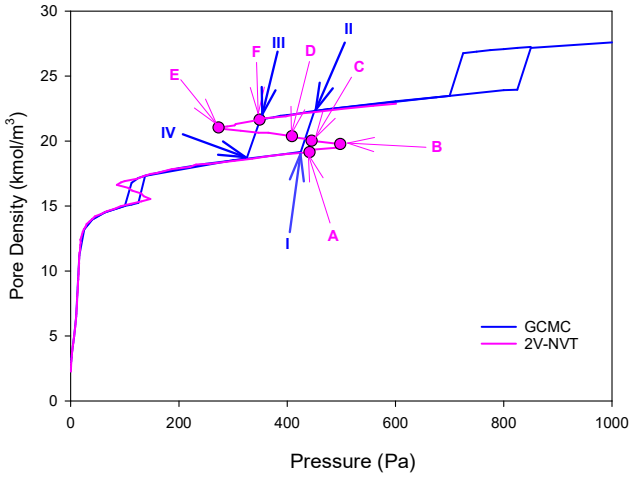

Figure 4.16 The grand canonical and canonical isotherms for xenon adsorption at 134 K in a closed end graphitic wedge with L=20.6 nm and α= 3.5 degrees. The circles on canonical isotherm denote the pressure points used for plotting the snapshots in Figure 4.19.

We took the second hysteresis loop as an example to study the first order transitions in the grand canonical isotherm and presented the snapshots of the molecular configuration for various points (*Points* I to II for condensation) and (*Points* III to IV for evaporation) in Figure 4.17.

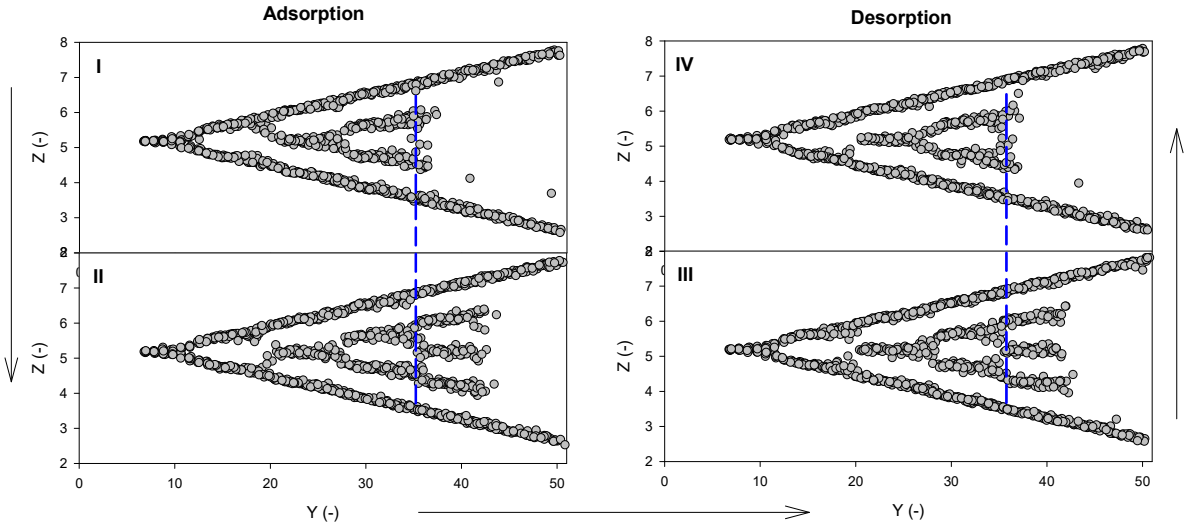

Figure 4.17 The snapshots of the molecular configurations for the condensation (*Points* I to II) and the evaporation (*Points* II to IV) marked on the grand canonical isotherm in Figure 4.16.

The first-order condensation (*Points* I to II) is associated with the formation of a new domain whose number of molecular layers is incremented by one from the previous

domain. This is called the bifurcation with the last domain composing of two layers at *Point* I bifurcating into three layers at *Point* II. This process is akin to the layering mechanism for adsorption on a flat surface at temperatures less than the 2D-critical temperature of a given layer. For wedges, we defined the bifurcation temperature, $T_{N,N+1}^{bifur}$, as the characteristic temperature at which the domain of N layers yields an additional domain of N+1 layers. For temperatures greater than $T_{N,N+1}^{bifur}$, there is no first-order transition of the bifurcation, although the pattern of alternate domains and junctions persists, as exemplified in the isotherm at 150 K in Figure 4.18.

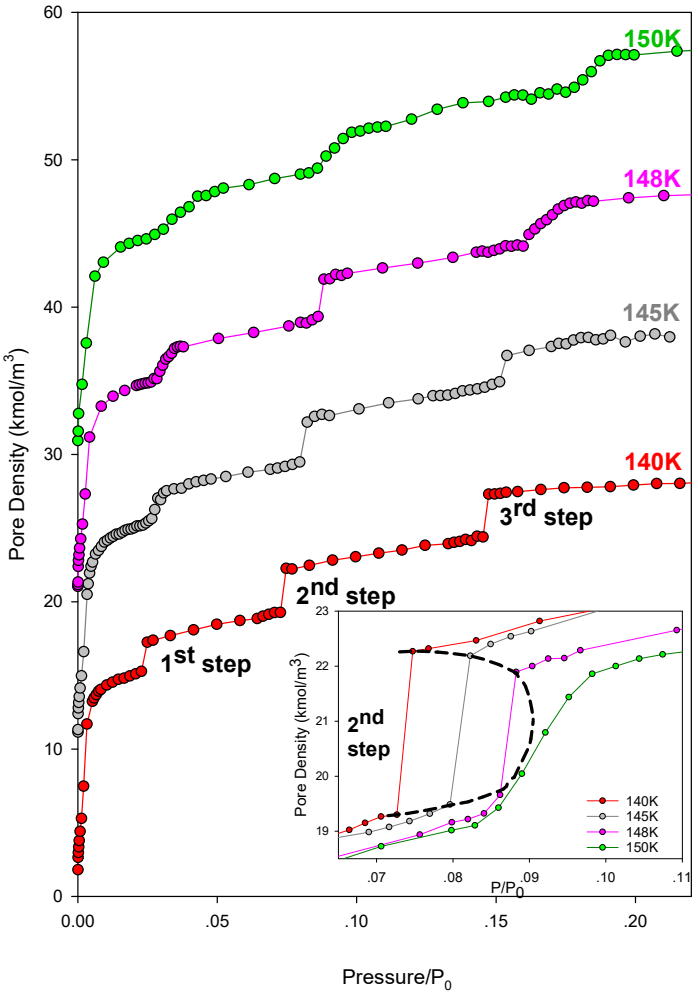

Figure 4.18 The grand canonical isotherms for xenon adsorption at 140 K, 145 K, 148 K and 150 K in a closed-end graphitic wedge with length L=20.6 nm and half angle α of 3.5 degrees. The isotherms are shifted by 10 kmol/m^3 for clarity, and the P_0 at different temperatures are the simulated sublimation pressures obtained from *VSE* simulation (Table G1 in Appendix G). The inset shows the second steps on these four isotherms.

The bifurcation temperatures are obtained from the isotherms in Figure 4.18 and summarized in Table 4.5, and for comparison we listed in the same table the 2D-critical temperatures of the first three adsorbate layers for xenon adsorption on planar graphite (details are given in Appendix I). Interestingly, the bifurcation temperatures for the wedge follow the same trend as for the 2D-critical temperatures for graphite, but they are greater, due to the enhancement in the solid-adsorbate interactions.

Table 4.5 The 2D critical temperatures for the first three adsorbate layers for xenon adsorption on a planar graphite (second column), and the characteristic temperatures for the first 3 steps in a closed-end graphitic wedge with length *L*=20.6 nm and half angle α of 3.5 degrees.

	Planar graphite	Closed-end wedge pore
1st step Critical T (K)	130	145
2nd step Critical T (K)	145	~150
3rd step Critical T (K)	140	148

The structure of the adsorbate for temperatures below the bulk triple point shows an alternate domains and junctions. In a recent work of Loi et al. [104] with argon adsorption in wedge the length of a domain is found to be a function of the wedge angle and is independent of temperature, $L_{domain} = 2^{1/6}\sigma_{ff} / \left(2\tan\alpha\right)$, where σ_{ff} is the collision diameter of the adsorbate and α is the wedge half angle, the same is also true for xenon studied in this work.

4.3.8 NVT vs. GCMC

To explore the microscopic mechanism of the hysteresis, we analysed the canonical and grand canonical isotherms for xenon adsorption at 134 K a closed-end graphitic wedge with *L*=20.6 nm and half angle of 3.5 degrees, as presented in Figure 4.16. As expected, these isotherms overlap where the isotherm is reversible, except in the regions where hysteresis occurs. In these regions the canonical isotherm exhibits van der Waals (*vdW)* loop which envelops the first-order condensation and evaporation of the grand canonical isotherm, with these transitions occurring before the corresponding spinodal points have been reached because of the thermal fluctuations.

To understand the microscopic mechanism of the hysteresis, we presented in Figure 4.19 the snapshots of the molecular configurations for various points spanning the second *vdW* loop (taken as an example) of the canonical isotherm. *Point A* is just before the first order condensation, occurring before the gas-like spinodal point of *Point B*. As the pressure is increased from *Point A* to *Point B*, we observed the formation of clusters of molecules at the end of the layers which merge to form a stable nucleation site at *Point* C, from which bifurcation occurs with the formation of a new domain. As have pointed out by Tan et al. [194] the coalescence is accounted for the sharp decrease of the pressure, because the radius of the fused cluster is greater than the radii of the two clusters before merging. Further dosing induces the bifurcation at *Point* D and a complete domain is formed at the liquid-like spinodal point of *Point* E, beyond which the domain is densified up to *Point* F. The same process is repeated for the third and higher hysteresis loops.

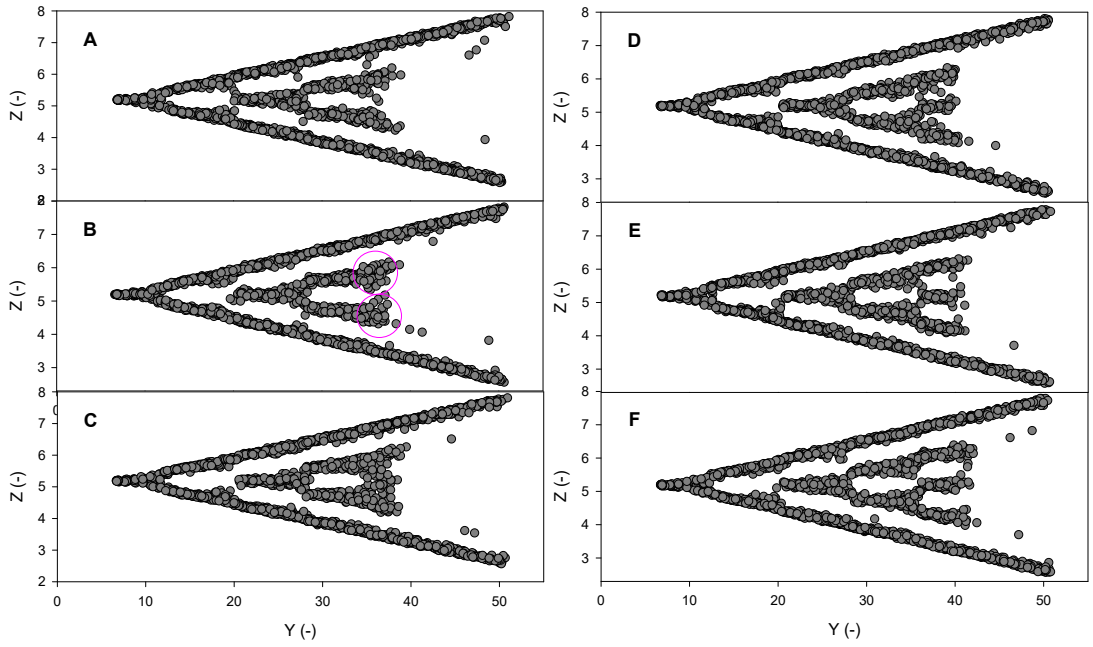

Figure 4.19 The snapshots of molecular configurations for various points as marked on the canonical isotherm in Figure 4.16.

Similar behaviour is observed for different half angles, and we showed one example of 4.2 degrees half angle in Figure J1 (Appendix J). Apart from the above observations, each domain has its own critical half angle above which the adsorbate of that domain

becomes disordered (Appendix K).

4.4 Conclusions

Adsorption of xenon in open wedge pores and its step-wise desorption behaviour under subcritical conditions were thoroughly investigated using GCMC simulation. We have found that there exists a bifurcation temperature for the occurrence of the step-wise desorption. Low temperature facilitates the formation of orderly structures in the wedge in the form of domains of commensurate packing, separated by small junctions of incommensurate packing, the former of which results in steps in the desorption boundary of the hysteresis loop. The length of the domain depends only on the angle of wedge and is independent of the temperature for temperatures less than the bifurcation temperature, which was found to be about the boiling temperature of xenon. The pore widths of the junctions, i.e. the transition region between the two adjacent domains accommodating N and $N+1$ integer adsorbate layers, are not affected by the pore angle, length and temperature.

Hysteresis was then proved to exist in closed-end wedge pores for temperatures below the bulk triple point temperature. The functional form of the Cohan equation is found to be valid in relating the radius of curvature of the interface to the bulk pressure. The hysteresis was observed when the adsorbate forms alternate domains and junctions, with integral number of adsorbate layers in each domain. To form a domain, which is the source of the hysteresis, the temperature is lower than the bifurcation temperature for that specific domain, and this bifurcation temperature is a function of the wedge angle. Each domain has its own characteristic temperature above which it becomes disordered. The microscopic mechanism of the hysteresis was investigated with the simulation in the canonical ensemble, through which we can track the growth the domain and the formation of junctions as a function of loading. The alternate evaporation of domains and junctions is the microscopic reason for the stepwise evaporation which is the same as that in open wedge. The external adsorbent field and the confinement of the closed-end wedge pore have a significant effect on the

condensed phase at temperatures below the triple point, under which the adsorbate is not as dense as the bulk solid, but is denser than the supercool liquid.

Chapter 5. Adsorption-Induced Deformation in Connected Deformable Pores

5.1 Introduction

Adsorption induced deformation has been a well recognized phenomenon, the deformable solids show expansion/contraction or more complex behaviors which could have influence on the adsorption capacity and heat, and moreover, a source of hysteresis. Gor et al. [195] proposed that due to the high sensitivity of the microporous solids to the adsorption-induced deformation, the measurement of adsorption-induced strains could be an efficient way for characterizing the microporous solids. Although various experimental results are well-documented, the fundamental understanding of adsorption-induced deformation has not been fully resolved. Theoretical studies demonstrated that deformation is a complex function of pore size, pore shape, temperature, pressure, adsorbate species, and the properties of the adsorbent, etc. However, most of these studies focus on either micro- or meso- uniform pore model. Until very recently, theoretical attention has turned to non-uniform pore model, such as wedge pore [196], but remained the focus on micro- size range.

It should be noted that most experimental investigations have been carried out in complex solids which contain both micropores and mesopores. Therefore, it is questionable that the deformation mechanisms in pores of either micro- or meso- sizes are applicable in real cases. To the best of our knowledge, little attention has turned to the theoretical studies of deformation in a connected pore having both micro- and meso- size components. In this chapter, we proposed a more realistic solid model consisting of both micro- and meso parts, and utilize *MC* simulation to systematically investigate how each part influences the deformation behaviors of the connected pore as a whole. In the meantime, we paied special attention to the hysteresis observed in the deformable connected pore model. We would like to stress the effect of bulk

modulus (how easy or difficult for pore to deform) on the hysteresis. Hysteresis is possible to occur when the bulk modulus is lower than a critical value as the pore is easier to deform to some specific size. Bulk modulus is found to be a function of the number of movable layers and solid affinity.

5.2 Simulation Details

GCMC Simulation

In a *GCMC* simulation we used at least 2×10^5 cycles in both the equilibration and sampling stages. Each cycle consists of 1000 trial moves of displacement, insertion, deletion of argon molecules, and displacement of the flexible graphene layers, chosen with the following ratio of probabilities: 333:333:333:1, giving a total of 2×10^8 configurations per calculated pressure point. In the equilibration stage, the maximum displacement length in each direction is initially set as half of the dimension of the box in that direction, and is adjusted at the end of each cycle to give an acceptance ratio of 20%, and then is kept constant during the sampling stage. For the displacement of a movable layer, one layer is chosen randomly and displaced in the direction normal to the pore walls, with acceptance following the usual Metropolis rule. The maximum displacement length for a movable layer is kept as 1/1000 of the separation distance between adjacent layers in both the equilibration and sampling stages. The cut-off radius is 5 times the collision diameter of argon.

The schematic plot of the pore model is presented in Figure 2.6. We have studied four different combinations of the narrow and wide (initial) pore sizes as shown in Table 5.1, falling into micro- and meso- range respectively. Each case includes three different narrow pore length L_N = 1/4 L, 1/2 L and 3/4 L.

Table 5.1 Four different combinations of the narrow and wide pore sizes.

	Narrow Pore Size H_N (nm)	Wide Pore Size H_W (nm)
Case 1	0.65	2.01
Case 2	0.80	2.15
Case 3	0.90	2.25

Case 4	0.99	2.34

The deformation modes for slit micropores are divided into four categories: expansion at all loadings, contraction at all loadings, initial contraction followed by expansion, keeping commensurate at all loadings. These modes are mapped by the pore size in Figure 5.1, according to which, the deformation modes for the sizes corresponding to the narrow parts for Case 1-4 are expansion, contraction, contraction followed by expansion and commensurate, respectively.

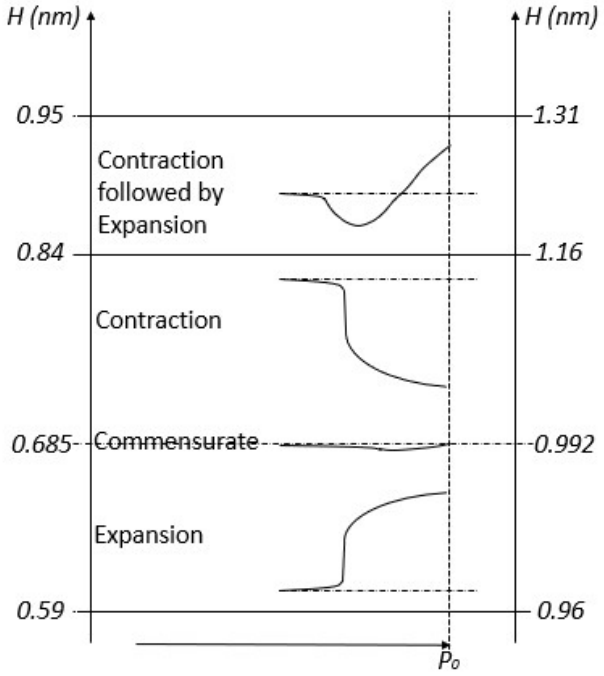

Figure 5.1 Four deformation modes for deformable slit micropores over the size range of 0.59-1.31 nm.

Deformable Independent Slit Pore (Slit Unit)

Here for the sake of comparison, we also define the deformable independent slit pores, named slit unit hereafter, those having the same initial size as the narrow section are composed of 4 movable layers and 1 fixed layer in each wall while those having the same initial size as the wide section consists of 2 movable layers and 1 fixed layer in each wall. The pore lengths of the micro- and meso- slit units are 10 nm and 20 nm, respectively.

5.3 Results and Discussions

5.3.1 Effects of Pore Size

First, we fix the length of the narrow pore L_N as half of the total pore length L, and only change the pore sizes. We show in Figure 5.2 the strain isotherms of both narrow and wide sections for all four cases at 87.3 K, the results of the corresponding slit units that having the same initial sizes are presented in the same figures for comparison.

For all the four cases studied here, regardless of pore sizes, the strain isotherms of wide pores resemble very much that of narrow ones, however, with the magnitude about one order smaller, and start to divert from the narrow pore when approaching the saturation vapour pressure. From Figure 5.2, four deformation modes can be classified: expansion at all loadings (Case 1), contraction at all loadings (Case 2), contraction followed by expansion (Case 3) and commensurate pores (Case 4).

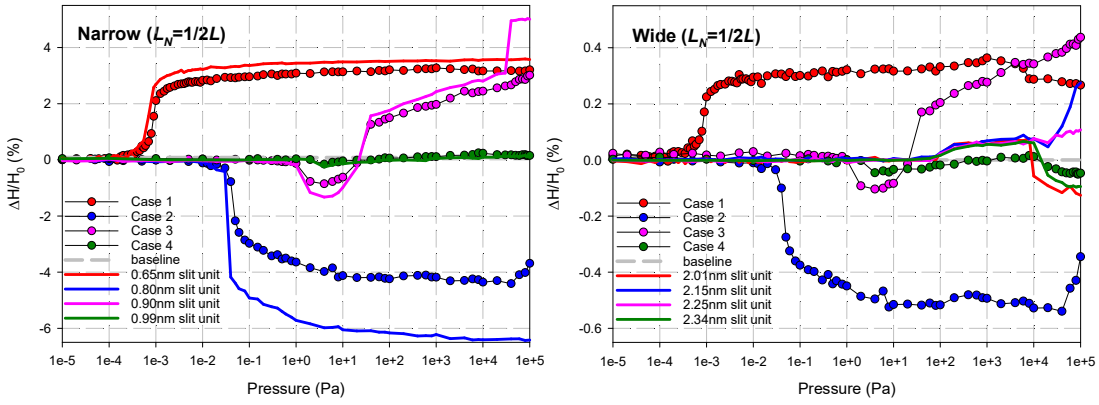

(a) (b)

Figure 5.2 The strain isotherms of (a) narrow pore and (b) wide pore for four cases at 87.3 K. The strain isotherms of corresponding deformable independent slit pores (slit units) with the same initial widths are presented for comparison.

The comparison with the strain isotherms of corresponding slit units suggests that the micro- narrow pore determines the general major shape of the strain isotherm while the meso- wide pore comes into effect the behaviour at high pressure, due to the stronger *SF* interaction in micro- narrow pore.

There is some obvious mutual influence of the two parts in the connected pore that the existence of meso- wide pore results in a smaller contraction/expansion extent of the

micro- narrow pore compared with the corresponding micro- slit units. Conversely, the existence of micro- narrow pore results in a larger variation extent of wide pore compared with the corresponding meso- slit units.

Interestingly, there is a sharp increase in the strain isotherm of 0.90 nm deformable slit unit pore at pressure of 5×10^4 Pa, which is associated with hysteresis and will be addressed in more details in Section 5.3.2.2.

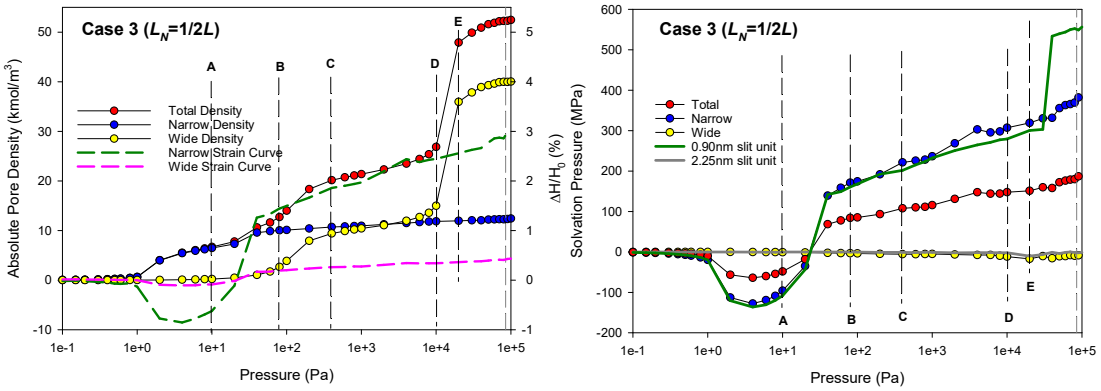

(a) (b)

Figure 5.3 (a) Pore density and (b) solvation pressure versus loading for Case 3, divided into two parts: narrow pore and wide pore. The solvation pressure versus loading of corresponding slit unit pores are presented for comparison.

In order to shed a light upon the underneath mechanism, next we take Case 3, which has the most complicated deformation pattern among all four cases, as an example for microscopic analysis. Figure 5.3 shows the narrow pore, wide pore and total pore density and solvation pressure versus loading. Comparison of isosteric heat of Case 3 and that of corresponding slit unit pores is shown in Figure 5.4. The snapshots for points A-E as labelled in Figure 5.3 are presented in Figure 5.5. From these figures, we can make the following observations:

a) With pressure increase up to point A, adsorption initiated from the small pore inside which two complete contact adsorbed layers are formed due to greater *SF* interaction than the wide section. At this stage, the connected pore acts as an independent 0.90 nm deformable slit pore, contraction occurs due to the negative

solvation pressure in the narrow pore. A very slight increase in *SF* energy at 1.8 Pa (Figure 5.4a) is because of the formation of the two contact layers, which induces the contraction of the pore and the distance between the contact layer and solid is reduced to maximise the system energy. As shown in Figure 5.4b, with pressure increased from 1 Pa to 1.8 Pa, the contact layers are pushed closer to the solid walls while approaching the well-depth of the *SF* potential.

b) From point A to B, more particles squeeze into the two contact adsorbed layers in the micro- narrow pore while start to adsorb in the meso- wide pore. Accompanying this increased adsorption is the transition of the connected pore from contraction to expansion, as governed by the narrow pore. Additionally, due to the average distance between the particles is increased, the *FF* energy in the connected pore is weaken. Expansion in pore size results in a weaker *SF* energy, as shown in Figure 5.4c.

c) From point B to C, the completion of contact layers (multilayer region) in the wide pore induces further expansion as reported by Diao et al. [146], accounts for the second hump in *FF* energy and total energy, while the *SF* energy decreased slightly as particles start to adsorb into the higher layers in the wide pore and getting further from the walls.

d) From point C to D, particles mainly build up at the junction of the pore and form a concave meniscus, *FF* interaction remain constant while *SF* decreased, due the larger distance between adsorbate and solid. The monotonically increased solvation pressure in the narrow pore is accounted for the pore expansion.

e) From point D to E, capillary condensation occurs in the wide pore, which exhibits as a very small negative solvation pressure (Figure 5.3b), however, this is compensated by the increase of positive solvation pressure as in the narrow pore, and thus the total solvation pressure remains constant.

f) From point E to the saturation vapour pressure, particles fill in the meniscus, the pore is expanded further because of expansion in both the narrow and wide pores.

From the above microscopic analysis, we confirm that the deformation behaviour of a

connected pore is dependent on both the narrow and wide pores, with the narrow section being more dominating especially at the low pressure region.

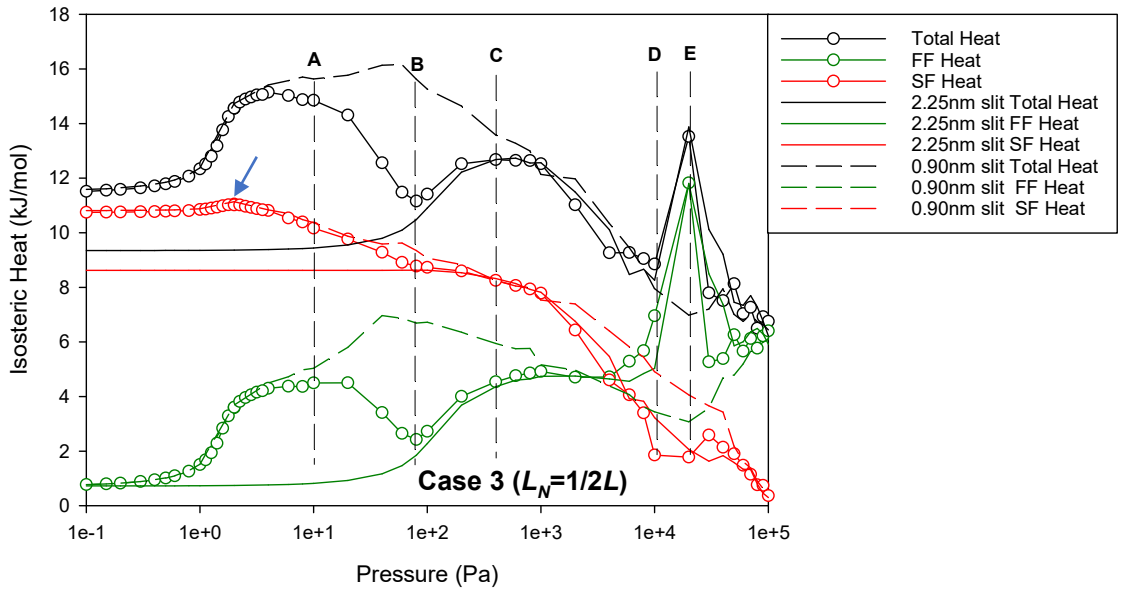

(a)

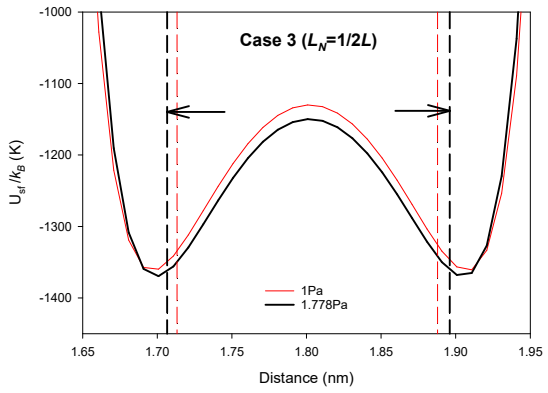

(b)

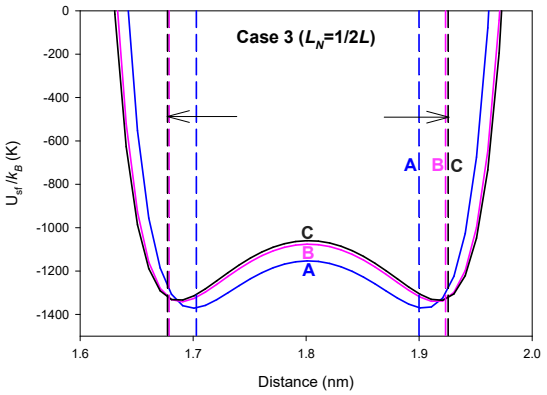

(c)

Figure 5.4 (a) Comparison of isosteric heat of Case 3 and that of corresponding slit units with same initial widths of 0.9 nm and 2.251 nm. (b) The U_{sf} profiles at 1 and 1.8 Pa; (c) the U_{sf} profiles at pressures corresponding to points A-C; the dashed line represents the positions of the contact layers in the narrow pore in the z-direction (parallel to the pore walls).

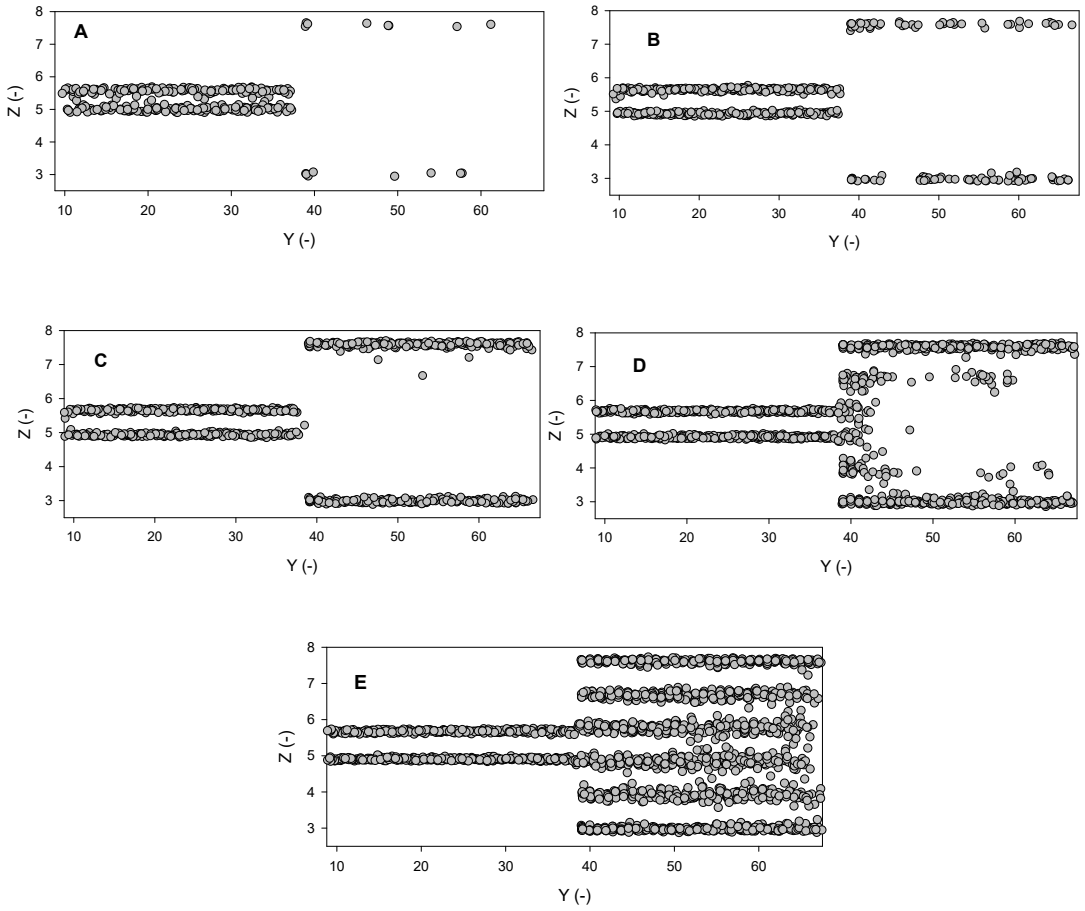

Figure 5.5 Snapshots for points A-E as labelled in Fig. 5.3 for case 3.

5.3.2 Effects of Length Ratio

5.3.2.1 Extensive strain isotherms of connected pores with different length ratios

In Figure 5.6, we presented the strain isotherms of both narrow and wide pores of different length ratios for Case 1-4. From the extensive study, we can see that by increasing the length of narrow pore, its deformation behaviours approach that of the independent slit unit pores, and the same applies to the wide pore.

The most distinct difference lies in the deformation behaviours of the wide pore, which are significantly affected by the presence of the connected narrow pore. Compare with the strain isotherms of the corresponding deformable unit slit pores, at the final status of the saturated wide pore, it changes from contraction to expansion (Case 1), from expansion to contraction (Case 2), ended with enhanced expansion (Case 3) and from slight contraction to being commensurate (Case 4), and the deviation is enhanced with

the increased narrow pore length $L_{N,}$ i.e. shorter length of the wide pore. Moreover, with different length ratios, the final status of the two parts could be completely different, e.g. when L_N = 1/4 L in Case 2, the narrow pore contracts while wide pore is commensurate at saturation vapour pressure.

Another interesting phenomenon was observed in Case 4, with the 0.99 nm narrow pore being a commensurate pore, all strain isotherms of the wide pore merge to the same commensurate point at saturation pressure, though the length ratios are different.

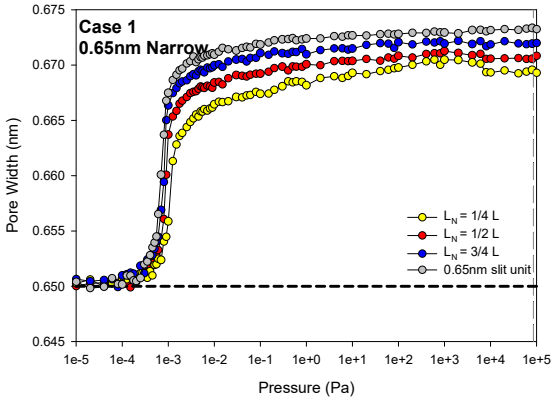

(a)

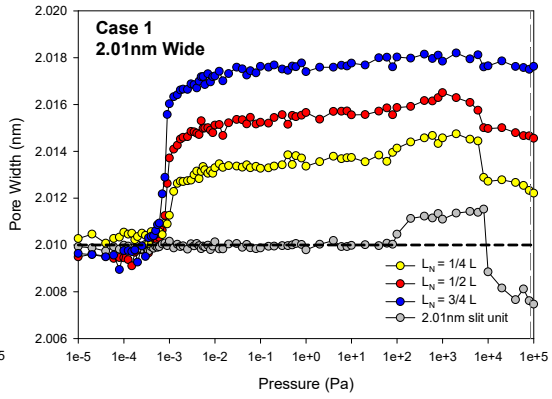

(b)

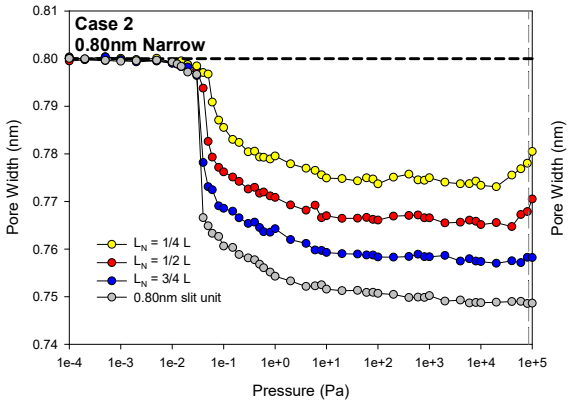

(c)

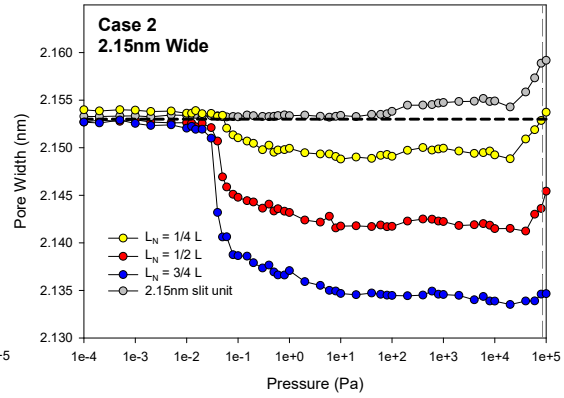

(d)

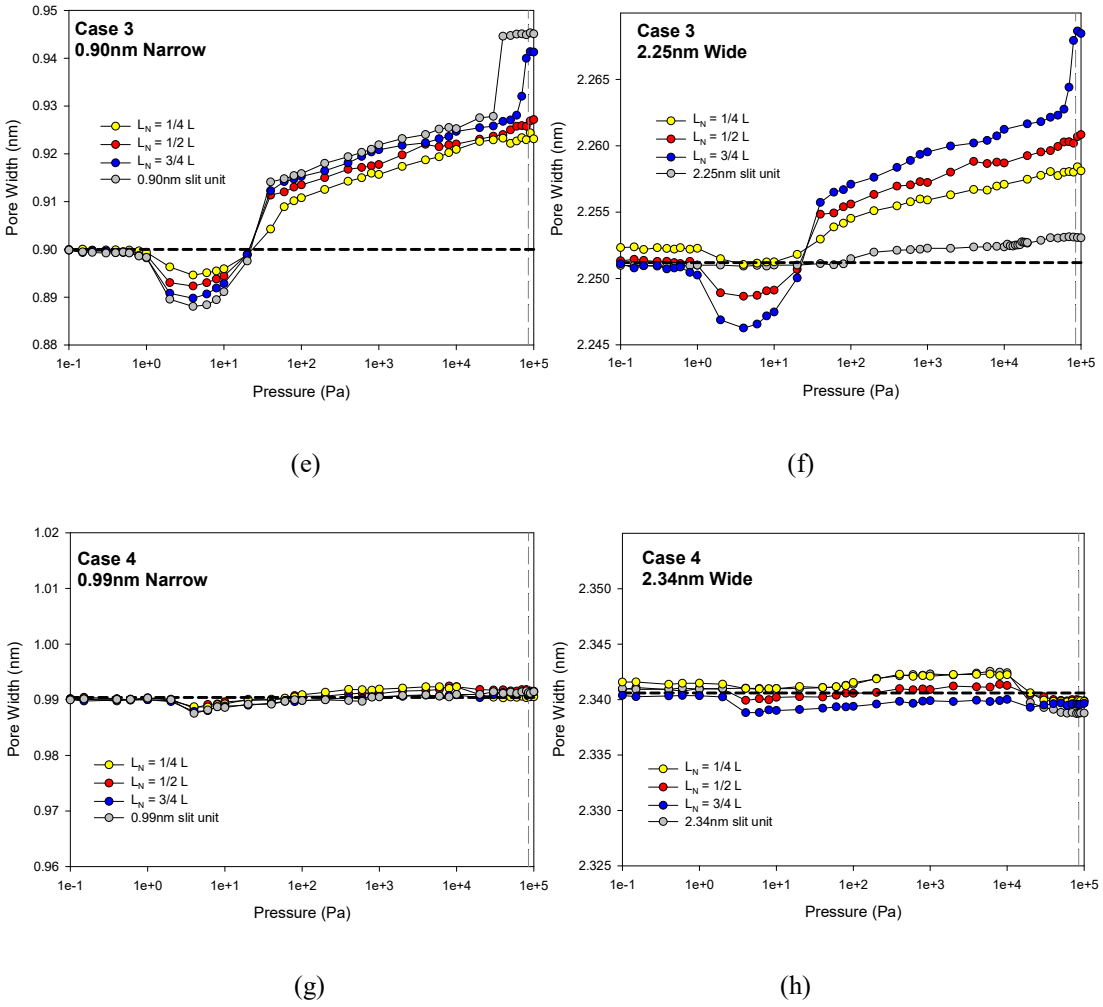

Figure 5.6 The strain isotherms of the narrow pore for 4 cases are presented in (a) (c) (e) and (g) with the strain isotherms of wide pore are in (b) (d) (f) and (h). The strain isotherms of corresponding deformable slit unit pores with same initial widths are presented for comparison.

5.3.2.2 Hysteresis in Case 3

Another interesting feature is the formation of hysteresis in Case 3 (Figure 5.7). When narrow pore length L_N is increased to 3/4 L, hysteresis occurs in both the narrow and wide pores. Through the comparison with the strain isotherms of corresponding deformable unit slit pores, we found that 0.90 nm deformable slit unit also has hysteresis. This indicates that the narrow pore has a strong influence on the wide pore and the narrow pore length ratio needs to be increased to a certain critical value to trigger the occurrence of hysteresis.

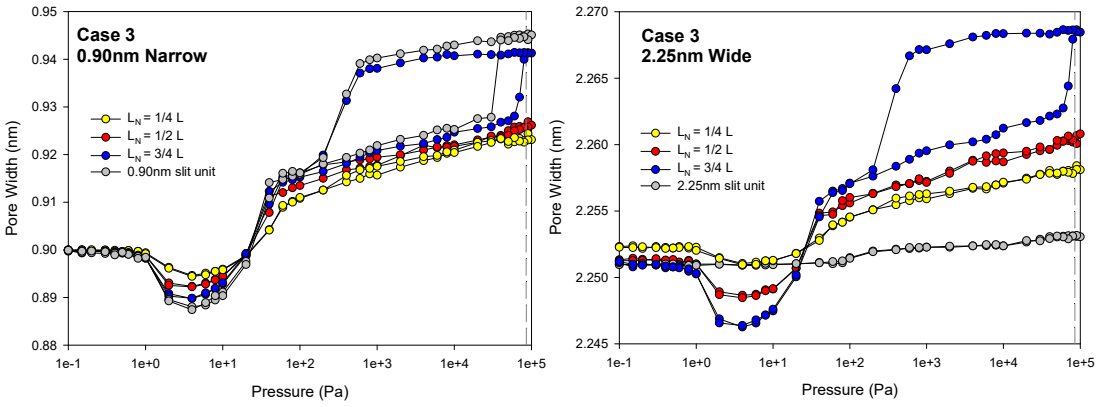

(a) (b)

Figure 5.7 The strain isotherms of (a) narrow pore and (b) wide pore for Case 3. The strain isotherms of corresponding deformable slit pores with same initial widths are presented for comparison.

To further explore this hysteresis, the effects of the number of movable layers were investigated for the 0.90 nm deformable slit unit, the strain isotherms are shown in Figure 5.8a. Hysteresis occurs only when each wall consists of at least four movable layers. This is also manifested in the density isotherms (Figure 5.8b), the ones with at least four movable layers have greater capacity due to a further expansion of the pore to accommodate more particles. As reported by Diao et al. [146], the increase of the number of movable layers results in the decrease of bulk modulus and makes the pore easier to deform. The percentage change of the pore width versus solvation pressure (Figure 5.8c) clearly demonstrates this declining trend of bulk modulus from 22 GPa to 8 GPa (Figure 5.8d). Obviously, low bulk modulus can facilitate the formation of the hysteresis. Figure 5.9 shows the snapshots of the bottom contact layer (in the deformable slit pore with 4 movable layers) for point A and B as labelled in Figure 5.8a, and we see a distinct change in the packing pattern, that is, more stable hexagonal structures are visible at point B. This gives rise to stronger *FF* interaction, and it is compensated by the decrease of *SF* energy and *SS* energy (being less negative) as illustrated in Figure 5.10, which is possible due to the further expansion of the pore. Similar transition and packing change of particles are also found in the deformable slit pore with 5 movable layers. Moreover, hexagonal structure is also observed in rigid slit pore with the same size as point B, indicating that the packing change of adsorbate

in deformable pore is because the pore size deforms to the specific value of 0.9446 nm.

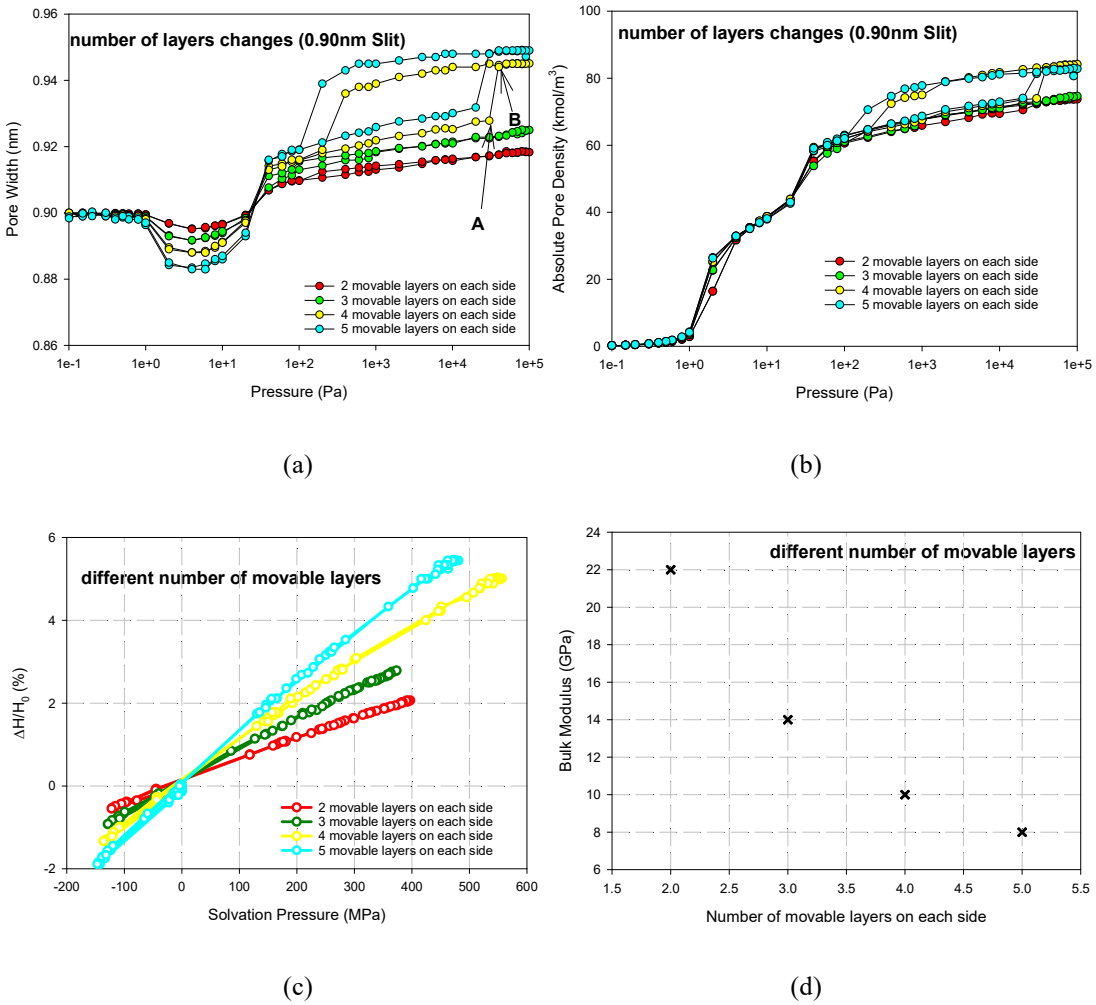

Figure 5.8 The (a) strain, (b) density isotherms, (c) percentage change of the pore width versus solvation pressure and (d) bulk modulus of 0.9 nm deformable slit pores with different number of movable layers.

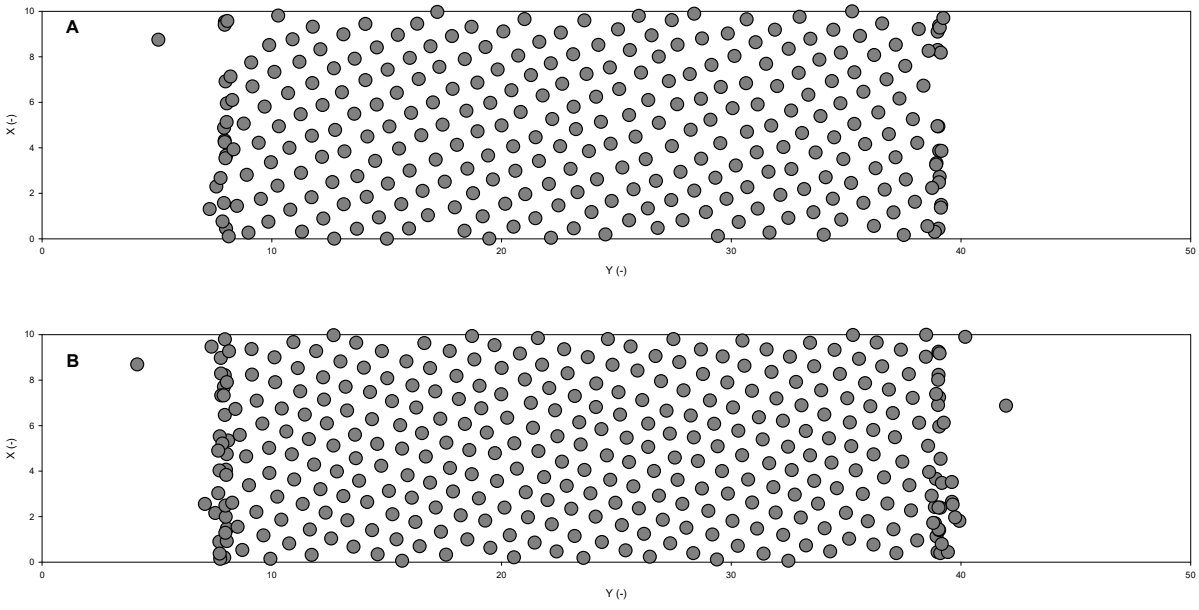

Figure 5.9 The snapshots of the bottom contact layer for point A and B as labelled in Figure 5.8a.

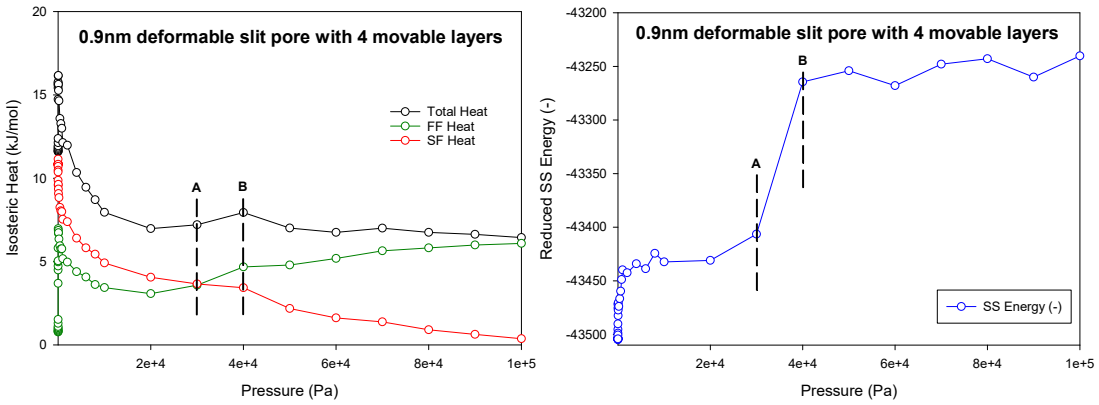

(a) (b)

Figure 5.10 (a) Isosteric heat and (b) reduced *SS* energy of 0.9 nm deformable slit pore with 4 movable layers and 1 fixed layer in each wall.

The bulk modulus of the narrow section in the deformable connected pore for Case 3 slightly decreases with its length (Appendix L), contrary to what was reported by Diao et al. that the bulk modulus of the deformable slit pore slightly increases with slit length. This also indicates the mutual influence of wide section on narrow section.

From the above analysis, we concluded that the hysteresis in the connected pore is presented only when the length of the micro- narrow section exceeds half of the total length, and again the deformation of the connected pore is dominated by the deformable micro- narrow section. The hysteresis is due to the packing change of particles when the pore size is expanded to a specific value and this expansion is only possible when the bulk modulus is below certain value.

5.3.3 Effects of Temperature

The effects of temperature were studied with the Case 3 pore configurations at 298 K with pressure up to 10^8 Pa. The strain isotherms of narrow and wide pores together with that of the corresponding deformable unit slits are shown in Figure 5.11. At this supercritical condition, a much smaller extent of contraction is observed, without hysteresis, emphasizing the importance of higher thermal motions and fluctuations of the molecules in swelling.

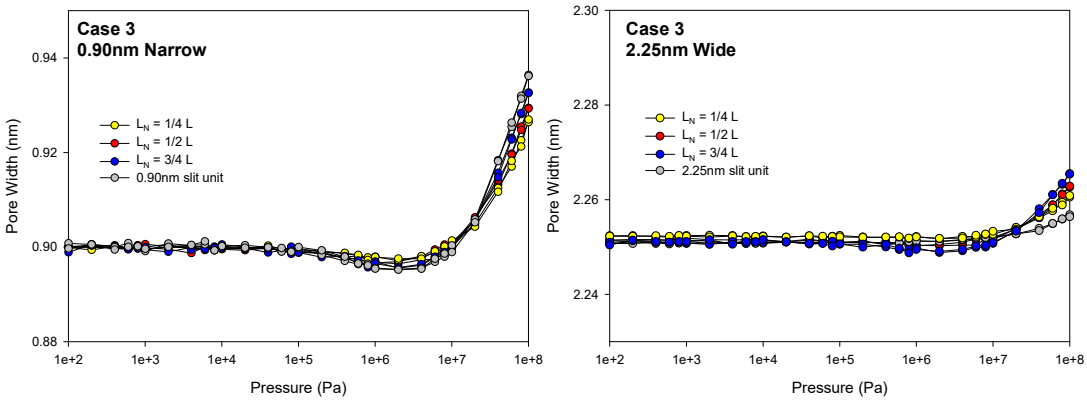

(a) (b)

Figure 5.11 The strain isotherms of (a) narrow pore and (b) wide pore for Case 3 at supercritical temperature 298K. The strain isotherms of corresponding deformable slit units are presented for comparison.

5.3.4 Effects of Surface Affinity of Narrow Section

As illustrated in earlier sections, the narrow pore plays a dominant role in determining the deformation mode of the entire connected pore. To reinforce this proposal, we decreased the reduced well depth of carbon atom from 28 K to 15 K in the innermost 4 movable layers of the narrow section to reduce its modulus, i.e. easier to deform. Pore configurations in Case 3 are used, as expected in Figure 5.12, the hysteresis not only exists in the pore with 3/4*L* narrow section length but also in those with shorter narrow section lengths. Figure 5.13 presents the comparison of percentage change of the pore width versus solvation pressure in the two corresponding 0.90 nm deformable slit unit pores with different solid affinity, indicating that the modulus decreases from 10 GPa to 5.4 GPa.

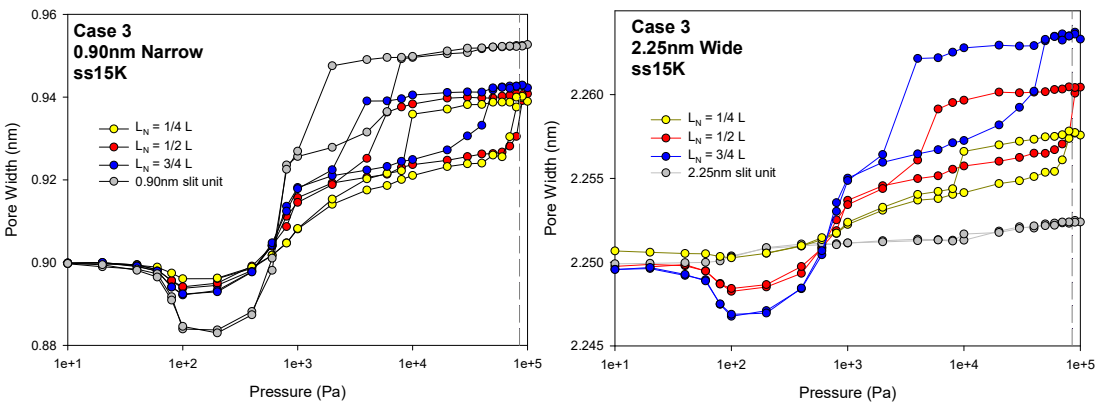

(a) (b)

Figure 5.12 The strain isotherms of (a) narrow pore and (b) wide pore for Case 3 when the reduced well depth of solid decreased to 15 K. The strain isotherms of corresponding deformable slit unit pores are presented for comparison.

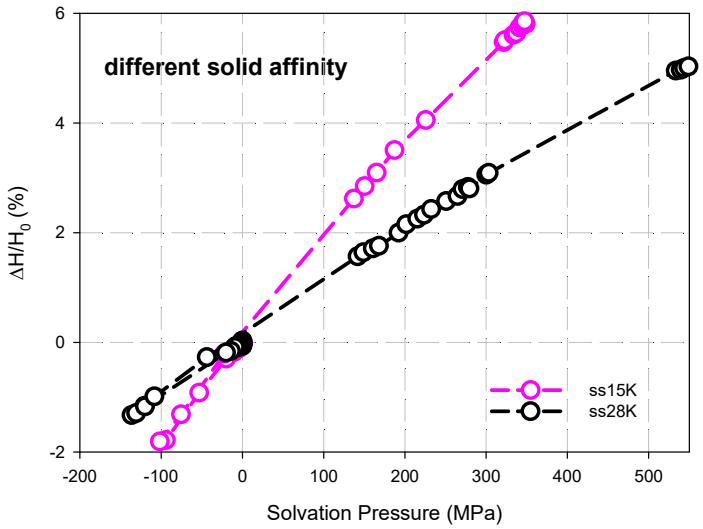

Figure 5.13 Comparison of the percentage change of the pore width versus solvation pressure in two corresponding 0.9 nm deformable slit unit pores with different solid affinity.

5.4 Conclusions

A systematic investigation has been carried out for the adsorption-induced solid deformation in our newly proposed connected deformable pore which is composed of micro- and meso- size parts. We observed mutual influence between the two parts and the deformation of the connected pore depends on both parts. Specifically, the micro- narrow section is more dominating (especially at low pressure) and determines the general major shape of the strain isotherm, while the meso- wide section comes into effect at high pressure, due to the stronger SF interaction in micro- narrow section. The increasing length ratio of micro- narrow section can further strengthen its dominating role. Moreover, a very interesting observation is that hysteresis can exist in connected deformable pore under critical temperature only when the length ratio of micro- narrow section exceeds half of the total length. This hysteresis is due to the packing change of particles when the pore size is expanded to a specific value. This was further investigated by checking on the bulk modulus, and found that hysteresis is only

possible when bulk modulus is lower than a critical value, which can be achieved by increasing the number of movable layers and decreasing the solid affinity.

Chapter 6. Adsorption of Mercury with Activated Carbon: A Practical Application

6.1 Introduction

The removal of mercury with carbonaceous materials has attracted global attention because of the harmful effects of mercury on human and the environment [197, 198], to further improve the removal technology, there is a need to understand the interaction between mercury and carbon [199, 200]. To date, this has been limited to first-principle calculations of mercury interaction with small clusters of carbon atoms, which is not suitable for studying adsorption of mercury in porous carbons where the high surface density and the confined space play a very significant role.

In this chapter, the new potential model for mercury developed in Chapter 3 was applied to simulate mercury adsorption in activated carbon (AC). It is well recognized that mercury cannot wet AC under ambient conditions [201] without functional groups, such as halogens and sulphur [198-200]. Wetting of mercury in carbon nanotubes can only occur with the presence of electrocapillary pressure, known as electrowetting [202]. These findings indicate that mercury does not wet carbon because of the weak interaction between mercury and carbon, compared to the intermolecular interaction of mercury. In ultrafine graphitic pores, the solid-fluid interaction is enhanced, and we aimed to investigate to see whether such enhancement is sufficient to induce the filling of mercury in carbon pores. AC is known to have a very broad pore size distribution, ranging from ultrafine pores to large mesopores, and since the filling of mercury is only possible with ultrafine pores this explains the experimental fact that the volume of the adsorbed mercury is much less than the total pore volume. This will be substantiated with the extensive simulation study in this chapter, and we also explored systematically the effects of temperature and pore size on mercury filling. As far as the authors are aware of, this work is the first to study filling of mercury in ultrafine

carbonaceous pores with Monte Carlo simulation, although Tang et al. has recently just reported their work of mercury adsorption in MOF [55].

6.2 Simulation Details

GCMC Simulation

Adsorption of mercury in *AC* was investigated with *GCMC* simulation. The solid-fluid interaction energy is calculated with the Bojan–Steele equation (Section 2.3.1) [26, 162]. The *x*-dimension of the pore is 3nm, and the pore length (*L*) is 10 nm, and the periodic boundary conditions were only applied in the *x*- direction to simulate the infinite extent. Two bulk gas reservoirs of 3nm length in the *y*- direction are connected at each end of the pore, and periodic boundary conditions were applied in all directions, for example if a molecule is moved out of the gas space on the right it will be replaced by a molecule entering the left gas space. In a simulation 200,000 cycles were used in both the equilibration and sampling stages.

2V-NVT Simulation

The *2V-NVT* scheme is employed to obtain corresponding canonical isotherms [152, 203-205], comprising two boxes: one is the adsorption system and the other a gas reservoir. The dimensions of the pore are the same as that used in the *GCMC* simulations. For the gas reservoir box, the linear box dimension in *z*- direction is 2×10^6 nm which is large enough to ensure the reliable calculation of the bulk pressure, and the other two (*x*- and *y*-) dimensions are the same as those of the adsorption box. At least 100,000 cycles are used in both the equilibration and sampling stages. Each cycle consists of 1000 trial moves of two types with equal probability. Beside displacement is one of the trial moves for both boxes, molecule is allowed to move from one box to the other. The dosing increment of molecules is 2 each time before point E in Figure 6.3, and increases to 10 afterwards. The pressure of the gas reservoir is determined with the virial equation.

6.3 Results and Discussions

6.3.1 GCMC Simulations in Finite Open Slit Pores

Mercury adsorption in graphitic finite slit pores with the new 12-6 *LJ* (T) model were carried out with *GCMC* simulation. The intermolecular interactions of mercury are very strong such that it prefers to form clusters, in preference to adsorption on a graphite surface under ambient conditions (Appendix M). It is only when the temperature is high enough that adsorption on graphite can occur because of the entropic factor, and it was found that the wetting temperature of mercury on graphite is 1600 K, which is too high to be practical. We now investigate to see whether the enhancement of the solid-fluid potential energy in small slit pores is sufficient for the clusters to nucleate and coalesce, followed by filling of the pore space because of the strong intermolecular interactions. The isotherms of pore widths of 0.63 nm, 0.7 nm, 1nm and 2nm are presented in Figure 6.1 for a range of temperatures from 323 K (ambient condition) to 1500 K (very close to the critical point).

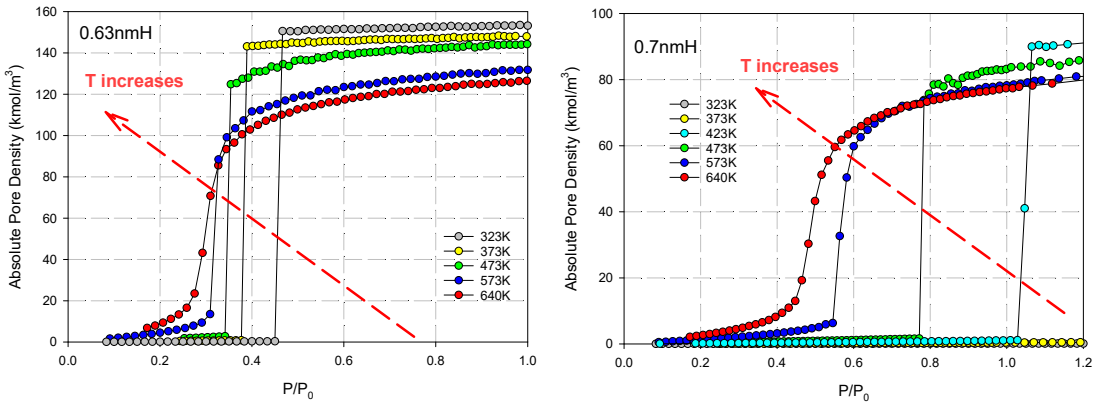

(a) (b)

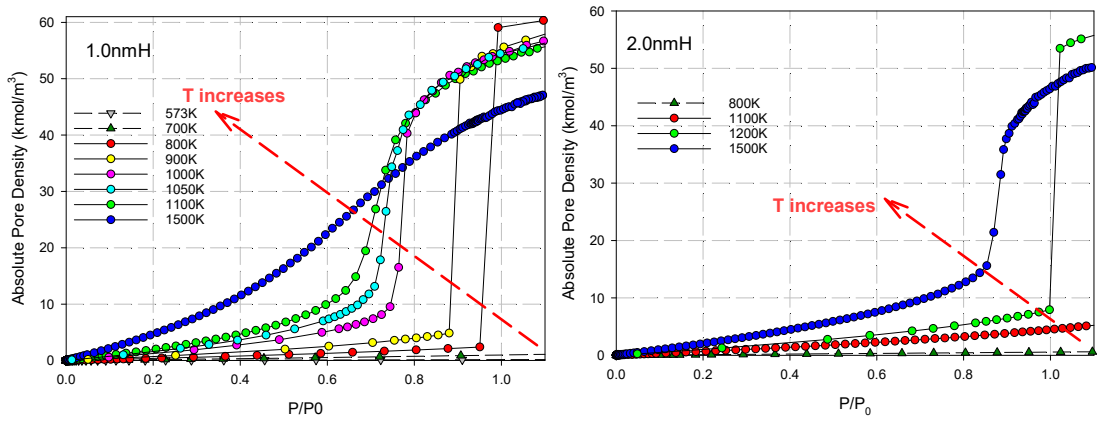

(c) (d)

Figure 6.1 Isotherms of mercury adsorption at various temperatures in slit pores having widths of (a) 0.63 nm, (b) 0.7 nm, (c) 1.0 nm and (d) 2.0 nm

For all pores considered the adsorbed amount increases with temperature for a given reduced pressure. This is due to the lower isosteric heat at zero loading than the heat of condensation (Figure 6.2a), a signature of non-wetting. Let us consider the isotherms of the 2 nm pore (Figure 6.1d), the non-wetting behaviour is observed for a wide range of temperatures because its solid-fluid potential is not sufficiently enhanced to induce the nucleation of clusters, and it is not until the temperature is high enough, 1200 K, above which filling occurs because of the entropic factor. On the other hand, in the ultrafine pore of 0.63 nm (Figure 6.1a), an interesting behaviour of non-wetting can be seen at very low loadings for all temperatures because the isosteric heat is less than the heat of condensation, but as the reduced pressure has reached 0.4, the enhancement of the solid-fluid interactions induce the formation of clusters, followed by filling even under ambient conditions. It is important to stress that filling of a pore with mercury does not mean that it wets the carbon surface.

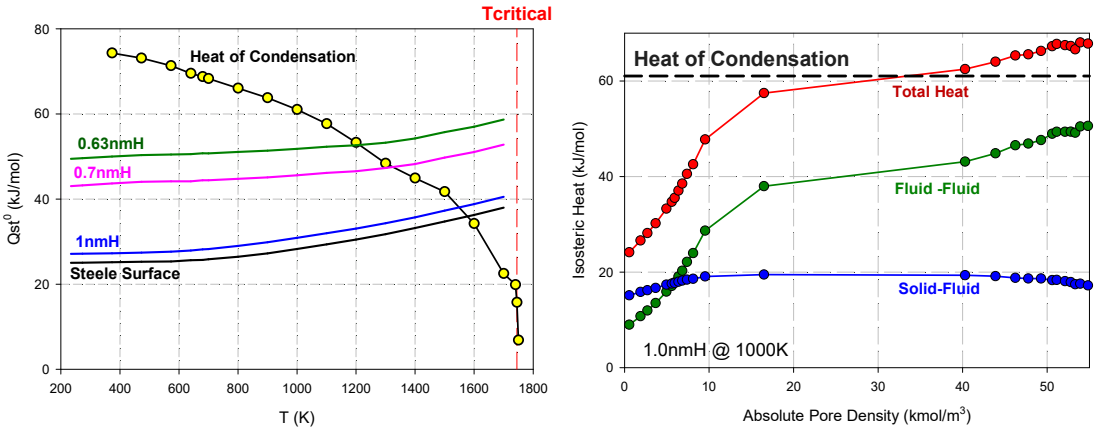

(a) (b)

Figure 6.2 (a) Isosteric heat at zero loading versus temperature compared with heat of condensation, (b) Isosteric heat versus loading in 1.0 nm width pore at 1000 K. The zero coverage heat was obtained by Monte Carlo integration (MCI) [206].

For a given pore size, there exists a filling temperature, T_F, below which mercury does not fill the pore, as seen in the low adsorbed density and the crossing of the isotherm with the P_0 axis. For pore widths of 0.7 nm, 1 nm and 2 nm, the corresponding filling temperatures are 423 K, 800 K and 1200 K, respectively. On the other hand, filling occurs in 0.63 nm ultrafine pore for all temperatures studied. This suggests that to remove mercury, the microporous carbons should be used because of the enhancement in the solid-fluid interactions. This is corroborated in the experimental work of Zeng et al. [207], where the volume of the adsorbed amount (assume it behaves like liquid) correlates with the volume of the ultra-fine pores (Appendix N).

The following features are summarized for a given pore:

1. For temperatures less than T_F, there is no filling of the pore space and non-wetting on the pore walls.
2. For temperatures greater than T_F, but less than the pore critical temperature T_P, the filling is first order, and when the temperature is greater than T_P, the

mechanism becomes continuous filling which is similar to the micropore filling introduced by Dubinin for simple gases adsorption in micropores [208].

3. After the filling has occurred, the trend of the isotherms with respect to temperature is opposite to that at low loadings, i.e. the adsorbed density is greater for lower temperature at a given reduced pressure. This is simply due to the combined solid-fluid and fluid-fluid interactions that leads to isosteric heat greater than the heat of condensation.

To corroborate the behaviour of the isotherm with respect to temperature, we showed in Figure 6.2a the isosteric heat at zero loading ($q_{st}^{(0)}$) and the heat of condensation (λ_{cond}) as a function of temperature. As long as the temperature is not too close to the critical temperature, $q_{st}^{(0)}$ is less than λ_{cond}, suggesting a non-wetting behaviour on a bare carbon surface or in an empty graphitic pore, a well-known fact that mercury is a non-wetting agent. For small pores, the isosteric heat at zero loading remains less than the heat of condensation, despite of the enhancement in the solid-fluid interaction. However, as the loading is increased, Figure 6.2b shows that the isosteric heat at a loading of 30 kmol/m^3 is comparable to the heat of condensation because of the increasing contribution from the fluid-fluid interaction, resulting in filling at this loading and beyond as shown in Figure 6.1c.

6.3.2 Canonical Simulations in 0.63nm Width Slit Pore at 323 K

To reveal the underlying mechanism of filling, in Figure 6.3 the canonical isotherm obtained from *2V-NVT* scheme in 0.63nm slit pore at 323 K (ambient condition) is presented together with the GCMC isotherm for comparison.

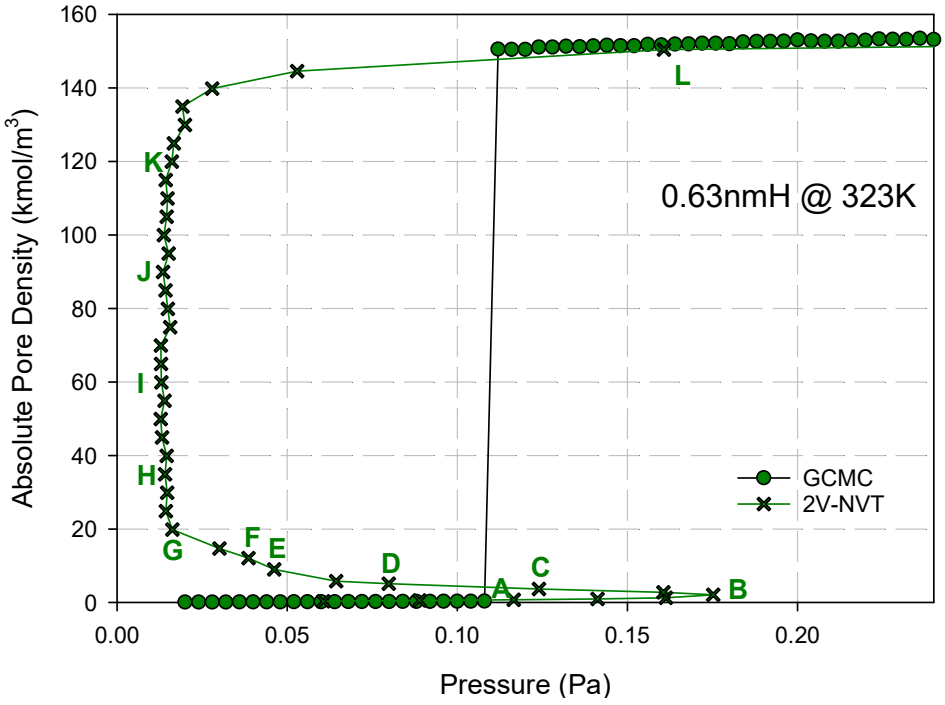

Figure 6.3 Isotherms of 0.63 nm width slit pore at 323 K (ambient condition) using 2V-NVT method (cross symbols). The isotherms obtained with GCMC are also shown with circle symbols.

Figure 6.4 shows the snapshots for Points A to L as marked in Figure 6.3. This 0.63 nm pore accommodates only one layer of mercury molecules. The evolution of the molecular configuration shows that mercury adsorbs negligibly at very low pressure (A) and molecules are distributed sparsely within the confined space (B-C), followed by the nucleation of two distinct clusters (D-F) which then coalesce (G), progressively fill the pore (H-K) at constant chemical potential, indicating the broadening of the adsorbed phase with a flat interface, and finally densification is seen at Point L.

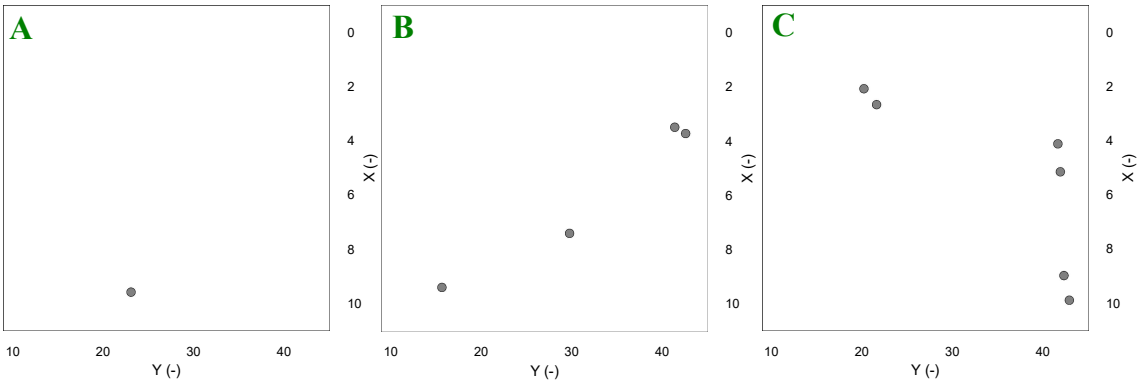

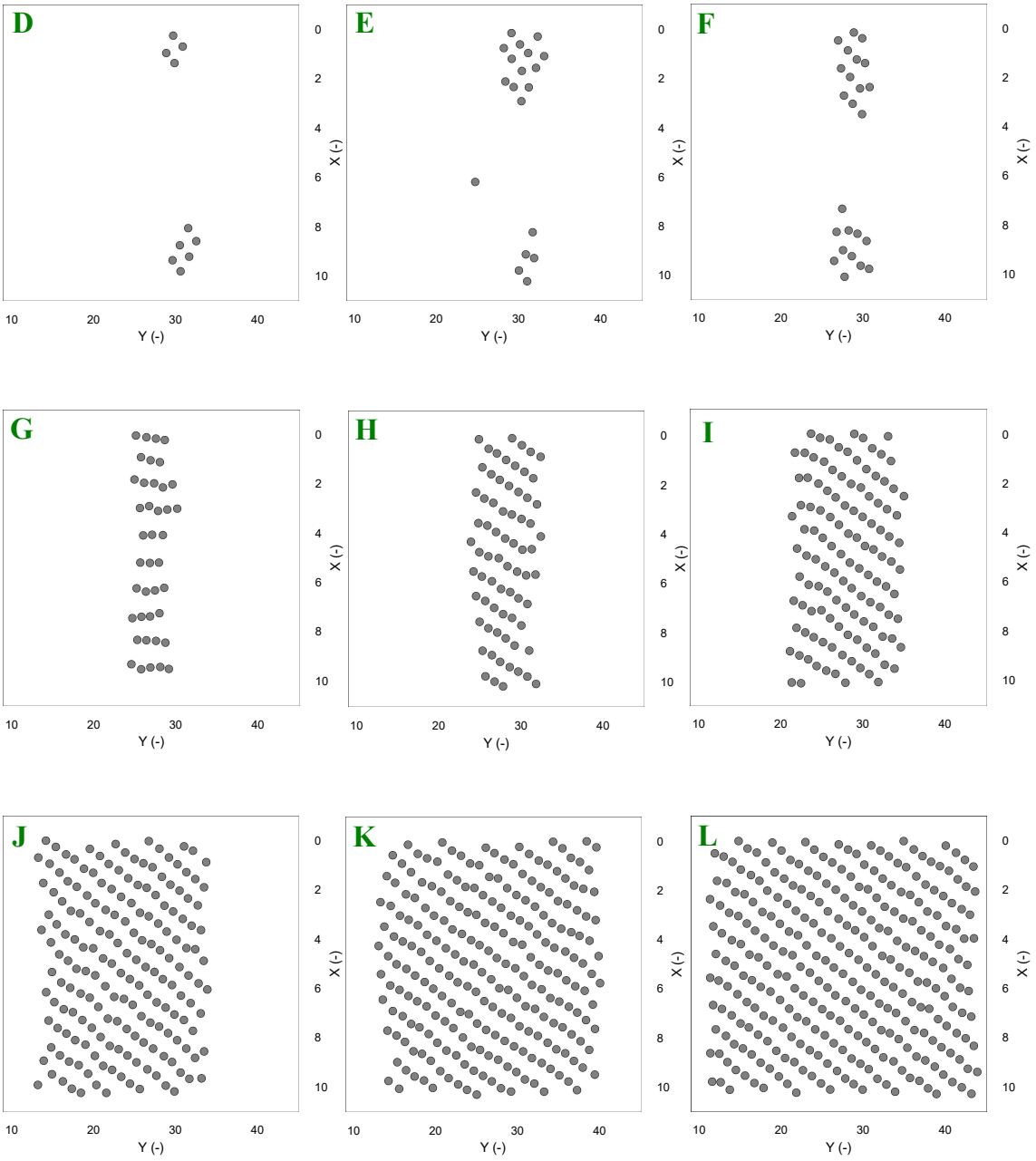

Figure 6.4 Top view of snapshots of the 0.63 nm width slit pore at 323 K using 2V-NVT method. Point A to L are as labelled in Figure 6.3.

The canonical simulation results at 800 K and 1000 K for 1nm slit pore which can accommodate two layers of mercury molecules are also presented in Appendix E. Formation of clusters is present at 800 K (T_F) but absent at 1000 K (T_P) due to the entropic effects.

6.4 Conclusions

In this chapter, we carried out the study to provide insight into mercury adsorption removal using the newly developed potential model for mercury, its functional form is compatible with the potentials of other fluids and solids readily available in the literature. Mercury adsorption within carbonaceous pores were studied with MC simulation for the first time. The wetting temperature of mercury on graphite was found to be 1600 K, supporting the fact that mercury does not wet carbon under ambient conditions. Furthermore, mercury can fill the ultrafine graphitic pores (less than 0.7 nm) at ambient temperatures even though it does not wet the surface. This is brought about by the enhancement in the solid-fluid interaction. Our simulation results are supported with the experimental data of Zeng et al. [207].

Chapter 7. Conclusions and Recommendations

This thesis has presented a fundamental study on the gas adsorption in carbonaceous materials with more realistic models, including wedge pore and connected deformable pore. Monte Carlo simulation was used to evaluate the adsorbate potentials and investigate the mechanisms of various adsorption phenomena. A special effort also has been spent on developing a new mercury potential model to improve the understanding of mercury interaction with carbonaceous materials, which has important practical application in industry.

7.1 Conclusions

The first objective of this thesis was realized through the phase equilibria (*VSE* and *VLE*) studies with Bin-CMC scheme to evaluate the selected potential models which is a precondition for subsequent adsorption studies. We have found that the potentials of Ar and Xe can predict their corresponding bulk phase behaviours (gas, liquid and solid phases) and agree well with the experimental data of other thermodynamic properties (saturation vapor pressure, enthalpy of phase change and surface tension). Triple point obtained with simulation also match with the experimental values and exhibited as the discontinuity in dense phase and enthalpy of phase change, indicating a switch in dense phase from liquid to solid.

Following the success in the evaluation of the selected models for Ar and Xe, their adsorption behaviors in the two more realistic pore models, including the wedge pore and deformable connected pore, were investigated with the combination of grand canonical and canonical ensembles. Subcritical adsorption of xenon in wedge pores exhibits a step-wise behaviour under a critical value of temperature (boiling point). The microscopic origin is due to the alternation in molecular configuration of commensurate packing (orderly domains) and incommensurate packing (structureless junctions), which is facilitated by low temperature. The lengths of the domains depend

only on the pore angle while the pore widths of the junctions are not affected by the pore angle, pore length and temperature. Then, the existence of hysteresis was proved in closed-end wedge pores at temperatures below the triple point and when the pore angle is less than a critical value. The hysteresis is caused by the formation and evaporation of a domain, and each domain has its own characteristic temperature above which it becomes disordered and there is no first-order transition and no hysteresis. The functional form of the Cohan equation was used to relate the radius of curvature of the interface to the bulk pressure and we found the condensed phase is not as structured as the bulk solid, but is denser than the supercool liquid. After that, adsorption-induced deformation in connected deformable pore was investigated, showing that the micro- narrow section is more dominating (especially at low pressure) and determines the general major shape of the strain isotherm, while the meso- wide section comes into effect at high pressure. The increase of the ratio of the length of narrow section to the total length can further strengthen this dominating role and even trigger the occurrence of hysteresis under critical temperature when this value exceeds 0.5. This hysteresis is due to the packing change of particles when bulk modulus is lowered to a critical value by increasing the number of movable layers or decreasing the solid affinity.

Finally, a study on mercury adsorption with carbonaceous materials was attempted to provide insight into mercury removal, which included the development of a new state-dependent potential for mercury by the potential evaluation process whose functional form is compatible with the potentials of other fluids and solids readily available in the literature. Mercury adsorption within carbonaceous pores was studied with *MC* simulation for the first time. The wetting temperature of mercury on graphite was found to be 1600 K, supporting the fact that mercury does not wet carbon under ambient conditions. Furthermore, mercury can fill the ultrafine graphitic pores (less than 0.7nm) at ambient temperatures even though it does not wet the surface, which is brought about by the enhancement of the solid-fluid potential and the strong intermolecular interactions. Simulated adsorption data agree qualitatively well with

experimental measurement.

7.2 Recommendations

7.2.1 More Sophisticated Potential Model for Mercury

In Chapter 3, we developed a single-site potential model for mercury, which has thrown a light upon the physisorption of mercury in porous materials as shown in Chapter 6. However, as has been reported in literatures, chemisorption plays an important role in mercury adsorption in solids which are composed of not only carbon but other substances, such as halogens, sulphur, etc., and this cannot be handled with the current model. To mimic the real process and realize the simulation of both physi- and chemi- sorption, it is essential to develop a more sophisticated potential model for mercury.

7.2.2 Proper Adsorbent Model for Mercury

Due to the limited duration of my PhD study, the more realistic solid models that tested for argon and xenon were not applied to mercury adsorption but only the ideal slit pore models. In future work, more realistic pore models should be considered, not only considering the geophysical heterogeneity, such as wedge pore and connected pore, but also bringing the surface chemistry factors into consideration, for example, different type of functional groups.

7.2.3 Mixture Adsorption

Mercury is known to be coexisting with many other components in industrial gases, e.g. natural gas, flue gas, etc. Therefore, it is necessary to consider the competition effects of other components on the mercury adsorption. For example, for the removal of mercury from natural gas, the mixture adsorption of mercury and methane should be conducted to reveal the adsorption mechanisms for the purpose of improving the mercury removal technology as well as guiding the development of novel adsorbents.

References

1. Dabrowski, A., *Adsorption - from theory to practice.* Advances in Colloid and Interface Science, 2001. **93**(1-3): p. 135-224.
2. Gregg, S.J. and K.S.W. Sing, eds. *Adsorption, Surface Area and Porosity*. Second ed. 1982, Academic press INC.: New York.
3. Walton, K.S. and R.Q. Snurr, *Applicability of the BET Method for Determining Surface Areas of Microporous Metal-Organic Frameworks.* Journal of the American Chemical Society 2007. **129**: p. 8552-8556.
4. Fan, C., et al., *New Method to Determine Surface Area and Its Energy Distribution for Nonporous Solids: A Computer Simulation and Experimental Study.* Langmuir, 2010. **26**(8): p. 5610-5623.
5. Herrera, L.F., et al., *Novel Method To Determine Accessible Volume, Area, and Pore Size Distribution of Activated Carbon.* Industrial & Engineering Chemistry Research, 2011. **50**(7): p. 4150-4160.
6. Langmuir, I., *The adsorption of gases on plane surfaces of glass, mica and platinum.* Journal of the American Chemical Society, 1918. **40**: p. 1361-1402.
7. Brunauer, S., P.H. Emmett, and T. Edward, *Adsorption of gases in multimolecular layers.* Journal of the American Chemical Society, 1938. **60**: p. 309 - 319.
8. Frenkel, D. and B. Smit, *Understanding molecular simulation : From algorithms to applications.* Second ed. Computational Science Series, ed. D. Frenkel, et al. 2002, San Diego: Academic Press. 638.
9. Nicholson, D. and G. Parsonage, *Computer simulation and the statistical mechanics of adsorption*. 1982, London: Academic Press.
10. Möller, D. and J. Fischer, *Determination of an effective intermolecular potential for carbon dioxide using vapour-liquid phase equilibria from NpT + test particle simulations.* Fluid Phase Equilibria, 1994. **100**(C): p. 35-61.
11. Birkett, G.R. and D.D. Do, *PVT behaviour of fluids with potential models optimised for phase equilibria.* Fluid Phase Equilibria, 2004. **224**(2): p. 199-212.
12. Mick, J.R., et al., *Optimized Mie potentials for phase equilibria: Application to noble gases and their mixtures with n-alkanes.* J Chem Phys, 2015. **143**(11): p. 114504.
13. Fan, C., et al., *A novel application of kinetic Monte Carlo method in the description of N2 vapour–liquid equilibria and adsorption.* Chemical Engineering Science, 2013. **90**(0): p. 161-169.
14. Errington, J.R. and A. Panagiotopoulos, *Phase equilibria of the modified Buckingham exponential-6 potential from Hamiltonian scaling grand canonical Monte Carlo.* Journal of Chemical Physics, 1998. **109**(3): p. 1093-1100.
15. Ohba, T., D. Nicholson, and K. Kaneko, *Temperature Dependence of*

Micropore Filling of N2 in Slit-Shaped Carbon Micropores: Experiment and Grand Canonical Monte Carlo Simulation. Langmuir, 2003. **19**(14): p. 5700-5707.

16. Do, D.D. and H.D. Do, *Cooperative and Competitive Adsorption of Ethylene, Ethane, Nitrogen and Argon on Graphitized Carbon Black and in Slit Pores.* Adsorption, 2005. **11**(1): p. 35-50.
17. Kanda, H. and M. Miyahara, *Sublimation phenomena of Lennard-Jones fluids in slit nanopores.* The Journal of Chemical Physics, 2007. **126**(5): p. 054703-4.
18. Ohba, T. and K. Kaneko, *Cluster-associated filling of water molecules in slit-shaped graphitic nanopores.* Molecular Physics, 2007. **105**(2-3): p. 139-145.
19. Jagiello, J. and J.P. Olivier, *2D-NLDFT adsorption models for carbon slit-shaped pores with surface energetical heterogeneity and geometrical corrugation.* Carbon, 2013. **55**: p. 70-80.
20. Fan, C., et al., *A molecular simulation study of adsorption and desorption in closed end slit pores: Is there a hysteresis loop?* Chemical Engineering Science, 2015. **121**: p. 313-321.
21. Kowalczyk, P., et al., *Storage of hydrogen at 303 K in graphite slitlike pores from grand canonical Monte Carlo simulation.* Journal of Physical Chemistry B, 2005. **109**(36): p. 17174-17183.
22. Liu, X. and X. He, *Effect of pore characteristics on coalbed methane adsorption in middle-high rank coals.* Adsorption, 2016. **23**(1): p. 3-12.
23. Bruschi, L., et al., *Adsorption on ordered and disordered duplex layers of porous anodic alumina.* Langmuir, 2015. **31**(17): p. 4895-905.
24. Hisashi, O. and Y. Fumiko, *Liquid–vapor coexistence curves of several interatomic model potentials.* J Chem Phys, 2000. **113**(20): p. 9162.
25. Vortler, H.L., I. Nezbeda, and M. Lisal, *The exp-6 potential fluid at very high pressures: computer simulations and theory.* Molecular Physics: An International Journal at the Interface Between Chemistry and Physics, 1997. **92**(5): p. 813-824.
26. Bojan, M.J. and W.A. Steele, *Computer simulation of physical adsorption on stepped surfaces.* Langmuir, 1993. **9**(10): p. 2569-2575.
27. Liu, L., et al., *Development of averaged solid–fluid potential energies for layers and solids of various geometries and dimensionality.* Adsorption, 2017. **24**(1): p. 1-9.
28. Steele, W.A., *The physical interaction of gases with crystalline solids: I. Gas-solid energies and properties of isolated adsorbed atoms.* Surface Science, 1973. **36**(1): p. 317-352.
29. Do, D.D. and H.D. Do, *Effects of potential models in the vapor–liquid equilibria and adsorption of simple gases on graphitized thermal carbon black* Fluid Phase Equilibria, 2005. **236**(1,2): p. 169-177
30. Panagiotopoulos, A.Z., *Monte Carlo methods for phase equilibria of fluids.* J. Phys.: Condens. Matter, 2000. **12**(Copyright (C) 2011 American Chemical Society (ACS). All Rights Reserved.): p. R25-R52.

31. Martin, M.G. and J.I. Siepmann, *Transferable Potentials for Phase Equilibria. 1. United-Atom Description of n-Alkanes.* The Journal of Physical Chemistry B, 1998. **102**(14): p. 2569-2577.
32. Wick, C.D., M.G. Martin, and J.I. Siepmann, *Transferable Potentials for Phase Equilibria. 4. United-Atom Description of Linear and Branched Alkenes and Alkylbenzenes.* J. Phys. Chem. B, 2000. **104**(33): p. 8008-8016.
33. Rai, N. and J.I. Siepmann, *Transferable Potentials for Phase Equilibria. 9. Explicit Hydrogen Description of Benzene and Five-Membered and Six-Membered Heterocyclic Aromatic Compounds.* The Journal of Physical Chemistry B, 2007. **111**(36): p. 10790-10799.
34. Eggimann, B.L., et al., *An online parameter and property database for the TraPPE force field.* Molecular Simulation, 2013. **40**(1-3): p. 101-105.
35. Kruk, M., J.R. Matos, and M. Jaroniec, *Argon and nitrogen adsorption studies of changes in connectivity of ordered cage-like large mesopores during the hydrothermal treatment.* Colloids and Surfaces A: Physicochemical and Engineering Aspects, 2004. **241**(1-3): p. 27-34.
36. Kruk, M. and M. Jaroniec, *Argon adsorption at 77 K as a useful tool for the elucidation of pore connectivity in ordered materials with large cagelike mesopores.* Chemistry of Materials, 2003. **15**(15): p. 2942-2949.
37. Shai, D.E., N.M. Urban, and M.W. Cole, *Structure and heat capacity of Ne and Xe adsorbed on a bundle of carbon nanotubes from Monte Carlo calculations.* Physical Review B, 2008. **77**(20).
38. Bojan, M.J. and W.A. Steele, *Computer simulations of the adsorption of xenon on stepped surfaces.* Molecular Physics: An International Journal at the Interface Between Chemistry and Physics, 1998. **95**(3): p. 431 - 437.
39. Prasetyo, L., et al., *The role of adsorbate size on adsorption of Ne and Xe on graphite.* J Colloid Interface Sci, 2018. **524**: p. 490-503.
40. Bonechi, A., M. Moraldi, and L. Frommhold, *Interaction-induced polarizability invariants and the interatomic potential of the mercury diatom.* The Journal of Chemical Physics, 1998. **109**(14): p. 5880-5885.
41. Pahl, E., et al., *A highly accurate potential energy curve for the mercury dimer.* J Chem Phys, 2010. **132**(11): p. 114301.
42. Schwerdtfeger, P., et al., *The potential energy curve and dipole polarizability tensor of mercury dimer.* The Journal of Chemical Physics, 2001. **115**(16): p. 7401.
43. Calderin, L., L.E. Gonzalez, and D.J. Gonzalez, *Static, dynamic and electronic properties of expanded fluid mercury in the metal-nonmetal transition range. An ab initio study.* J Phys Condens Matter, 2011. **23**(37): p. 375105.
44. Haberland, H.I., Bernd von; Yufeng, Ji; Kolar, Thomas; Thanner, Gregor, *Ground state and response properties of mercury clusters.* Z. Phys. D, 1993: p. 8-12.
45. Calvo, F., et al., *Diatomics-in-Molecules Modeling of Many-Body Effects on the Structure and Thermodynamics of Mercury Clusters.* J Chem Theory Comput, 2012. **8**(2): p. 639-48.

46. Inui, M., et al., *Critical Indices ν and γ Experimentally Obtained at the Liquid–Vapor Critical Point in Fluid Hg.* Journal of the Physical Society of Japan, 2016. **85**(3): p. 035001.
47. E. Czuchaj, F.R., H. Stoll, H. Preuss, *Calculation of ground- and excited- state potential energy curves for the Hg2 molecule in a pseudopotential approach.* Chemical Physics, 1997.
48. Munro, L.J., J.K. Johnson, and K.D. Jordan, *An interatomic potential for mercury dimer.* The Journal of Chemical Physics, 2001. **114**(13): p. 5545.
49. Schautz. F, F.H.-J., Dolg. M, *Quantum Monte Carlo study of Be_2 and group 12 dimers M_2 (M = Zn, Cd, Hg).* Theoretical Chemistry Accounts, 1998. **99**: p. 231-240.
50. Raabe, G. and R.J. Sadus, *Molecular simulation of the vapor–liquid coexistence of mercury.* The Journal of Chemical Physics, 2003. **119**(13): p. 6691.
51. Dolg, M. and H.-J. Flad, *Size dependent properties of Hgn clusters.* Molecular Physics, 1997. **91**(5): p. 815-826.
52. Barysz. Maria, I.Y., *Relativistic Methods for Chemists.* 2010. **10**.
53. Tomonari Sumi, E.M., Kiyoshi Tanaka, *Molecular-dynamics study of liquid mercury in the density region between metal and nonmetal.* PHYSICAL REVIEW B, 1999.
54. Bomont, J.M. and J.L. Bretonnet, *An effective pair potential for thermodynamics and structural properties of liquid mercury.* J Chem Phys, 2006. **124**(5): p. 054504.
55. Tang, H., et al., *Predictions of Hg0 and HgCl2 Adsorption Properties in UiO-66 from Flue Gas Using Molecular Simulations.* The Journal of Physical Chemistry C, 2019. **123**(10): p. 5972-5979.
56. Do, D.D. and H.D. Do, *Adsorption of carbon tetrachloride on graphitized thermal carbon black and in slit graphitic pores: Five-site versus one-site potential models.* J. Phys. Chem. B, 2006. **110**(19): p. 9520-9528.
57. Chen, B. and J.I. Siepmann, *Transferable Potentials for Phase Equilibria. 3. Explicit-Hydrogen Description of Normal Alkanes.* The Journal of Physical Chemistry B, 1999. **103**(25): p. 5370-5379.
58. Chen, B., J. Potoff, and I. Siepmann, *Monte Carlo Calculations for Alcohols and Their Mixtures with Alkanes. Transferable Potentials for Phase Equilibria. 5. United-Atom Description of Primary, Secondary, and Tertiary Alcohols.* J. Phys. Chem. B., 2001. **105**(15): p. 3093 - 3104.
59. Panagiotopoulos, A.Z., *Direct determination of phase coexistence properties of fluids by Monte Carlo simulation in a new ensemble.* Molecular Physics, 1987. **61**(4): p. 813-826.
60. Panagiotopoulos, A.Z., *Current advances in Monte Carlo methods.* Fluid Phase Equilibria, 1996. **116**(1-2): p. 257-266.
61. Blas, F., *Improved vapor-liquid equilibria predictions for Lennard-Jones chains from the statistical associating fluid dimer theory: Comparison with Monte Carlo simulations.* J. Chem. Phys., 2001. **115**(9): p. 4355-4358.

62. Gao, G. and W. Wang, *Gibbs Ensemble Monte Carlo simulation of binary vapor-liquid equilibria for CFC alternatives.* Fluid Phase Equilibria, 1997. **130**(1-2): p. 157-166.
63. Vega, L., *Phase equilibria and critical behavior of square-well fluids of variable width by Gibbs ensemble Monte Carlo simulation.* J. Chem. Phys., 1992. **96**(3): p. 2296-2305.
64. Panagiotopoulos, A.Z., *Direct Determination of Fluid Phase Equilibria by Simulation in the Gibbs Ensemble: A Review.* Molecular Simulation, 1992. **9**(1): p. 1-23.
65. Kofke, D., *Direct evaluation of phase coexistence by molecular simulation via integration along the saturation line.* J. Chem. Phys., 1993. **98**(5): p. 4149-4162.
66. Potoff, J.J., J.R. Errington, and A.Z. Panagiotopoulos, *Molecular Simulation of Phase Equilibria for Mixtures of Polar and Non-polar Components.* Molecular Physics, 1999. **97**(10): p. 1073 - 1083.
67. Fan, C., D.D. Do, and D. Nicholson, *A new and effective Bin–Monte Carlo scheme to study vapour–liquid equilibria and vapour–solid equilibria.* Fluid Phase Equilibria, 2012. **325**: p. 53-65.
68. Fan, C., D.D. Do, and D. Nicholson, *Bin-Monte Carlo simulation of ethylene coexistence and of ethylene adsorption on graphite.* Colloids and Surfaces A: Physicochemical and Engineering Aspects, 2013(0).
69. Nguyen, V.T., et al., *Development of kinetic Monte Carlo and Bin-Monte Carlo schemes for simulation of mixtures – vapor–liquid equilibria & adsorption.* Chemical Engineering Science, 2013. **102**: p. 220-226.
70. McBain, J.W., *An explanation of hysteresis in the hydration and dehydration of gels.* Journal of the American Chemical Society, 1935. **57**(1): p. 699-700.
71. Foster, A.G., *Sorption Hysteresis. Part I. Some factors determining the size of the hysteresis loop.* The Journal of Physical Chemistry, 1951. **55** (5): p. 638-643.
72. Everett, D.H., *Adsorption hysteresis*. The Solid-Gas Interface, ed. E.A. Flood. Vol. 2. 1967, New York: Marcel Dekker. 1055-1110.
73. Heffelfinger, G.S., F. van Swol, and K.E. Gubbins, *Adsorption hysteresis in narrow pores.* The Journal of Chemical Physics, 1988. **89**(8): p. 5202-5205.
74. Ravikovitch, P.I., et al., *Capillary Hysteresis in Nanopores: Theoretical and Experimental Studies of Nitrogen Adsorption on MCM-41.* Langmuir, 1995. **11**(12): p. 4765-4772.
75. Ball, P.C. and R. Evans, *Temperature dependence of gas adsorption on a mesoporous solid: capillary criticality and hysteresis.* Langmuir, 1989. **5**(3): p. 714-723.
76. Tompsett, G.A., et al., *Hysteresis and scanning behavior of mesoporous molecular sieves.* Langmuir, 2005. **21**(18): p. 8214-8225.
77. Morishige, K. and Y. Nakamura, *Nature of Adsorption and Desorption Branches in Cylindrical Pores.* Langmuir, 2004. **20**(No. 11): p. 4503-4506.
78. Diao, R., et al., *On the adsorbate restructuring induced hysteresis of simple*

gas adsorption in slit micropores. Chemical Engineering Journal, 2016. **290**: p. 381-390.

79. Prasetyo, L., et al., *A GCMC simulation and experimental study of krypton adsorption/desorption hysteresis on a graphite surface.* J Colloid Interface Sci, 2016. **478**: p. 402-12.
80. Diao, R., et al., *On the 2D-transition, hysteresis and thermodynamic equilibrium of Kr adsorption on a graphite surface.* J Colloid Interface Sci, 2015. **460**: p. 281-9.
81. Kresge, C.T., et al., *Ordered Mesoporous Molecular-Sieves Synthesized by A Liquid-Crystal Template Mechanism.* Nature, 1992. **359**(6397): p. 710-712.
82. Zhao, D.Y., et al., *Nonionic triblock and star diblock copolymer and oligomeric surfactant syntheses of highly ordered, hydrothermally stable, mesoporous silica structures.* Journal of the American Chemical Society, 1998. **120**(24): p. 6024-6036.
83. Thommes, M., et al., *Physisorption of gases, with special reference to the evaluation of surface area and pore size distribution (IUPAC Technical Report).* Pure and Applied Chemistry, 2015. **87**(9-10): p. 1051-1069.
84. De Boer, J.H., *The structure and texture of a physical adsorbent.* Colloques Internationaus du CNRS, 1972. **201**: p. 407.
85. Aoshima, M., T. Suzuki, and K. Kaneko, *Molecular association-mediated micropore filling of supercritical Xe in a graphite slit pore by grand canonical Monte Carlo simulation.* Chemical Physics Letters, 1999. **310**(1-2): p. 1-7.
86. Stoeckli, F., et al., *The comparison of experimental and calculated pore size distributions of activated carbons.* Carbon, 2002. **40**(3): p. 383-388.
87. Ustinov, E.A. and D.D. Do, *Adsorption in Slit-Like Pores of Activated Carbons: Improvement of the Horvath and Kawazoe Method.* Langmuir, 2002. **18**: p. 4637-4647.
88. Olivier, J.P., *Improving the models used for calculating the size distribution of micropore volume of activated carbons from adsorption data.* Carbon, 1998. **36**(10): p. 1469-1472.
89. Gusev, V.Y., J.A. Obrien, and N.A. Seaton, *A self-consistent method for characterization of activated carbons using supercritical adsorption and grand canonical Monte Carlo simulations.* Langmuir, 1997. **13**(10): p. 2815-2821.
90. Zeng, Y., et al., *Wedge Pore Model as an Alternative to the Uniform Slit Pore Model for the Determination of Pore Size Distribution in Activated Carbon.* The Journal of Physical Chemistry C, 2015. **119**(46): p. 25853-25859.
91. Monson, P.A., *Understanding adsorption/desorption hysteresis for fluids in mesoporous materials using simple molecular models and classical density functional theory.* Microporous and Mesoporous Materials, 2012. **160**: p. 47-66.
92. Landers, J., G.Y. Gor, and A.V. Neimark, *Density functional theory methods for characterization of porous materials.* Colloids and Surfaces A: Physicochemical and Engineering Aspects, 2013. **437**: p. 3-32.
93. Rouquerol, J., et al., *Recommendations for the Characterization of Porous*

Solids. Pure and Applied Chemistry, 1994. **66**(8): p. 1739-1758.
94. Jagiello, J. and J.P. Olivier, *Carbon slit pore model incorporating surface energetical heterogeneity and geometrical corrugation.* Adsorption-Journal of the International Adsorption Society, 2013. **19**(2-4): p. 777-783.
95. Guo, J., et al., *Topological defects: origin of nanopores and enhanced adsorption performance in nanoporous carbon.* Small, 2012. **8**(21): p. 3283-8.
96. Pan, J., et al., *The closed pores of tectonically deformed coal studied by small-angle X-ray scattering and liquid nitrogen adsorption.* Microporous and Mesoporous Materials, 2016. **224**: p. 245-252.
97. de Tomas, C., et al., *Transferability in interatomic potentials for carbon.* Carbon, 2019. **155**: p. 624-634.
98. Franklin, R.E., *Crystallite growth in graphitizing and nongraphitizing carbons.* Proceedings of the Royal Society of London, Series A, 1951. **209**: p. 196-218.
99. Philip, J.R., *Kinetics of Capillary Condensation in Wedge-Shaped Pores.* The Journal of Chemical Physics, 1964. **41**(4): p. 911-916.
100. Parlange, J.-Y., *Diffusion-Controlled Condensation and Evaporation in Wedge-Shaped Pores.* The Journal of Physical Chemistry, 1972. **76**(18): p. 2543-2547.
101. A. O. Parry, C.R., and A. J. Wood, *Universality for 2D Wedge Wetting.* PHYSICAL REVIEW LETTERS, 1999. **83**(26): p. 5535-5538.
102. Binder, K., *Modeling of wetting in restricted geometries.* Annual Review of Materials Research, 2008. **38**: p. 123-142.
103. Malijevsky, A. and A.O. Parry, *Density functional study of complete, first-order and critical wedge filling transitions.* J Phys Condens Matter, 2013. **25**(30): p. 305005.
104. Loi, Q.K., et al., *Order-disorder transition of an argon adsorbate in graphitic wedge pores.* Chemical Engineering Journal, 2020. **384**.
105. Nickmand, Z., et al., *GCMC simulation of argon adsorption in wedge shaped mesopores of finite length.* Adsorption, 2013. **19**(6): p. 1245-1252.
106. De Boer, J.H., *The Shape of Capillaries*, in *Structure and Properties of Porous Materials*, D.H. Everett and F.S. Stone, Editors. 1958, Colston Papers: London. p. 68.
107. Derjaguin, B., *A theory of capillary condensation in the pores of sorbents and of other capillary phenomena taking into account the disjoining action of polymolecular liquid films.* Acta Physicochimica Urss, 1940. **12**(2): p. 181-200.
108. Broekhoff, J.C.P. and J.H. De Boer, *Studies on pore systems in catalysts XIII. Pore distributions from the desorption branch of a nitrogen sorption isotherm in the case of cylindrical pores.* Journal of Catalysis, 1968(10): p. 377-390.
109. Cohan, L.H., *Sorption hysteresis and the vapor pressure of concave surfaces.* Journal of the American Chemical Society, 1938. **60**: p. 433-435.
110. Naumov, S., et al., *Understanding adsorption and desorption processes in mesoporous materials with independent disordered channels.* Physical Review E, 2009. **80**(3): p. 031607.
111. Ancilotto, F., et al., *Grand Canonical Monte Carlo study of argon adsorption*

in aluminium nanopores. Molecular Physics, 2011. **109**(23-24): p. 2787-2796.
112. Wallacher, D., et al., *Capillary Condensation in Linear Mesopores of Different Shape.* Physical Review Letters, 2004. **92**(19): p. 195704.
113. Grosman, A. and C. Ortega, *Capillary condensation in porous materials. Hysteresis and interaction mechanism without pore blocking/percolation process.* Langmuir, 2008. **24**(8): p. 3977-3986.
114. Bruschi, L., et al., *Adsorption hysteresis in self-ordered nanoporous alumina.* Langmuir, 2008. **24**(19): p. 10936-10941.
115. Bruschi, L., et al., *Capillary Condensation and Evaporation in Alumina Nanopores with Controlled Modulations.* Langmuir, 2010. **26**(14): p. 11894-11898.
116. Gelb, L.D., *The ins and outs of capillary condensation in cylindrical pores.* Molecular Physics, 2002. **100**(13): p. 2049-2057.
117. Fan, C., D.D. Do, and D. Nicholson, *On the Cavitation and Pore Blocking in Slit-Shaped Ink-Bottle Pores.* Langmuir, 2011. **27**(7): p. 3511-3526.
118. Paul, R. and H. Rieger, *Condensation phenomena in nanopores: A Monte Carlo study.* The Journal of Chemical Physics, 2005. **123**(2): p. 024708-7.
119. Grosman, A. and C. Ortega, *Influence of elastic deformation of porous materials in adsorption-desorption process: A thermodynamic approach.* Physical Review B: Condensed Matter and Materials Physics, 2008. **78**(8): p. 085433/1-085433/12.
120. Zeng, Y., et al., *On the hysteresis of adsorption and desorption of simple gases in open end and closed end pores.* Chemical Engineering Science, 2017. **158**: p. 462-479.
121. Rasmussen, C.J., et al., *Cavitation in Metastable Liquid Nitrogen Confined to Nanoscale Pores.* Langmuir, 2010. **26**(12): p. 10147-10157.
122. Ravikovitch, P.I. and A.V. Neimark, *Density Functional Theory of Adsorption in Spherical Cavities and Pore Size Characterization of Templated Nanoporous Silicas with Cubic and Three-Dimensional Hexagonal Structures.* Langmuir, 2002. **18**(5): p. 1550-1560.
123. Morishige, K., et al., *Change in Desorption Mechanism from Pore Blocking to Cavitation with Temperature for Nitrogen in Ordered Silica with Cagelike Pores.* Langmuir, 2006. **22**(22): p. 9920-9924.
124. Kleitz, F., et al., *Probing Adsorption, Pore Condensation, and Hysteresis Behavior of Pure Fluids in Three-Dimensional Cubic Mesoporous KIT-6 Silica.* The Journal of Physical Chemistry C, 2010. **114**(20): p. 9344-9355.
125. Zeng, Y., et al., *Evaporation from an Ink-Bottle Pore: Mechanisms of Adsorption and Desorption.* Industrial & Engineering Chemistry Research, 2014. **53**(40): p. 15467-15474.
126. A. L. Pulin, A.A.F., V. A. Sinitsyn, and A. A. Pribylov, *Adsorption and adsorption-induced deformation of NaX zeolite under high pressures of carbon dioxide.* Russian Chemical Bulletin, 2001. **50**(1): p. 60-62.
127. Yakovlev, V.Y., A.A. Fomkin, and A.V. Tvardovski, *Adsorption and deformation phenomena at the interaction of CO2 and a microporous carbon*

adsorbent. Journal of Colloid and Interface Science, 2003. **268**(1): p. 33-36.
128. Shkolin, A.V. and A.A. Fomkin, *Deformation of AUK microporous carbon adsorbent induced by methane adsorption.* Colloid Journal, 2009. **71**(1): p. 119-124.
129. Dacey, J.R.a.M.J.B.E., *Volume changes in saran charcoal caused by the adsorption of water, methanol and benzene vapours.* Carbon, 1971. **9**(5): p. 579-585.
130. Balzer, C., et al., *Deformation of porous carbons upon adsorption.* Langmuir, 2011. **27**(6): p. 2553-60.
131. Meehan, F.T., *The Expansion of Charcoal on Sorption of Carbon Dioxide.* Proceedings of the Royal Society of London A: Mathematical, Physical and Engineering Sciences, 1927. **115**(770): p. 199-207.
132. Bangham, D.H., N. Fakhoury, and A.F. Mohamed, *The swelling of charcoal. Part II. Some factors controlling the expansion caused by water, benzene and pyridine vapours.* Proceedings of the Royal Society of London A: Mathematical, Physical and Engineering Sciences, 1932. **138**(834): p. 162-183.
133. Scherer, G.W., *Dilatation of porous glass.* Journal of the American Ceramic Society, 1986. **69**(6): p. 473-480.
134. Kawaguchi, T.H., H; Iura, J, *SHRINKAGE BEHAVIOR OF SILICA GELS DURING DRYING.* Journal of Non-Crystalline Solids, 1988. **100**(1): p. 220-225.
135. Schneemann, A., et al., *Flexible metal-organic frameworks.* Chem Soc Rev, 2014. **43**(16): p. 6062-96.
136. Morak, R., et al., *Quantifying adsorption-induced deformation of nanoporous materials on different length scales.* J Appl Crystallogr, 2017. **50**(Pt 5): p. 1404-1410.
137. Prass, J., et al., *Capillarity-driven deformation of ordered nanoporous silica.* Applied Physics Letters, 2009. **95**(8).
138. Balzer, C., et al., *Adsorption-Induced Deformation of Hierarchically Structured Mesoporous Silica-Effect of Pore-Level Anisotropy.* Langmuir, 2017. **33**(22): p. 5592-5602.
139. Bangham, D.H.a.R.I.R., *The swelling of charcoal. Part V. The saturation and immersion expansions and the heat of wetting.* Proceedings of the Royal Society of London A: Mathematical, Physical and Engineering Sciences, 1938. **166**(927): p. 572-586.
140. Haines, R.S. and R. McIntosh, *Length Changes of Activated Carbon Rods Caused by Adsorption of Vapors.* The Journal of Chemical Physics, 1947. **15**(1): p. 28-38.
141. Flood, E.A.a.F.M.F., *Stresses and strains in adsorbent-adsorbate systems: V. thermodynamic theory of adsorption-extension phenomena.* Canadian Journal of Chemistry, 1963. **41**(7): p. 1703-1717.
142. Lakhanpal, M.L.a.E.A.F., *Stresses and strains in adsorbate-adsorbent systems: IV. contractions of activated carbon on adsorption of gases and vapors at low initial pressures.* Canadian Journal of Chemistry, 1957. **35**(8): p. 887-899.

143. Ravikovitch, P.I. and A.V. Neimark, *Density functional theory model of adsorption deformation.* Langmuir, 2006. **22**(26): p. 10864-8.
144. Do, D.D., D. Nicholson, and H.D. Do, *Effects of Adsorbent Deformation on the Adsorption of Gases in Slitlike Graphitic Pores: A Computer Simulation Study.* J. Phys. Chem. C, 2008. **112**: p. 14075-14089.
145. Nguyen, V.T., D.D. Do, and D. Nicholson, *Solid deformation induced by the adsorption of methane and methanol under sub- and supercritical conditions.* J Colloid Interface Sci, 2012. **388**(1): p. 209-18.
146. Diao, R., et al., *Monte Carlo Simulation of Adsorption-Induced Deformation in Finite Graphitic Slit Pores.* The Journal of Physical Chemistry C, 2016. **120**(51): p. 29272-29282.
147. Khatir, Y., M. Coulon, and L. Bonnetain, *Adsorption of Benzene on Exfoliated Graphite Between 70C and 5C.* Journal De Chimie Physique Et De Physico-Chimie Biologique, 1978. **75**(9): p. 789-795.
148. Metropolis, N. and S. Ulam, *The Monte Carlo method.* Journal of the American Statistical Association, 1949. **44**(247): p. 335-341.
149. Metropolis, N., et al., *Equation of state calculations by fast computing machines.* The Journal of Chemical Physics, 1953. **21**(6): p. 1087-1092.
150. Allen, M.P. and D.J. Tildesley *Computer Simulation of Liquids*. 1989, Oxford: Oxford University Press. xiii, 385.
151. Norman, G.E. and Filinov, *Investigation of phase transitions by a Monte Carlo method.* High Temp., 1969. **7**: p. 216-222.
152. Nguyen, V.T., D.D. Do, and D. Nicholson, *Monte Carlo Simulation of the Gas-Phase Volumetric Adsorption System: Effects of Dosing Volume Size, Incremental Dosing Amount, Pore Shape and Size, and Temperature.* The Journal of Physical Chemistry B, 2011. **115**(24): p. 7862-7871.
153. Neimark, A.V. and A. Vishnyakov, *Gauge cell method for simulation studies of phase transitions in confined systems.* Physical Review E, 2000. **62**(4): p. 4611-4622.
154. Neimark, A.V. and A. Vishnyakov, *A simulation method for the calculation of chemical potentials in small, inhomogeneous, and dense systems.* Journal of Chemical Physics, 2005. **122**(23).
155. Stone, A.J., *The theory of intermolecular forces*. 1997: Oxfor University Press. 276.
156. Michels, A., H. Wijker, and H.K. Wijker, *Isotherms of argon between 0°C and 150°C and pressures up to 2900 atmospheres.* Physica, 1949. **15**(7): p. 627-633.
157. Reid, R.C.P., J. M.; Sherwood, T. K, *Properties of Gases and Liquids*. 1985, New York: McGraw-Hill.
158. H. R. Palser, A., *Interlayer interactions in graphite and carbon nanotubes.* Physical Chemistry Chemical Physics, 1999. **1**(18): p. 4459-4464.
159. Fan, C., et al., *On the identification of the sharp spike in the heat curve for argon, nitrogen, and methane adsorption on graphite: Reconciliation between computer simulation and experiments.* The Journal of Physical Chemistry C, 2012. **116**(1): p. 953-962.

160. Steele, W.A., *International encyclopedia of physical chemistry and chemical physics, Topic 14, Vol. 3: The interaction of gases with solid surfaces*. 1974: Pergamon Press, Oxford. 356 pp.
161. Bojan, M.J. and W.A. Steele, *Computer simulation of physisorbed Kr on a heterogeneous surface.* Langmuir, 1989. **5**: p. 625-633.
162. Bojan, M.J. and W.A. Steele, *Computer simulation of physisorption on a heterogeneous surface.* Surface Science, 1988. **199**(3): p. L395-L402.
163. Widom, B., *Potential-distribution theory and the statistical mechanics of fluids.* The Journal of Physical Chemistry, 1982. **86**(6): p. 869-872.
164. Johnson, J.K., J.A. Zollweg, and K.E. Gubbins, *The Lennard-Jones equation of state revisited.* Molecular Physics: An International Journal at the Interface Between Chemistry and Physics, 1993. **78**(3): p. 591 - 618.
165. Kirkwood, J.G. and F.P. Buff, *The statistical mechanical theory of surface tension.* J. Chem. Phys., 1949. **17**: p. 338-343.
166. Do, D., et al., *The role of accessibility in the characterization of porous solids and their adsorption properties.* Adsorption, 2010. **16**(1): p. 3-15.
167. Do, D.D. and H.D. Do, *Appropriate volumes for adsorption isotherm studies: The absolute void volume, accessible pore volume and enclosing particle volume* Journal of Colloid and Interface Science, 2007. **316**(2): p. 317-330.
168. Do, D.D., H.D. Do, and D. Nicholson, *Molecular Simulation of Excess Isotherm and Excess Enthalpy Change in Gas-Phase Adsorption.* The Journal of Physical Chemistry B, 2009. **113**(4): p. 1030-1040.
169. Fan, C., D.D. Do, and D. Nicholson, *Condensation and Evaporation in Capillaries with Nonuniform Cross Sections.* Industrial & Engineering Chemistry Research, 2013. **52**(39): p. 14304-14314.
170. Qiao, C.Z., et al., *Connect the Thermodynamics of Bulk and Confined Fluids: Confinement-Adsorption Scaling.* Langmuir, 2019. **35**(10): p. 3840-3847.
171. Neyt, J.-C., et al., *Prediction of the Temperature Dependence of the Surface Tension Of SO2, N2, O2, and Ar by Monte Carlo Molecular Simulations.* J. Phys. Chem. B, 2011. **115**: p. 9421-9430.
172. *https://webbook.nist.gov/chemistry/.*
173. Fray, N. and B. Schmitt, *Sublimation of ices of astrophysical interest: A bibliographic review.* Planetary and Space Science, 2009. **57**(14-15): p. 2053-2080.
174. Perry, R.H. and D.W. Green, *Perry's Chemical Engineers' Handbook*. Seventh ed. 1997, New York: McGraw-Hill.
175. Ferreira, A.G.M. and L.Q. Lobo, *The sublimation of argon, krypton, and xenon.* The Journal of Chemical Thermodynamics, 2008. **40**(12): p. 1621-1626.
176. Bomont, J.M. and J.L. Bretonnet, *A molecular dynamics study of density profiles at the free surface of liquid mercury.* Journal of Physics: Conference Series, 2008. **98**(4): p. 042018.
177. Bomont, J.-M., J. Delhommelle, and J.-L. Bretonnet, *Structure and thermodynamics of the expanded liquid mercury by Monte Carlo simulation: a first attempt.* Journal of Non-Crystalline Solids, 2007. **353**(32-40): p. 3454-

3458.
178. Desgranges, C. and J. Delhommelle, *Thermodynamics of phase coexistence and metal-nonmetal transition in mercury: assessment of effective potentials via expanded Wang-Landau simulations.* J Phys Chem B, 2014. **118**(11): p. 3175-82.
179. Liessmann, G., W. Schmidt, and S. Reiffarth, *Data Compilation of the Saechsische Olefinwerke Boehlen.* Germany, 1995.
180. Huber, M.L., A. Laesecke, and D.G. Friend, *Correlation for the Vapor Pressure of Mercury.* Ind. Eng. Chem. Res., 2006. **45**(21): p. 7351-7361.
181. http://mercury.atomistry.com/physical_properties.html.
182. Kernaghan, M., *Surface Tension of Mercury.* Physical Review, 1931. **37**(8): p. 990-997.
183. Trokhymchuk, A. and J. Alejandre, *Computer simulations of liquid/vapor interface in Lennard-Jones fluids: Some questions and answers.* The Journal of Chemical Physics, 1999. **111**(18): p. 8510-8523.
184. Biscay, F., et al., *Calculation of the surface tension from Monte Carlo simulations: Does the model impact on the finite-size effects?* The Journal of Chemical Physics, 2009. **130**(18): p. 184710-13.
185. Fan, C., et al., *Novel approach to the characterization of the pore structure and surface chemistry of porous carbon with Ar, N2, H2O and CH3OH adsorption.* Microporous and Mesoporous Materials, 2015. **209**: p. 79-89.
186. Phadungbut, P., et al., *Computational methodology for determining textural properties of simulated porous carbons.* J Colloid Interface Sci, 2017. **503**: p. 28-38.
187. Vanin, A.A. and E.N. Brodskaya, *Computer simulation of Lennard-Jones fluid adsorption in wedge-shaped pores with smooth walls.* Colloid Journal, 2011. **73**(4): p. 445-452.
188. Klomkliang, N., D.D. Do, and D. Nicholson, *Hysteresis loop and scanning curves of argon adsorption in closed-end wedge pores.* Langmuir, 2014. **30**(43): p. 12879-87.
189. Mountain, R.D. and D. Thirumalai, *Quantitative measure of efficiency of Monte Carlo simulations.* Physica A (Amsterdam), 1994. **210**(3-4): p. 453-460.
190. Nguyen, V.T., D.D. Do, and D. Nicholson, *Microscopic configurations of methanol molecules in graphitic slit micropores: a computer simulation study.* J Colloid Interface Sci, 2013. **396**: p. 215-26.
191. Michels, A.W., T., *Vapour Pressure of Liquid Xenon.* Physica (Amsterdam), 1950. **16**(3): p. 253-256.
192. Barrer, R.M., N. Mckenzie, and J.S.S. Reay, *Capillary condensation in single pores.* Journal of colloid science, 1956. **11**: p. 479-495.
193. Liu, X., C. Fan, and D.D. Do, *Microscopic characterization of xenon adsorption in wedge pores.* Adsorption, 2019. **25**(6): p. 1043-1055.
194. Tan, S.J., et al., *On the growth of argon clusters on a weak adsorbent decorated with patches.* J Colloid Interface Sci, 2019. **537**: p. 431-440.
195. Gor, G.Y., P. Huber, and N. Bernstein, *Adsorption-induced deformation of*

nanoporous materials—A review. Applied Physics Reviews, 2017. **4**(1): p. 011303.
196. Zeng, Y., et al., *A Monte Carlo study of adsorption-induced deformation in wedge-shaped graphitic micropores.* Chemical Engineering Journal, 2018. **346**: p. 672-681.
197. Kuang, M., et al., *Study on mercury desorption from silver-loaded activated carbon fibre and activated carbon fibre.* Journal of Fuel Chemistry and Technology, 2008. **36**(4): p. 468-473.
198. Hsi, H.-C. and C.-T. Chen, *Influences of acidic/oxidizing gases on elemental mercury adsorption equilibrium and kinetics of sulfur-impregnated activated carbon.* Fuel, 2012. **98**: p. 229-235.
199. Padak, B., et al., *Mercury binding on activated carbon.* Environmental Progress, 2006. **25**(4): p. 319-326.
200. Padak, B. and J. Wilcox, *Understanding mercury binding on activated carbon.* Carbon, 2009. **47**(12): p. 2855-2864.
201. Galashev, A.E., *Mercury droplet formation on a graphene surface. Computer experiment.* Colloid Journal, 2015. **77**(5): p. 582-591.
202. J. Y. Chen, A.K., C. P. Collier and K. P. Giapis, *Electrowetting in Carbon Nanotubes.* Science, 2005. **310**(New Series): p. 1480-1483.
203. Nguyen, V.T., D.D. Do, and D. Nicholson, *Reconciliation of different simulation methods in the determination of the equilibrium branch for adsorption in pores.* Molecular Simulation, 2014. **40**(7-9): p. 713-720.
204. Prasetyo, L., et al., *Cluster growth and coalescence of argon on weakly adsorbing substrates.* Colloids and Surfaces A: Physicochemical and Engineering Aspects, 2018. **554**: p. 169-179.
205. Prasetyo, L., et al., *Effects of temperature on the transition from clustering to layering for argon adsorption on substrates of different strength - Parametric map of wetting, pre-wetting and non-wetting.* Microporous and Mesoporous Materials, 2018.
206. Do, D.D., D. Nicholson, and H.D. Do, *On the Henry constant and isosteric heat at zero loading in gas phase adsorption.* Journal of Colloid and Interface Science, 2008. **324**(1-2): p. 15-24.
207. Zeng, H., F. Jin, and J. Guo, *Removal of elemental mercury from coal combustion flue gas by chloride-impregnated activated carbon.* Fuel, 2004. **83**(1): p. 143-146.
208. Gregg, S.J. and K.S.W. Sing, *Adsorption, surface area and porosity*. 2nd ed. ed. 1982, London: Academic Press.

Appendices

Appendix A

Table A1 LJ parameters of the new 12-6 LJ (T) model

T (K)	σ_{ff} (nm)	ε_{ff}/k_B (K)	$\sigma^6\varepsilon$ (nm^6K)
234	0.2916	1175.5	0.7227
273	0.2914	1175.6	0.7198
373	0.2908	1175.8	0.7110
473	0.29	1175.8	0.6994
573	0.288	1176.8	0.6715
640	0.2863	1179.8	0.6497
680	0.2861	1180.6	0.6475
700	0.2855	1181	0.6396
800	0.284	1183	0.6207
900	0.2819	1186.5	0.5954
1000	0.28	1193	0.5749
1100	0.278	1200	0.5539
1200	0.275	1205	0.5212
1300	0.273	1215	0.5030
1400	0.27	1248	0.4835
1500	0.269	1290	0.4888
1600	0.268	1315	0.4872
1700	0.2674	1352	0.4842
1740	0.266	1375	0.4871
1745	0.266	1378	0.4881

Appendix B

Figure B1 shows the potential profiles of the new 12-6 *LJ* (T) model and two conventional 12-6 *LJ* models. It clearly shows that for a given temperature the profile of the new model falls between those of the two conventional 12-6 LJ models. The same trend is observed when the potential curves of *RS* model are compared with those of the new 12-6 *LJ* (T) model, as shown in Figure B2.

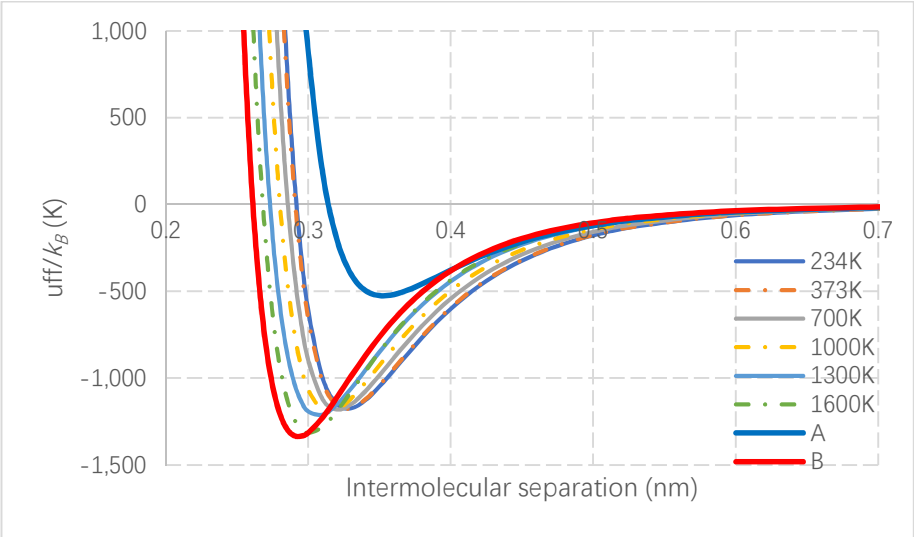

Figure B1 Potential curves of the new 12-6 LJ (T) model and two conventional 12-6 LJ models.

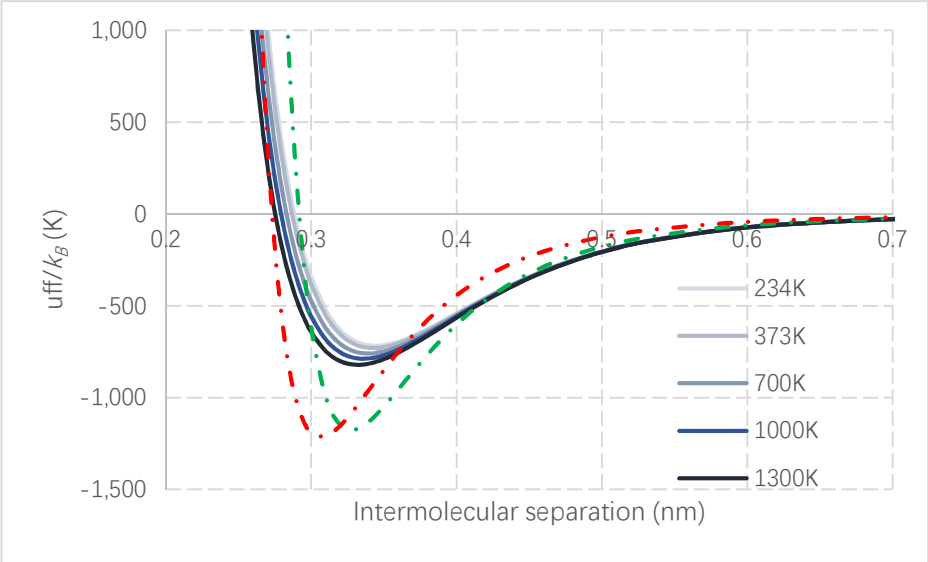

Figure B2 Potential curves of RS model and comparison with 12-6 LJ (T) model.

Appendix C

The saturation vapour pressures of xenon at different temperatures used in open wedge system, are determined by the Antoine equation [191], $\log_{10} P_0 = A - B/(T + C)$, with A=3.81, B=577.66 and C=−13, (P_0 in Pa, and T in K). Values of the saturation vapour pressure for various temperatures used in this chapter are tabulated in Table C1.

Table C1 The saturation vapour pressures of xenon at various temperatures (the triple point is 161K).

T (K)	134	**161**	165	167	170	200
P_0 (Pa)	1.08×10^4	8.01×10^4	1.02×10^5	1.14×10^5	1.34×10^5	5.22×10^5

Appendix D

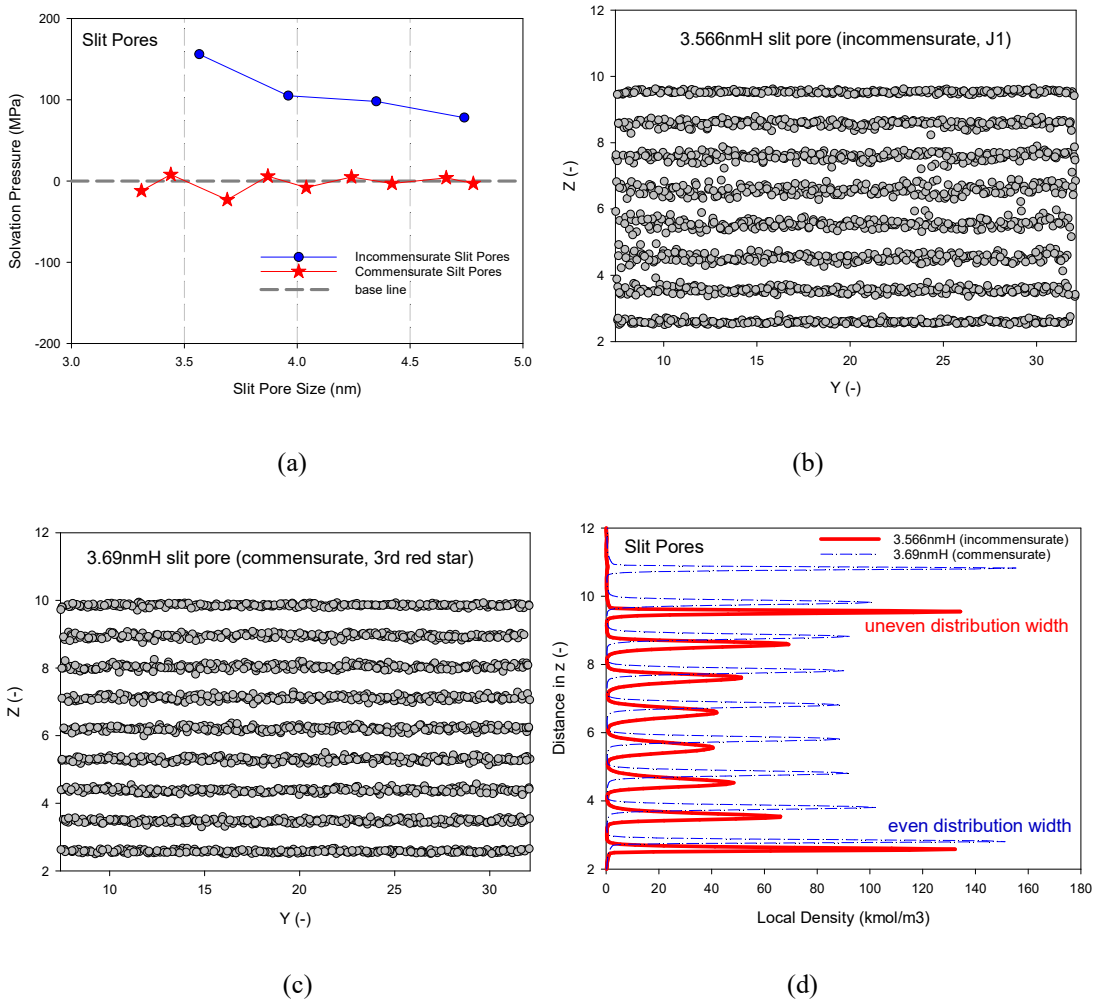

Figure D1 (a) Total solvation pressure for slits whose widths are the same as those at the junction and the domain; the blue circles denote the pore sizes at junctions, and the red stars denote the pore sizes whose solvation pressures are zero in Figure 4.3. Snapshots at the saturation pressures for xenon in slit pores of 10nm length at 134K with pore sizes of (b) 3.57 nm and (c) 3.69nm. The local denisty distribution at the saturation pressures for both slit pores are shown in (d).

Appendix E

The adsorption and desorption isotherm, the snapshots and the local solvation pressure distribution for argon adsorption at 70 K in the reference wedge pore are presented in Figure E1. Similar to xenon, the stepwise behaviour of the desorption branch is observed, but it is not as pronounced as that for xenon. This is due to the weaker intermolecular interactions of argon, and this is also reflected in the snapshot and the local solvation pressure. The bifurcation temperature of argon has been found to be lower but close to its boiling point, which is in agreement with what have been observed for xenon.

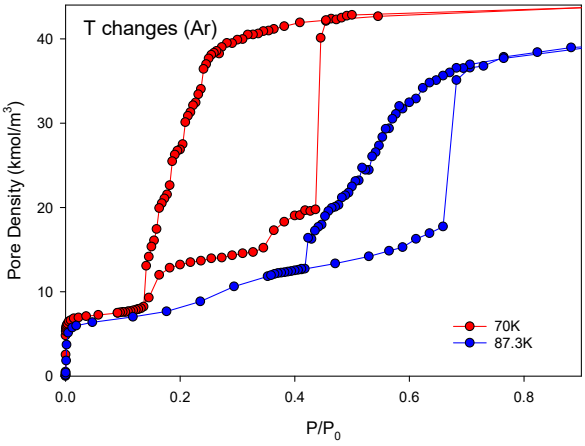

(a)

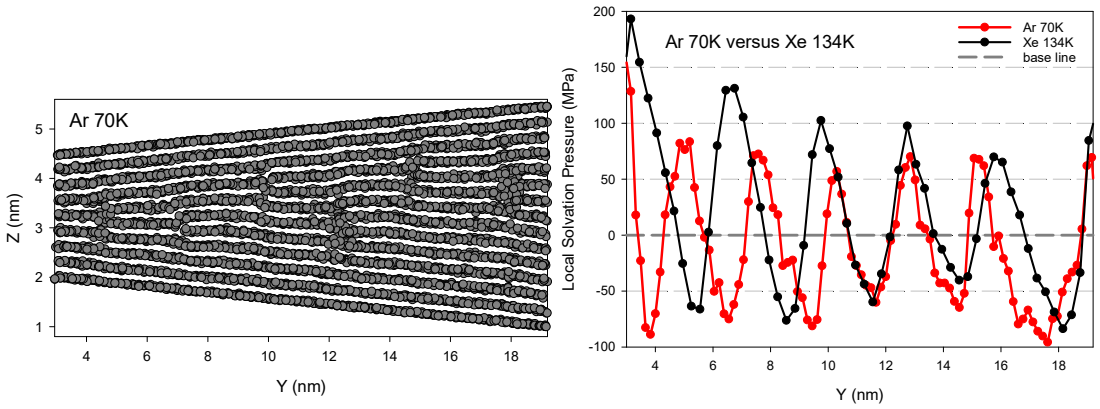

(b) (c)

Figure E1 (a) Isotherms of argon at 70K and 87.3K, (b) snapshot at the saturation vapour pressure of argon at 70K and (c) comparison of local solvation pressure distribution between argon at 70K and xenon at 134K in the reference wedge pore.

Appendix F

Figure F1 shows the isotherms and the snapshots for the wedge whose small end is SH=3.15nm and e angle of 2.1° for two different pore lengths L=16.2nm and 9.8nm. Similar behaviours as Case I presented in Section 4.3.4 were observed, with the exception that the domains I and II with the junction between them do not evaporate simultaneously, but rather evaporate sequentially. This is due to the enhancement of SF potential energy at the small end because of the smaller wedge angle.

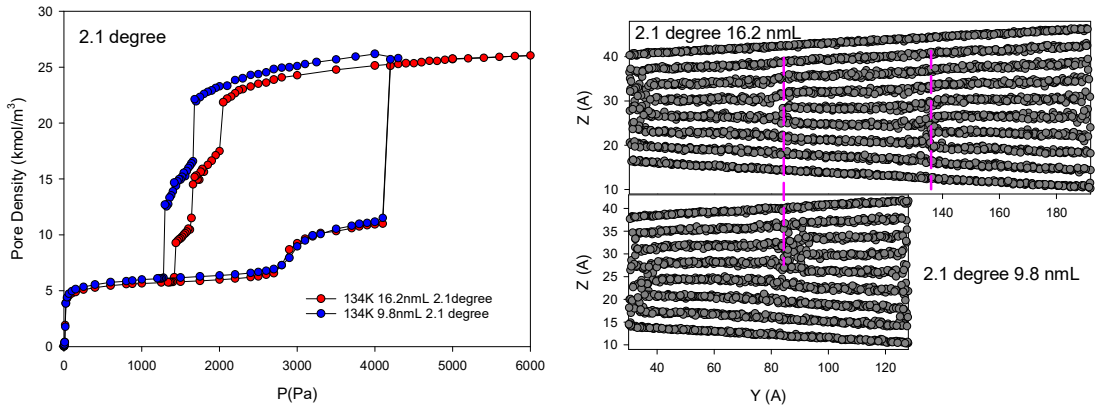

(a) (b)

Figure F1 (a) Isotherms and (b) snapshots at the saturation vapour pressures at 134K in wedge pores of different lengths L = 9.8 and 16.2 nm. The width of the small end is SH = 3.15nm and the angle is α = 2.1°. The width of the large ends for these two axial lengths are BH are 3.869nm and 4.338nm, respectively.

Appendix G

The simulated sublimation pressures for temperatures below the triple point temperature are determined from the vapor-solid equilibria (*VSE*) simulation. They are tabulated in Table G1 for the temperatures studied in this chapter.

Table G1 The simulated sublimation pressures for xenon at various temperatures below the simulated bulk triple point of 159K.

T (K)	130	134	140	145	148	150
P_0 (kPa)	4.5	6.7	12.0	18.8	23.8	28.2

The data above the triple point temperature determined from vapour-liquid equilibrium (*VLE*) simulation are listed in Table G2 and extrapolated to obtain the thermodynamic properties of supercooled liquid Xe at temperatures below the triple point (see Table 4.4 in Section 4.3.5).

Table G2 The thermodynamic properties for the bulk xenon obtained from *VLE* simulations (P_0 is the saturation pressure, γ is the surface tension and v_M is the liquid molar volume)

T (K)	$P_0(Pa)$	$\gamma(mJ/m^2)$	$v_M(m^3/mol)$
161	58652.5	20.6	4.75E-05
165	72949.6	19.5	4.80E-05
170	94771.7	18.9	4.84E-05
175	122145	17.4	4.89E-05
180	155989	16.1	4.95E-05
190	254769	15.2	5.07E-05
200	401314	14.8	5.20E-05

We determined the simulated triple point temperature by considering the variation of the saturation vapour pressure with respect to temperature as derived from the *VSE* and *VLE* simulations. This is shown in Figure G1 as plots of the logarithm of the saturation vapour pressures versus the inverse of temperature. Both *VSE* (red line) and *VLE* (blue line) results show a linear behaviour, and they intersect at the triple point of 159 K (compared to the experimental value of 161.4 K). The reliability of our method is also justified with the simulated heats of sublimation and evaporation of 15 kJ/mol and 13.2 kJ/mol, compared to the corresponding experimental values of 15.2 kJ/mol and 12.64 kJ/mol.

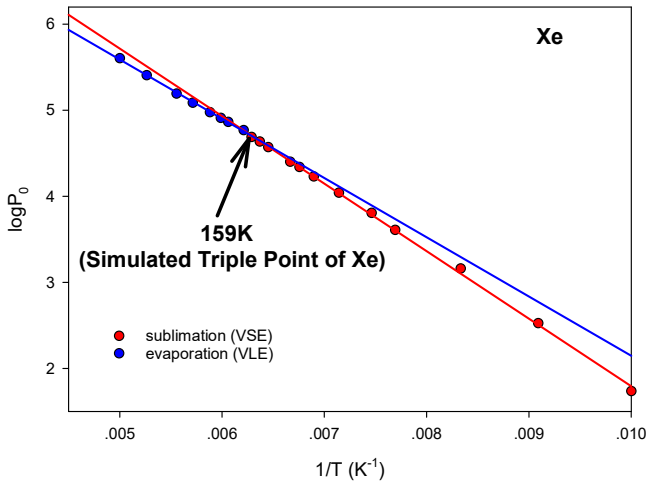

Figure G1 Saturation vapour pressure versus the inverse of the temperature for the bulk xenon for temperatures greater and less than the triple point temperature.

Appendix H

For the open wedge pore, the evaporation step at 2.2 kPa is corresponding to the evaporation of the domain at the larger end of the wedge, and that at 1.5 kPa is associated with the evaporation of the remaining two domains. For the closed wedge pore, the evaporation step at 2.2 kPa is similar to the open wedge pore, but the step at 1.5 kPa is due to the evaporation of the adjacent domain. The snapshots for these steps for the two wedge pores are shown in Figures H1 and H2, respectively.

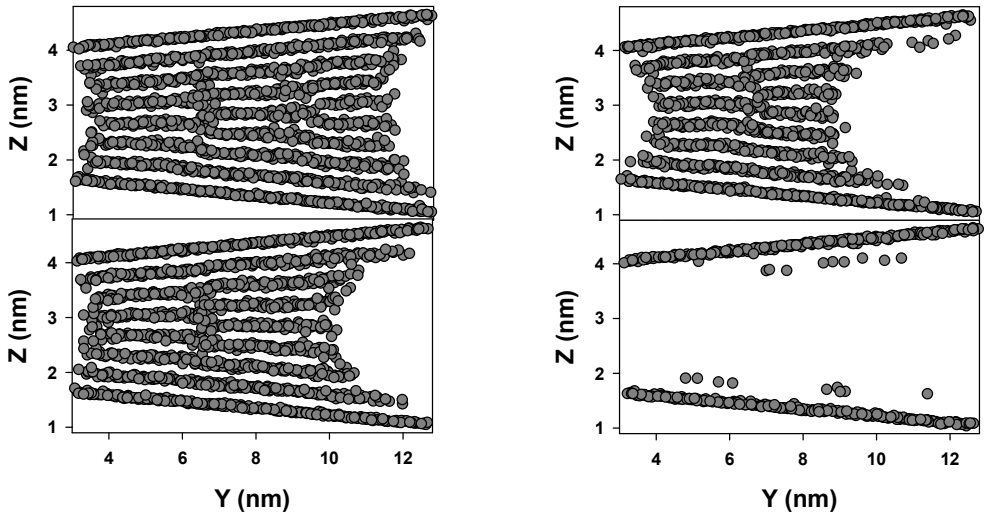

(a) (b)

Figure H1 Snapshots of the evaporation step for open wedge pore at (a) 2.2 kPa and (b) 1.5 kPa.

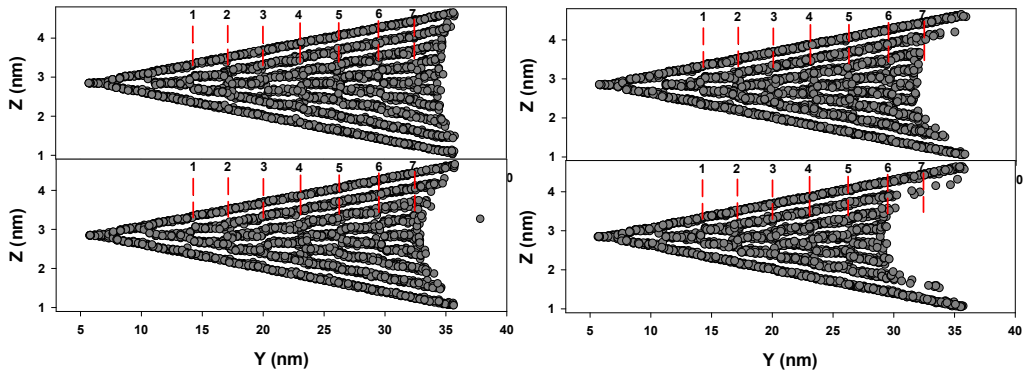

(a) (b)

Figure H2 Snapshots of the evaporation step for closed wedge pore at (a) 2.2 kPa and (b) 1.5 kPa.

Appendix I

Tables I1&2 summarize the status of the first three steps at various temperatures for xenon adsorption on surface and in closed-end wedge pore, respectively, either exist (E) or vanish (V). The critical/bifurcation temperature for each step has been indicated in the rightmost column.

Table I1 The critical temperatures for the first three layers on Steele surface for xenon.

T (K)	1st step	2nd step	3rd step	Tc
120	E	E	E	
130	V	E	E	1st step
134	V	E	E	
140	V	E	V	3rd step
145	V	V	V	2nd step

Table I2 The bifurcation temperatures for the three steps for xenon in a closed-end wedge pore with 3 loops.

T (K)	1st step	2nd step	3rd step	Tc
140	E	E	E	
142	E	E	E	
145	V	E	E	1st step
148	V	E	V	3rd step
150	V	V	V	2nd step

Appendix J

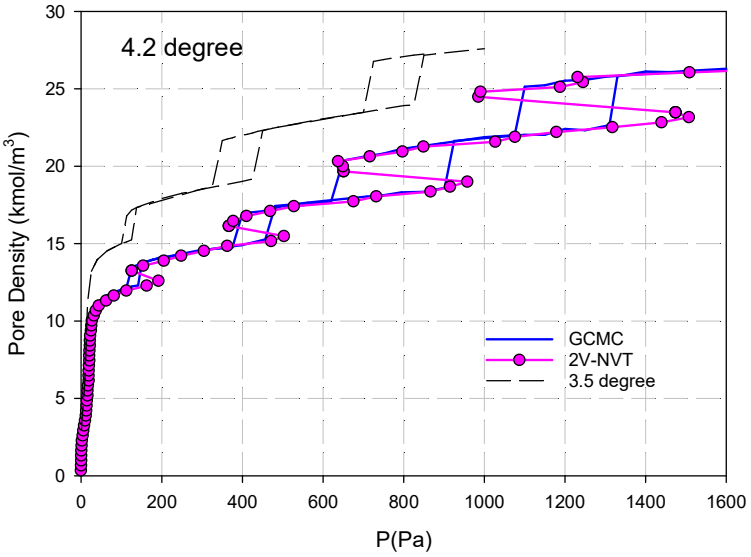

Figure J1 Plots of the canonical and grand canonical isotherms for xenon adsorption at 134K in a closed-end wedge with length L=20.6 nm. The solid and dashed lines represent wedges with a half angle α= 4.2 degrees and 3.5 degrees, respectively.

Appendix K

The effects of the half angle α were studied for xenon adsorption at 134K (Figure K1). For pores having half angles less than 90 degrees, their pore lengths *L* are adjusted to give the same accessible pore volume as that for the reference pore with *L*=20.6nm and α=3.5 degrees. In Figure K1b, the surface excess concentration is unified with the surface area in the 45-degree closed wedge for comparison purpose. The number of transitions in the isotherm for the reference pore is 3, and it reduces to 2 for the 6-degree pore, 1 for the 7-degree pore, and no transitions can be seen for pores with larger half angles. Snapshots at three specific pressures (125Pa, 300Pa and 500Pa) are selected to show the molecular configurations of the first and second domains, as shown in Figure K2. It is seen that the critical half angle for the second domain is between 6 and 7 degrees and that of the first domain is 18 degrees. For pores having half angles greater than 22.5 degrees, the adsorption mechanism is the same as that for surfaces, i.e. molecular layering. These results also substantiate the existence of hysteresis in the pore with *L*=20.6nm and α=3.5 degrees.

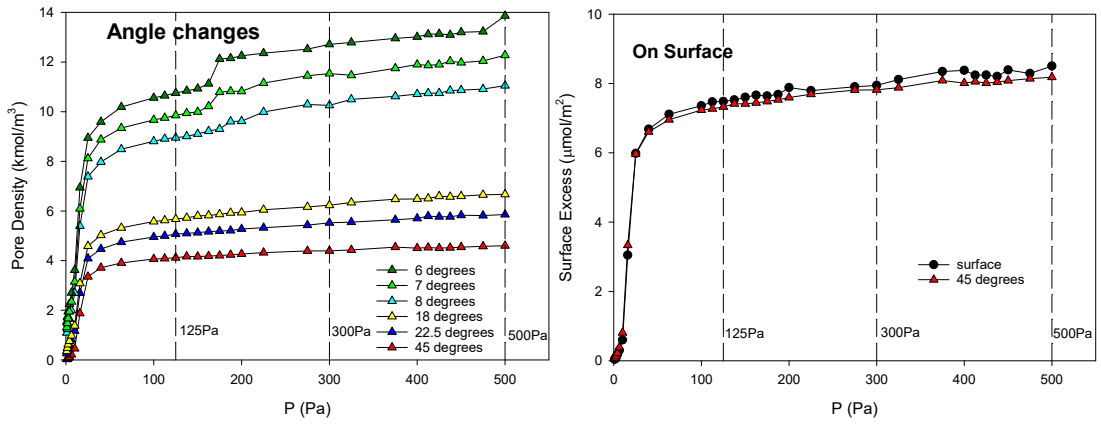

(a) (b)

Figure K1 The grand canonical isotherms for xenon adsorption at 134K (a) in closed-end wedge with various half angle and (b) on surface.

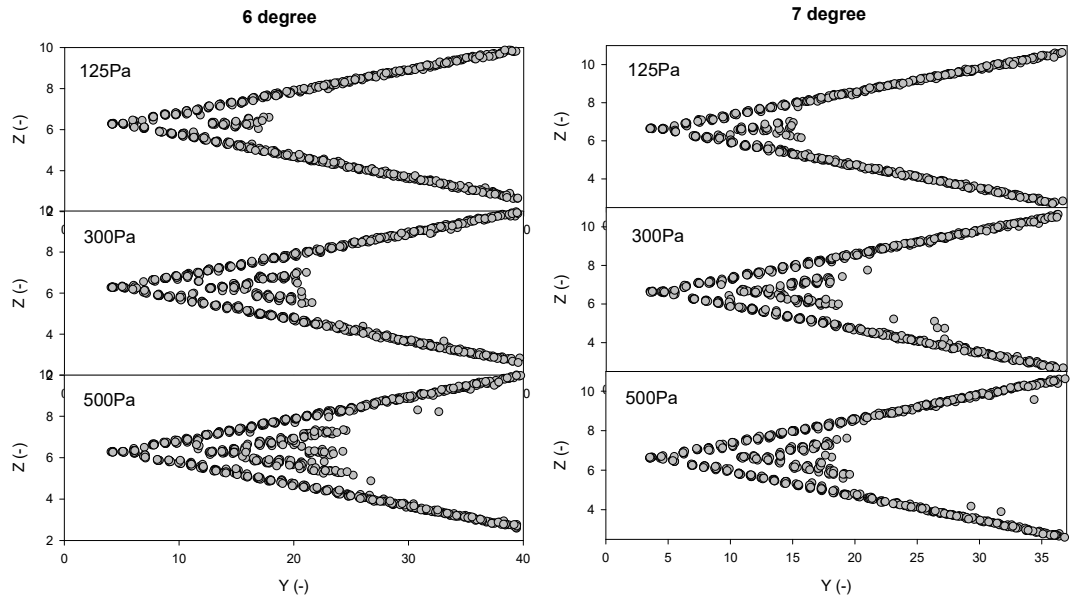

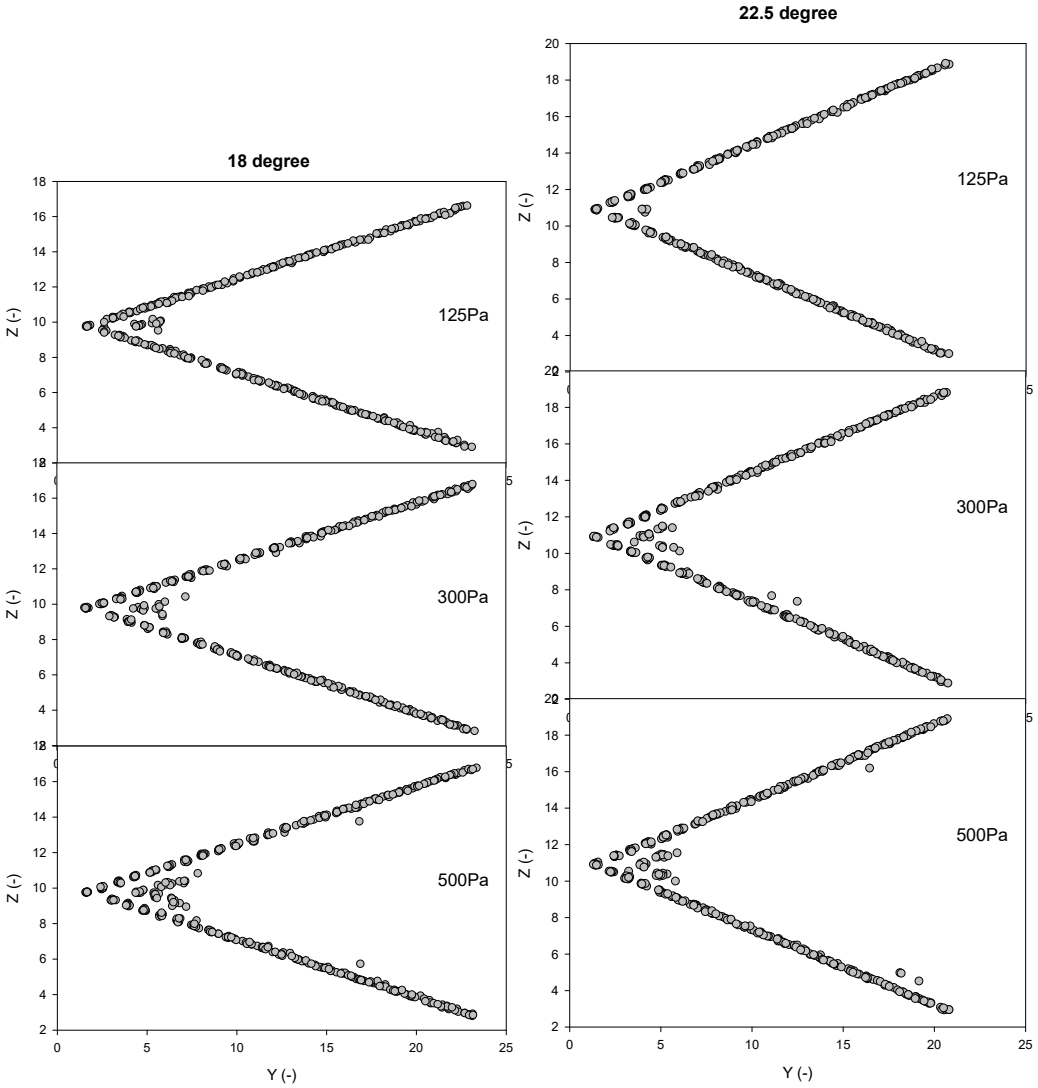
18 degree
125Pa
300Pa
500Pa
Z (-)
Y (-)
22.5 degree
125Pa
300Pa
500Pa
Z (-)
Y (-)

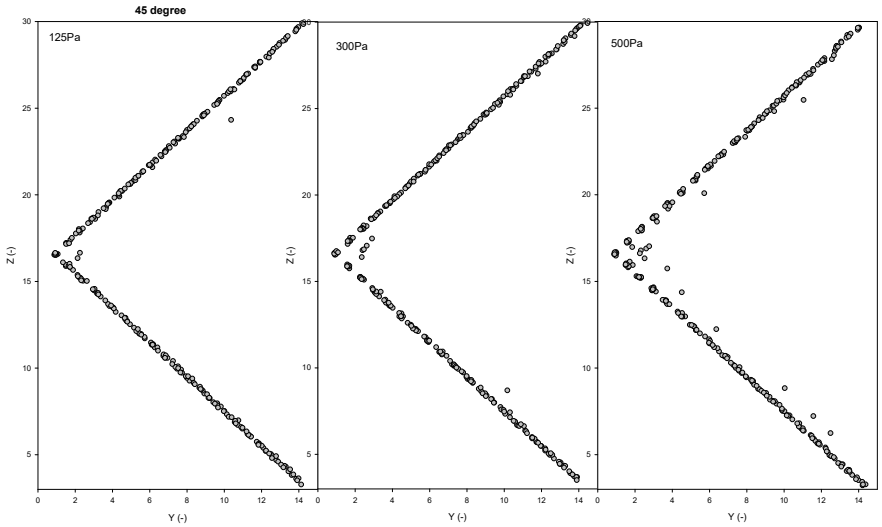
45 degree
125Pa
300Pa
500Pa
Z (-)
Y (-)

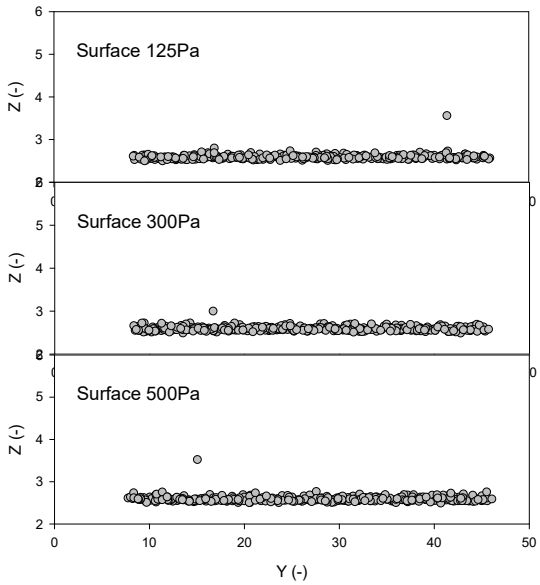

Figure K2 The snapshots of molecular configurations at specific pressure points (125Pa, 300Pa and 500Pa) as marked on the grand canonical isotherms in Figure K1.

Appendix L

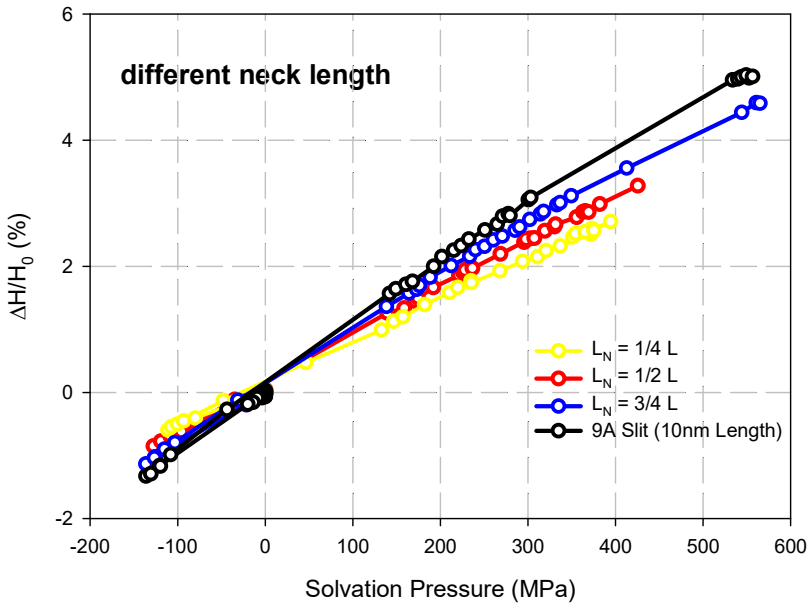

Figure L1 The percentage change of pore width versus solvation pressure in the region of narrow section for Case 3.

Appendix M

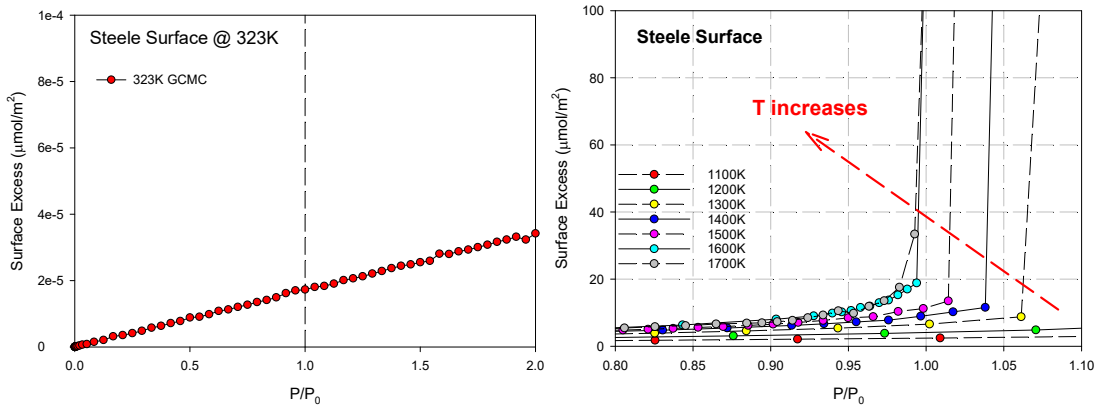

(a) (b)

Figure M1 The adsorption isotherm of mercury on graphite surface at (a) 323K and (B) 1100-1700K.

As shown in Figure M1(a), at ambient conditions, mercury does not adsorb on graphite and the isotherm crosses the P_0 axis with a finite angle. Only when temperature is increased to 1600K and beyond, mercury wets the surface.

Appendix N

The hypothetical adsorbed amount of mercury in activated carbon based on the data in ref [207].

Reported pore volume: 0.33 cm^3/g

Density of liquid mercury: 13.56 g/cm^3

Then the hypothetical amount adsorbed should be: $0.33 \times 13.56 \approx 4.5$ g(Hg) / g(AC).

But the highest adsorbed amount measured experimentally is ~120 μg/g which is ~0.003% of the hypothetical value.

Appendix O

Figure O1 shows the canonical isotherms in 1nm slit pore at 800K (T_F) and 1000K (T_P) together with the corresponding GCMC isotherms for comparison.

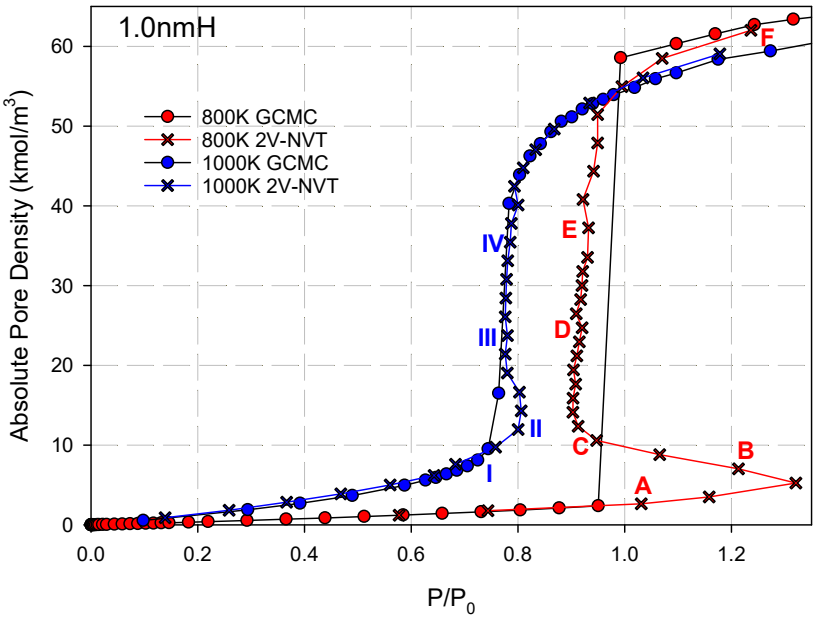

Figure O1 Isotherms of 1.0nm width slit pore at 800K and 1000K obtained with *2V-NVT* method (cross symbols). The isotherms obtained with *GCMC* are also presented as filled circle symbols.

Figure O2 shows the snapshots for Point A to F at 800K as marked in Figure O1. This 1.0nm width pore can accommodate two layers of mercury molecules, and to show clearly the configuration only one layer is presented. Once again we observed the nucleation and coalesce of clusters at 800K, just like the case in 0.63nm width pore at 323K. The snapshots of molecules for 1000K are shown in Figure O3, and it is seen that there is no formation of distinct clusters due to the high thermal fluctuations.

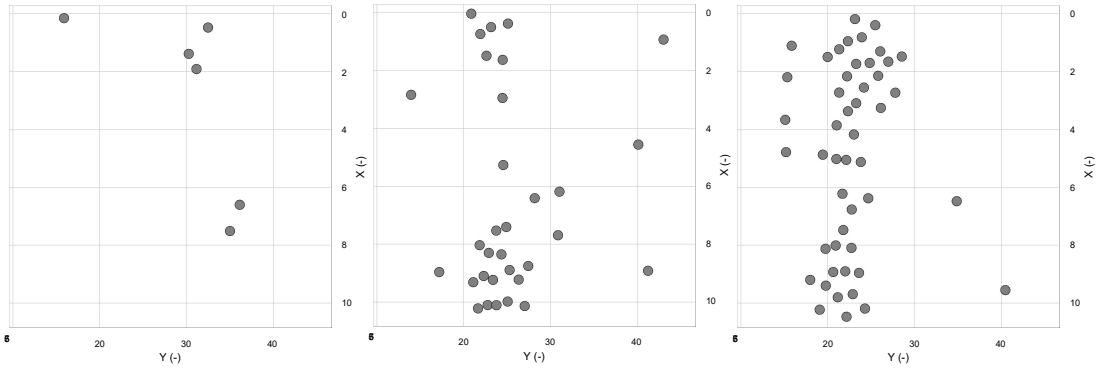

A B C

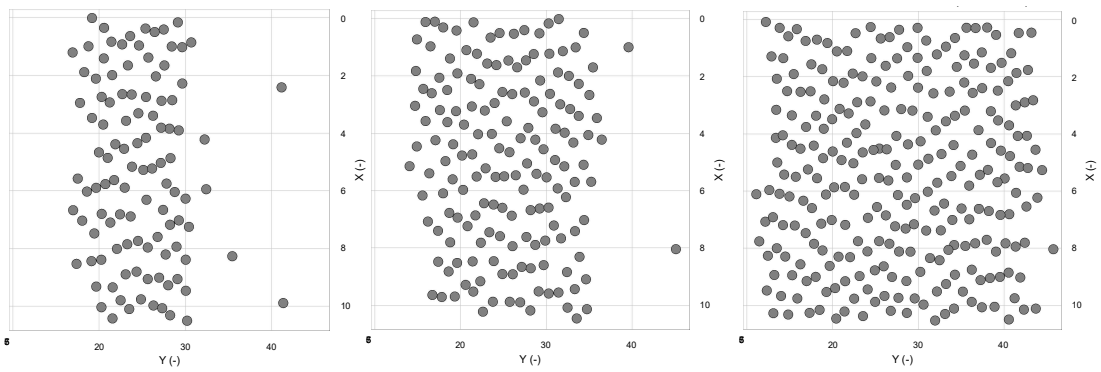

D E F

Figure O2 Top view of snapshots of the bottom layer of 1.0nm width slit pore at 800K using *2V-NVT* method. Point A to F are labelled in Figure O1.

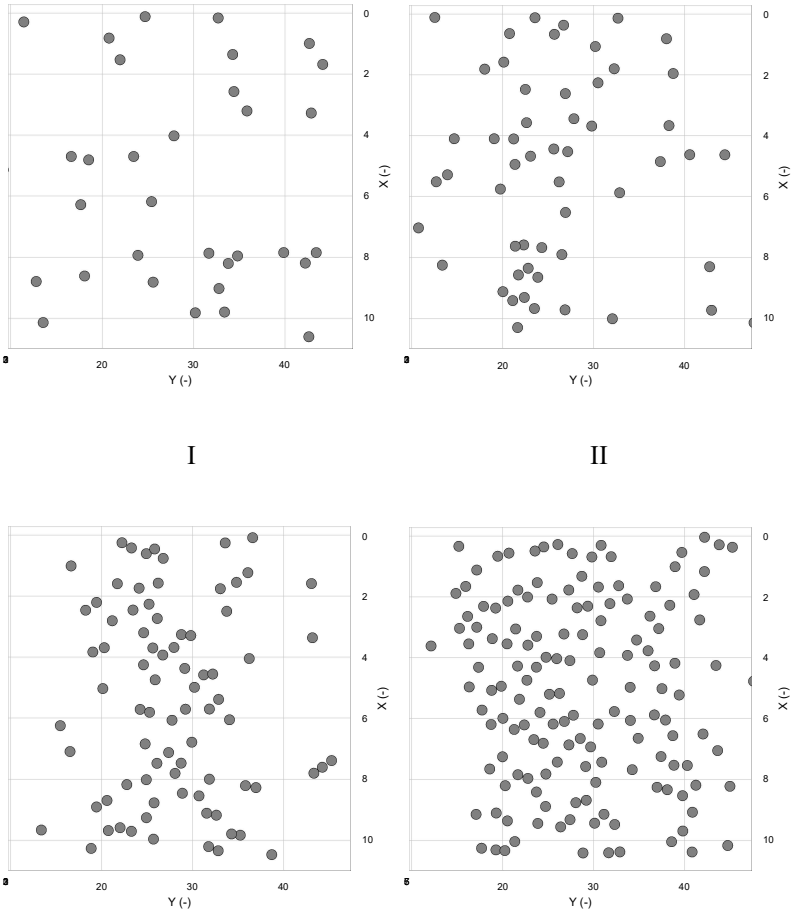

I II

III IV

Figure O3 Top view of snapshots of the bottom layer of 1.0nm width slit pore at 1000K using *2V-NVT* method. Point I to IV are labelled in Figure O1.

Appendix Copyright Permission Statements

Chapter 6 and the part about New Potential Model of Mercury in Chapter 3 were reprinted with permission from (Xiu Liu, Chunyan Fan, D.D. Do, Vishnu Pareek, Peiyu Yang. A temperature-dependent potential model for mercury in the description of vapour-liquid equilibrium & adsorption in activated carbon, Chemical Engineering Science 2020, 215, 115453)

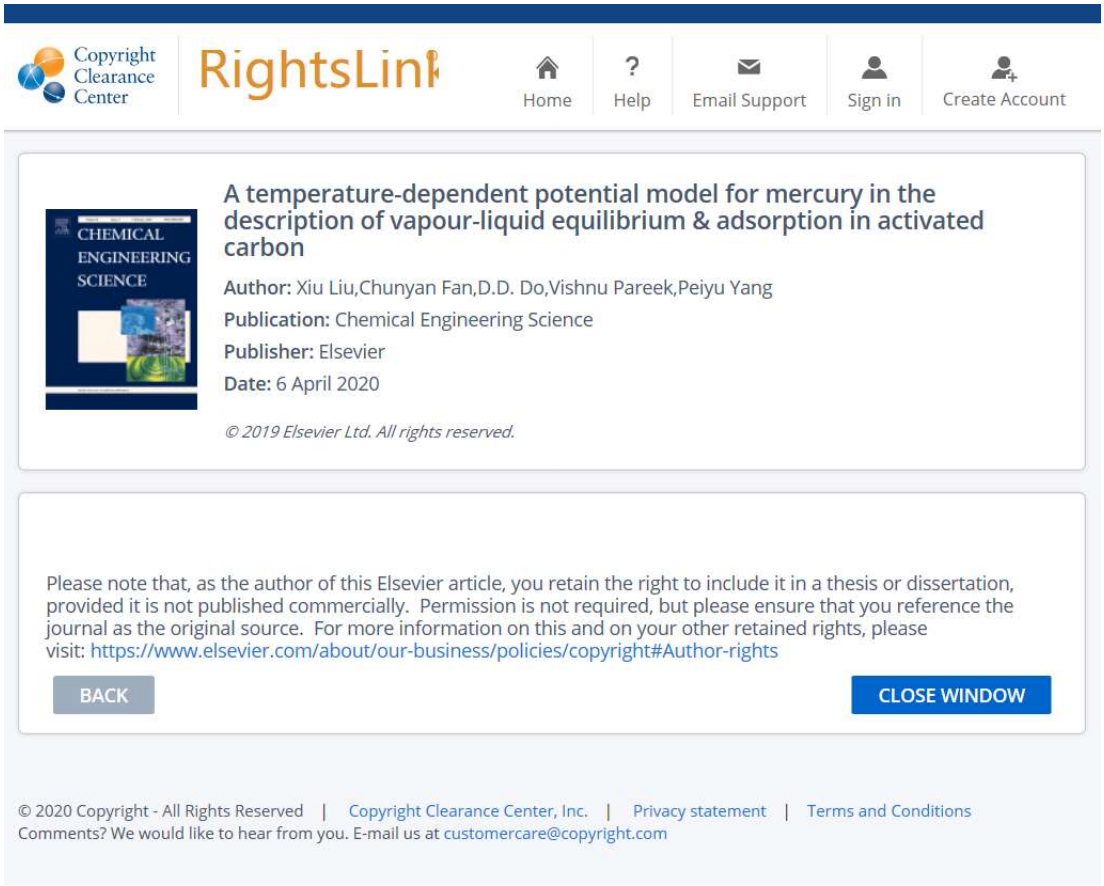

The part about closed wedge pore in Chapter 4 is reprinted with permission from (Xiu Liu, Chunyan Fan, D.D. Do, Chee Fei Leong. On the hysteresis of low temperature adsorption of xenon in graphitic wedge pore, Chemical Engineering Journal 2020, 390, 124499)

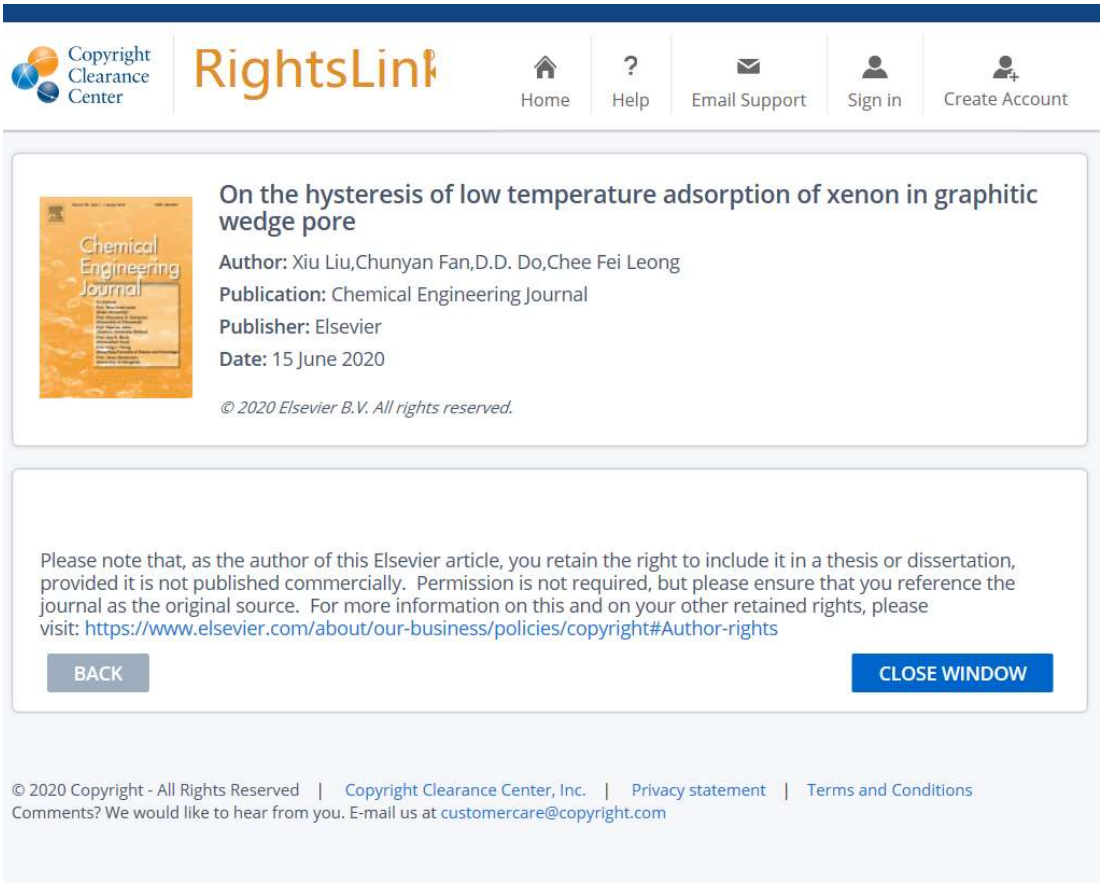

The part about open wedge pore in Chapter 4 is reprinted with permission from (Xiu Liu, Chunyan Fan, D.D. Do. Microscopic characterization of xenon adsorption in wedge pores, Adsorption 2019, 25, 1043–1055)

SPRINGER NATURE LICENSE
TERMS AND CONDITIONS

Apr 12, 2020

This Agreement between Ms. Xiu Liu ("You") and Springer Nature ("Springer Nature") consists of your license details and the terms and conditions provided by Springer Nature and Copyright Clearance Center.

License Number	4806540852457
License date	Apr 12, 2020
Licensed Content Publisher	Springer Nature
Licensed Content Publication	Adsorption
Licensed Content Title	Microscopic characterization of xenon adsorption in wedge pores
Licensed Content Author	Xiu Liu et al
Licensed Content Date	Mar 27, 2019
Type of Use	Thesis/Dissertation
Requestor type	academic/university or research institute
Format	print and electronic
Portion	full article/chapter
Will you be translating?	no
Circulation/distribution	100 - 199
Author of this Springer Nature content	yes
Title	Fundamental Study of Gas Adsorption in Porous Materials using More Realistic Models
Institution name	Curtin University
Expected presentation date	Apr 2020